Passivation and Dissolution of Alloys

by

Yusi Xie

A Dissertation Presented in Partial Fulfillment
of the Requirements for the Degree
Doctor of Philosophy

Approved November 2020 by the
Graduate Supervisory Committee:

Karl Sieradzki, Chair
Candace Chan
Qing Hua Wang
Daniel Buttry

ARIZONA STATE UNIVERSITY

December 2020

ABSTRACT

The passivity of metals is a phenomenon of vast importance as it prevents many materials in important applications from rapid deterioration by corrosion. Alloying with a sufficient quantity of passivating elements (Cr, Al, Si), typically in the range of 10% - 20%, is commonly employed to improve the corrosion resistance of elemental metals. However, the compositional criteria for enhanced corrosion resistance have been a long-standing unanswered question for alloys design. With the emerging interest in multi-principal element alloy design, a percolation model is developed herein for the initial stage of passive film formation, termed primary passivation. The successful validation of the assumptions and predictions of the model in three corrosion-resistant binary alloys, Fe-Cr, Ni-Cr, and Cu-Rh supports that the model which can be used to provide a quantitative design strategy for designing corrosion-resistant alloys. To date, this is the only model that can provide such criteria for alloy design.

The model relates alloy passivation to site percolation of the passivating elements in the alloy matrix. In the initial passivation stage, Fe (Ni in Ni-Cr or Cu in Cu-Rh) is selectively dissolved, destroying the passive network built up by Cr (or Rh) oxides and undercutting isolated incipient Cr (Rh) oxide nuclei. The only way to prevent undercutting and form a stable protective passive film is if the concentration of Cr (Rh) is high enough to realize site percolation within the thickness of the passive film or the dissolution depth. This 2D-3D percolation cross-over transition explains the compositional dependent passivation of these alloys. The theoretical description of the transition and its assumptions is examined via experiments and kinetic Monte Carlo simulations. The initial passivation scenario of the dissolution selectivity is validated by

the inductively coupled plasma mass spectrum (ICP-MS). The electronic effect not considered in the kinetic Monte Carlo simulations is addressed by density functional theory (DFT). Additionally, the impact of the atomic configuration parameter on alloy passivation is experimentally measured, which turns out to agree well with the model predictions developed using Monte Carlo renormalization group (MC-RNG) methods.

ACKNOWLEDGMENTS

I would like to express my special thanks and sincere gratitude to my advisor, Prof. Karl Sieradzki, for his patient guidance and continuous support throughout my years in the group. I am deeply touched by his intelligence, critical thinking, and rigorous attitude to research. It is his immense reservoir of knowledge and the great passion for researches that motivates me to further the research through abundant reading and critical thinking. He provides me the freedom to explore the topic I am interested in and always backs me up whenever I encounter problems. His encouragement and patience have truly made the originally arduous journey such great enjoyment, and I will cherish this time forever.

I would like to thank Prof. Qing Hua Wang, Prof. Candace Chan, and Prof. Daniel Buttry for participating in the research as committees and providing valuable insights and constructive advice. I am grateful to all my collaborators: Great thanks to Dorota Artmymowicz for performing the KMC simulations and the MC-RNG analysis; Pietro Lopes helps to conduct online ICP-MS analysis with the Argonne National Laboratory facilities; Prof. Houlong Zhuang and Duo Wang helps me to build a basic understanding in DFT simulations and helps with dissociative adsorption simulations; Haijun Jin helps to prepare Cu-Rh bulk alloys with arc melting. I would like to thank my lab-mates, thanks to Minglu Liu, the former post-doctorate in the group, for tremendous help with lab fundamentals; thanks to Erin Karasz, Ashlee Aiello for all the discussions we had when I had problems over the research and the experiments. I gratefully acknowledge the utilization of the facilities in John M. Cowley Center for High Resolution Electron

Microscopy, Machine and Electrical shop and computational resources of the Agave cluster at Arizona State University.

I would like to thank my boyfriend for his accompaniment, understanding and love over the past years. Thanks to my parents for their unconditional love, always understanding and supporting me to choose a life I pursue.

Support for this work was provided by the National Science Foundation, Division of Material Researches under award DMR-1708459.

TABLE OF CONTENTS

Page

LIST OF TABLES

Table Page

LIST OF FIGURES

Figure Page

Figure Page

Figure Page

Figure Page

Figure Page

CHAPTER 1

INTRODUCTION

1.1 Background

When exposed to an aggressive environment, metals and alloys that display passive behavior will form a continuous and protective thin film on the surface. An excellent passive film can reform when scratches or abrasive wear expose the underlying metal to an aggressive environment, preventing further corrosion. Elemental Chromium (Cr) is an excellent example of being protected by a thin film like this and could maintain metallic brightness for years in the wet atmosphere and aqueous solutions. Since the beginning of the 1900s, the industry has already known that alloying iron (Fe) with Cr radically improves the alloy's corrosion resistance, forming the predecessor of stainless steel[1]. It then took almost 50 years to figure out that when immersing in a corrosive environment, it is the instantaneously developed thin passive film (thickness of ~ 3nm) on the surface that constitutes the basis of the alloy's passivity[2].

Within the past few decades, the advance of sets of electrochemical techniques, surface science spectroscopy techniques, and scanning probes both ex-situ and in-situ inspire extensive investigations on the structural and compositional nature of the mysterious passive films, especially those developed on stainless steels[3–6]. A multilayer (mostly bilayer) structure has been revealed for most metals and alloys of industrial interests. For Fe, an inner Fe_3O_4 film and outer layer of hydrated γ-FeOOH sandwich a layer of γ-Fe_2O_3[7–11]. Ni has an outer layer of $Ni(OH)_2$ covering the inner NiO part[12–17]. Cr develops passive film with $Cr(OH)_3$ outsides the Cr_2O_3 layer[18]. However, even with intensive investigations and the utilization of the entire array of

modern analytical techniques, we currently know little about the initial stage of the passive film's development or the following crystallization process. With the critical role chemistry and reaction rate playing in passive film formation, every passive metal/environment combination would express specific characteristics. This diversity of passivation systems and the environment further negates the chance of establishing a universal model for the passivation processes.

When increasing the Cr concentration in binary Fe-Cr alloys, the corrosion resistance against the natural atmosphere and mildly acidic environments shows dramatic enhancement at ~13 at.% Cr. This critical threshold has been known for a long time and has been widely employed when engineering the composition of stainless steel in the industry. Similar to Cr in the Fe-Cr alloys, the progressive addition of passivating components such as Cr, Al, Si displays a critical composition where their decent corrosion resistance prevails over the poor passivation behavior of matrix element, even though the critical value varies with different alloy systems. Several theories have been proposed to predict the minimum composition for nice passivity, but none of them has been fully substantiated.

Recently an accelerated exploration of multiple-principal element alloys (MPEAs) for structural applications emerges due to their supreme structural strength and thermal stability under extreme environment. When narrowing down the vast formulation options of MPEAs to design promising alloys families with the potential strengths fully expressed, criteria that could predict the alloy properties are required. While there are design criteria in mechanical properties, no such criteria stand in alloy design for enhanced corrosion resistance. The emerging interests in MPEAs bring this long-standing

unsolved question of composition-dependent passivity of alloys in corrosion science back to the table. Here we try to rationalize the existing data, develop a predictive physical model for the passivation process, and explain the composition-dependent passivation behaviors in alloy passivation.

1.2 Thesis overview

The composition and structure of passive films that form over extended periods have been extensively studied. However, we know little about the initial stage of the passivation process occurring in a much shorter time scale, which sets the stage for the subsequent development. Factors controlling alloy passivity include crystal structure, alloy composition, and atomic configuration, which could be utilized as the "controlling knobs" for alloy designer to tune the corrosion resistance. The present work aims to accelerate our understanding of the initial passivation process and develop a quantitative theory, percolation model, for this initial passivation stage. The percolation model is

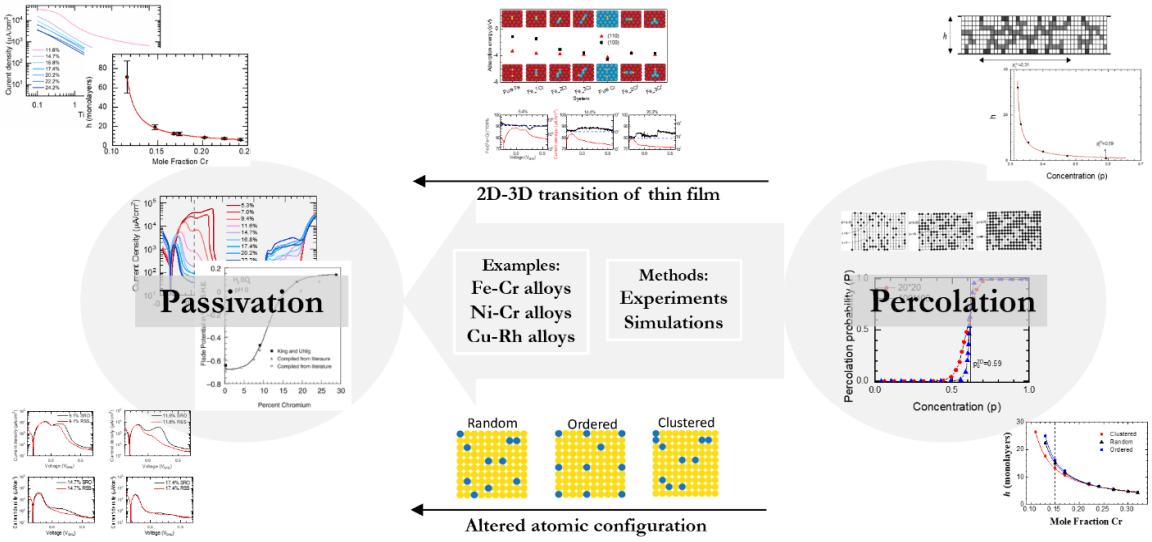

Figure 1.1. Overview of the analysis carried out in this work.

validated with its assumptions and predictions over these factors through a framework shown in figure 1.1. The studies are conducted in two aspects.

One involves the key designing parameter: the alloy composition. As the concentration of the passivating element in the alloy increases, the transition of the passive film thickness is measured with both electrochemical experiments and kinetic Monte Carlo (KMC) simulations. The measured transition behaviors are compared with the predictions of the model by fitting with a theoretical equation. Density functional theory (DFT) calculations and inductively coupled plasma mass spectroscopy (ICP-MS) analysis are conducted to verify the two assumptions of the model: 1) passivating elements clusters of small size in the alloy show electrochemical behaviors close to corresponding pure element; 2) under the defined conditions, surface passivation is achieved with reactions of primary passivation.

On the other hand, the atomic configuration of the alloy is altered by different heat treatments. Large cell Monte Carlo renormalization group (MC-RNG) methods and KMC simulations are employed to predict the impact of atomic distribution on alloy passivation behaviors. The prediction is compared with results obtained from electrochemical experiments.

The examination of the percolation is conducted in three alloy systems: Fe-Cr, Ni-Cr, and Cu-Rh. All the examined systems show excellent agreement with the percolation model, which supports us in predicting the critical value for alloy design.

1.3 Passivity of metals and alloys

The corrosion and passivation behaviors of a material is a reflection of the interaction between the material and the surrounding environment. Two primary methods

offer the starting points to study a corrosion system: the Pourbaix diagram and potentiodynamic polarization.

1.3.1 From a thermodynamic point of view

In most cases, thermodynamics gives an excellent first guide for understanding a corrosion system. Marcel Pourbaix firstly invented a straightforward method to summarize the thermodynamic information of a corrosive system onto a potential-pH diagram, known as the “Pourbaix diagram”. He has developed a gallery for systems of the pure elements in the water[19]. A Pourbaix diagram maps out the most electrochemically stable species of the studied element under a particular potential and pH. It determines whether the metal under these conditions will undergo corrosion or maintain immunity by the state of the most stable species as ions in aqueous solution or solids protecting the underlying metal. For instance, the Pourbaix diagram of Cr in figure 1.2 shows that when the Cr electrode is immersed in a solution with a pH of 0 and applied with a potential of 0.5 V_{SHE}, the most thermodynamically stable state of Cr is Cr^{3+}. Under this condition, the Cr electrode will dissolve as Cr^{3+}, suffering corrosion. The Pourbaix diagrams are constructed based on the Nernst equation under thermodynamic equilibrium. Conventionally, the data for free Gibbs energy of reacting compounds is estimated based on experimental heat measurements. Thanks to the recently increasing accuracy and capability of density DFT calculations, the thermodynamics could be more accurately described with cases like complicate alloy or compounds, materials of low dimension, and systems with defined defects[20].

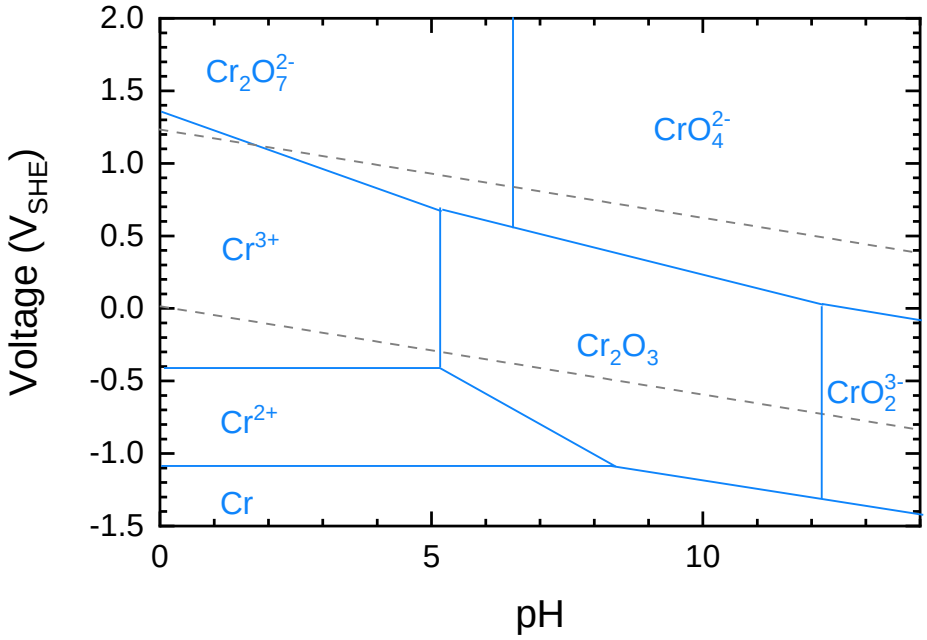

Figure 1.2. The Pourbaix diagram of Cr at 25℃[19].

Like the phase diagram, Pourbaix diagrams are constructed assuming all the reactions under equilibrium, and no reacting rates are considered. However, the actual reactions could be far from equilibrium. Especially in the case of the passivation where the growth of the passive film is more kinetically controlled: the formation of the most thermodynamically stable species usually could be sluggish, and then the kinetically favorable one prevails. A passive film is developed far from equilibrium in terms of both composition and structure. It should also be pointed out that the oxides located in the Pourbaix diagram are thick, bulk materials, of which the properties may be far different from the thin film(~ nanoscale) counterpart passivating the alloy/metal surface in the real case. Furthermore, the diagrams simply rule out the possibility of other nonstoichiometric passive oxides or hydroxides.

For all these reasons, it is not surprising to find that the passivation behaviors predicted by the Pourbaix diagram deviate from the experimentally measured behaviors. As shown in figure 1.2, when fixed pH at 2 and electrode potential controlled under a range of [-0.3 V_{SHE}, 1.2 V_{SHE}], Cr resides in the region of corrosion. However, it turns out that Cr forms a compact thin film and shows decent immunity to acids under the potential higher than 0.2 V_{SHE}.

1.3.2 From a kinetic point of view

An upper limit time associated with passivation is in order of 10^{-2} s. The rapid development of the passive film is limited by reaction kinetics and diffusion, yielding to an initially thermodynamically unstable film. The status that kinetics overwhelm thermodynamics is maintained with a low chemical dissolution rate of the passive layer. The reason that the passive layer deviates from dissolution equilibrium is the extremely slow transfer rate of the oxide cations (M^{n+}) at the oxide film/solution interface, which is hindered by a high activation barrier of releasing M^{n+} from the oxide into solution. The thickness of the thin film preserves through a dynamic equilibrium between the chemical dissolution and the growth of the passive film. The underlying metal is dissolved with the oxidized M^{n+} traveling towards the oxide/electrolyte interface, while oxide (hydroxide) grows via O^{2-} or OH^- decomposed from H_2O in the electrolyte and transferred towards the metal/oxide interface.

Another kinetic effect that has always been addressed during the passivation process is the so-called “aging effect”. Numerous experiments have reported a phenomenon that the physical and chemical nature of the passive films, such as the crystalline structure, compositions, hydration degree, and electronic properties,

significantly evolve with time, which usually improves the protectiveness of the film. Take Fe-Cr alloys for example, after exposure to air or aging under polarization for hours, the initially formed amorphous passive film on alloys of high composition (e.g., 21 at%) evolves to be nanocrystalline[21,22].

Anodic polarization curves are very instructive to capture the trace of kinetics and are commonly used to understand the electrochemical basis of what is happening at the reacting surface. Similar to the common electrochemical reactions not involving electrode, the dissolution kinetics of the electrode can be extracted from the shape of the curve at low polarization by fitting it to the theoretical equations for activation polarization. The reaction rate limited by the corrosion products diffusion deviated the exponential log i-overvoltage curve in forms of concentration polarization. In metal/alloy passivation, the active-passive transition reaction on the electrode surface is the reason for exacerbating the deviation of the polarization curve — the dramatic current drop with increasing potential marks the formation of passive films.

Various metals and alloys that undergo active-passive transition share a characteristic curve shape in acid solution. Take the anodic polarization curve of Fe-Cr alloy (17.4 at.%) for example (as shown in figure 1.3), three potential regions, namely active dissolution, passivation, and trans-passivation, can be generally identified. Starting

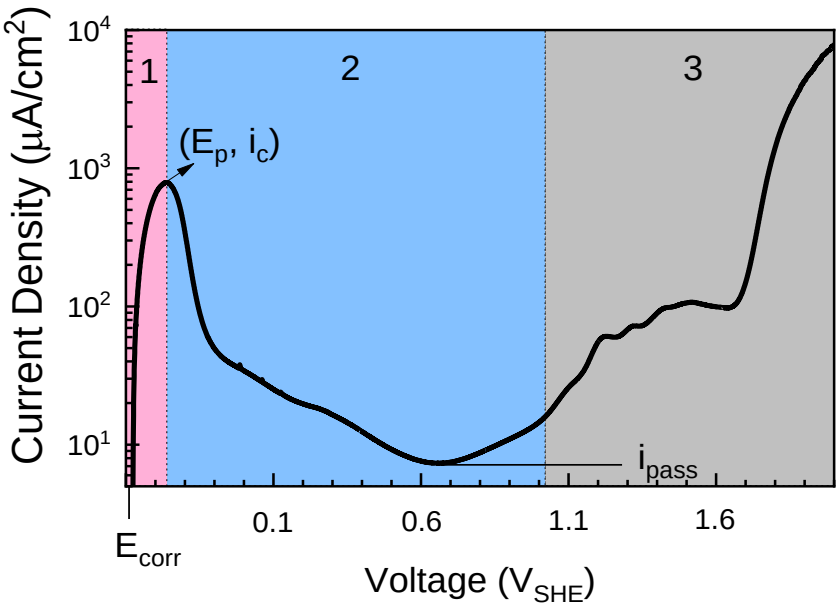

Figure 1.3. A typical anodic polarization curve of metals and alloys with an example of Fe-17.4 at.% Cr in 0.1 M H_2SO_4 showing sharp active-passive transition, the scanning rate of 5 mV/s. The curve is divided into three regions: 1. Active dissolution region; 2. Passivation region; 3. Transpassive region. The corrosion potential, passivation potential, critical current and, passivation current are marked.

from E_{corr}, where hydrogen evolution counteracts the free corrosion and gives to zero net currents, increasing voltage accelerates the dissolution rate of the metal. When approaching the end of the active dissolution region, passivation prefers to start locally at the more active sites, such as steps, of the surface, contributing to the curvature in the log i-overvoltage plot. As identified with a dramatic decrease in current, the surface is covered by a continuous protective film at passivation potential (E_p), also called Flade potential (E_{Flade}). With further increases in the applied potential, the current density increases again, entering the so-called transpassive region. The transpassive region includes the potentials where the passive film breaks down, and O_2 evolves from the decomposition of the water.

The critical current density (i_c), e.t, the maximum current density reached in active/passive transition, is commonly used to indicate the "easiness" of passivation. The lower i_c is, the less metal is consumed by dissolution before the passivation is achieved. The lowest current density in the passivation region is defined as the passivation current density (i_{pass}). It corresponds to the electrochemical dissolution and is determined by ion transportation through the passive film, which partly reflects the "protectiveness" of the film. Chemical dissolution is another part to be considered concerning the stability of the passive film. Both the electrochemical and chemical dissolution depends on the properties of the film, such as the chemical composition, grain size, and defects.

Keddam has attempted to establish a series of reaction paths for Fe-Cr alloys passivation, with an address on the kinetics of dissolution and passivation reactions[23]. He proposed several possible dissolution and passivation reactions for Fe and Cr, as listed in figure 1.4a, and conducted conventional simulations with corresponding kinetic parameters listed in figure 1.4b. The surface passivation was suggested to originate from some Cr-related blocking species, blocking the dissolution of Fe in the reaction path of $Fe\ (II)_{ad}$ to $Fe\ (II)_{sol}$. This blocking effect is realized in the simulations through equation 1.1:

$$K_4 * \theta_{Fe(II)ad} * (1 - \sqrt{\theta_{Cr(II)ad}}), \qquad (1.1)$$

where K corresponds to kinetic constants of the corresponding reaction path; θ's are the coverage of different species on the surface.

(a)

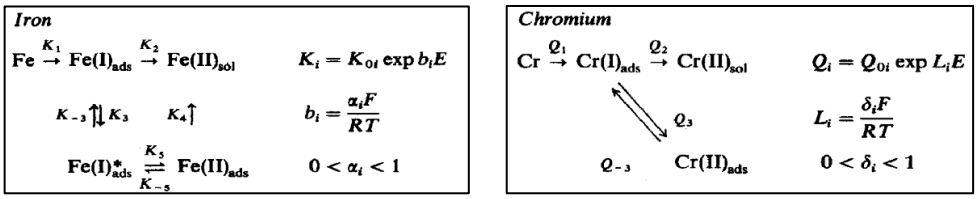

(b)

Alloy	Kinetic constants																			
	K_1		K_2		K_3		K_{-3}		K_5		K_{-5}		K_4		Q_1		Q_2		Q_3		Q_{-3}	
	K_{01}	b_1	K_{02}	b_2	K_{03}	b_3	K_{-03}	b_{-3}	K_{05}	b_5	K_{-05}	b_{-5}	K_{04}	b_4	Q_{01}	l_1	Q_{02}	l_2	Q_{03}	l_3	Q_{-03}	l_{-3}
Fe-7Cr	2×10^{7}	38.4	2×10^{-3}	7	4×10^{-9}	0	5.2×10^{-20}	30	1×10^{5}	35.4	1×10^{-7}	3	6×10^{-5}	7.3	3.4×10^{13}	38.4	3×10^{-3}	10	3×10^{-3}	19.2	3×10^{-12}	19.2
Fe-10Cr	6×10^{7}	38.4	2×10^{-3}	7	6×10^{-9}	0	5.2×10^{-20}	30	1.6×10^{5}	35.4	1×10^{-9}	3	2×10^{-7}	2	3.4×10^{12}	38.4	3×10^{-3}	10	1.2×10^{-2}	19.2	6×10^{-14}	19.2
Fe-22Cr	1×10^{8}	38.4	2×10^{-3}	7	1×10^{-8}	0	5.2×10^{-20}	30	4×10^{5}	35.4	1×10^{-12}	3	2×10^{-8}	2	3.4×10^{10}	38.4	3×10^{-3}	10	4×10^{-2}	19.2	1.2×10^{-15}	19.2

Units of K: mole $cm^{-2} s^{-1}$; l and b: V^{-1}.

(c)

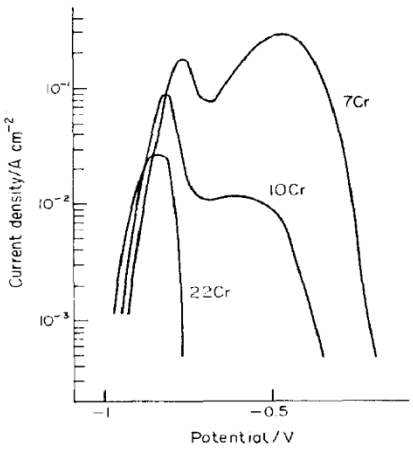

Figure 1.4. Keddam's kinetic models[23]. (a) The reaction paths were brought up for Fe and Cr; (b) the kinetic constants he used in the conventional simulations for polarization curves of alloys with different Cr contents; (c) obtained curves of Fe 7 at.% Cr, Fe 10 at.% Cr and Fe 22 at.% Cr from the simulations.

An excellent match is observed when comparing the Keddam's simulated current-voltage curve, as shown in figure 1.4c, with those experimentally measured ones. However, the assignments and alteration of the kinetic parameters in his simulations can hardly be reasoned and substantiated. For example, he increased the K_1 as Cr concentration increases for no apparent reasons. Nevertheless, the critical role reaction kinetics play in passivation stands out by the simulations.

1.4 Theories for the critical values of alloy passivation

With the industrial importance of the Fe-based alloys, the fact that a minimum addition of 13 at. Cr % to Fe passivates the alloy surface has become well known and is employed in alloy engineering for a long time. The value is obtained from the sudden change of the passivation potential and the critical current during the progressive addition of Cr to Fe in strong acid[24,25]. This well-known value could also be seen in the radical increase in the Cr enrichment of oxide films developed on the Fe-Cr alloys with gradually increasing Cr concentration in the alloy[26]. In addition to Fe-Cr alloys, several other binary alloys have also been reported to display a similar critical alloying composition: adding a certain quantity of the passivating element to the host metal could remarkably enhance the corrosion resistance of the alloys. The critical value for different alloy systems is not universal and varies a lot with environmental conditions. Tammann[26] reported some critical compositions in binary alloys based on the transition of the critical current over alloys composition. They are 40 at.% Ni to Cu, 15 at.% Mo to Ni, 8 at.% Cr to Co, 14 at.% Cr to Ni. Since then, several theories have been developed with explanations for the well-known 13 at.% Cr in Fe-Cr alloys as an example and also extended to other binary alloys. These theories are not mutually exclusive but addressing different aspects of the passivation process. This section will briefly discuss each of these theories to attain some insights on the passivation process from different perspectives.

1.4.1 Electron configuration theory

Uhlig[27,28] first ascribed the passivation of the metal surface to the chemisorption of an oxygen monolayer. He then developed the electron configuration theory for alloy passivation based on the adsorption conjecture and tried to rationalize the

critical composition in alloys passivation. His theory is based on the observation that uncoupled d-electrons in transition metal create stronger adsorption bonds with O_2. Uhlig claims that the alloying process will redistribute the electrons between the constituting elements: the unpaired d-electron band of the passivating element is filled by electron donation from the non-passivating element. The passivity of the alloys dies when the non-passivating element overweighs.

Figure 1.5 illustrates the redistribution of the electron during the passivation of Fe-Cr alloys. Electrons are transferred from the Fe s-band to Cr d-band vacancies, weakening the chemisorption bonds of Cr with O and thus retarding Cr-like passivation. In low Cr alloys, where the d-band electron vacancy of Cr atom is all filled, the Cr-like passivation disappears. The critical Cr composition Uhlig calculated for the Fe-Cr system is 16.7 at.%, nominally match the experimentally reported value, 13 at.%[24,25]. This theory is more successfully applied in the Cu-Ni system, whose passivity in acid solution vanishes once Cu content reaches above 60 at.%, while Uhlig's calculation yields to a

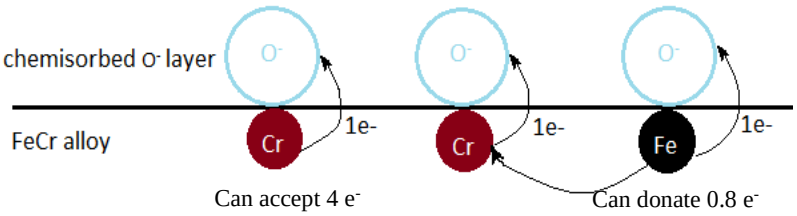

Figure 1.5. Schematic illustration of electron configuration theory for the passivity of alloys with an example of Fe-Cr alloys[24]. Every surface Cr atom has four d-vacancies to be filled up, while each surface Fe atom has 0.8 s-electron to donate. Both Cr and Fe atom donate one s-electron to form chemisorption bonds with Oxygen. When the d-vacancies of one Cr atoms are filled by 3-electrons from 5 Fe atoms, the Cr-like passivity disappears, which yields to a critical composition of 16.7-at.% Cr.

critical value of 59 at.%[29,30]. Uhlig later also extended his theory for critical alloy composition in other binary alloys such as Fe-Ni, Fe-Co, Ni-Cr, and Co-Cr alloys[31].

It is generally accepted that the quality of the thin layer of the passive film determines the corrosion resistance of alloy/metal. The common criticism for electron configuration theory is that it neglects the critical role passive film plays in passivity. However, it should be valued that the electron configuration theory, addressing the change of electronic properties during alloying, contributes to constructing a more comprehensive model for the passivity of alloys. With the advent of more powered computation ability, the first principles-based calculations of high accuracy are expected to better evaluate the electronic effects in alloying, which will also be emphasized with an example of FeCr alloys in session 2.4.1.

1.4.2 Graph theory

By contrast, McCafferty recently developed the graph theory highlighting the importance of passive oxide film[32,33]. He abstracted out a mathematical 2D graph for the mixed oxide films formed on alloys surface, in which the atoms and bonds of the

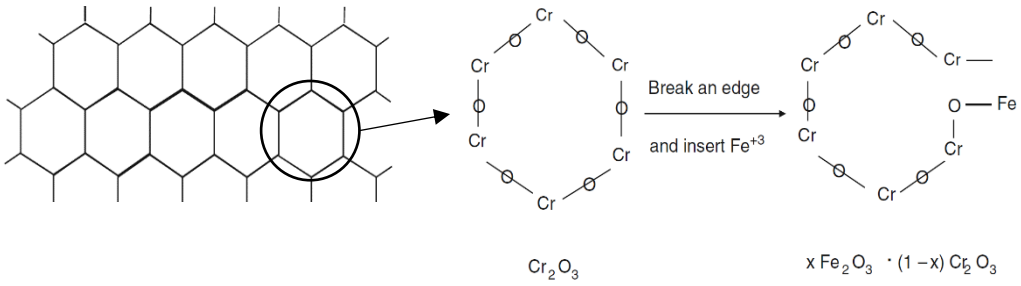

Figure 1.6. Illustration of graph theory for the passivity of Fe-Cr alloys[32]. Hexagons represent the Cr2O3 film with Cr^{3+} ions at vertices and O^{2-} at edges. The introduction of Fe^{3+} ions breaks the network of Cr_2O_3 film. Calculations show a continuous -O-Cr-O- network exists only when the Cr composition in the film is above 30 at.%.

oxide unit, -M-O-M-, are represented by vertices and edges. Take Fe-Cr binary alloys, for example: a hexagonal lattice stands for -Cr-O-Cr- network, interpolation of Fe^{3+} into the vertices will cut off the connectivity and disjoins the protective Cr oxide network, as shown in figure 1.6. Calculations show that 70 at.% Fe^{3+} is sufficient to destroy the Cr oxide network and, thus, the protective passive film. The value is connected to the well-known critical value, 13 at.% Cr, through the in situ XANES observation reported by Oblonsky[34] that Cr^{3+} accounts for 30% of cations in the oxide film formed on Fe-13 at.% Cr alloy. This approach was later successfully applied to other systems of Ni–Cr, Cu–Ni, Fe–Si, Co–Cr, and Al–Cr alloys to explain the occurrence of critical composition[32,33].

As mentioned earlier, various investigations have found that the nature of passive films is unduly complex and elusive. The aging process of compositional and crystalline properties with time enormously depends on passivation environments like electrolytes and potentials. The single value McCafferty picked for the film composition can hardly stand when the conditions are changed.

In addition to graph theory, McBee and Kruger also underline the vital role of passive films in passivity and associate the critical value with the observation that the crystallinity of the passive film developed on Fe-Cr alloys transits from a polycrystalline state to an amorphous state at around 13 at.% Cr. They ascribed the corrosion resistance of alloys with higher Cr concentration to the evolution of amorphous oxide films. The amorphous film was suggested to be more protective with less mobile ions than the crystalline structure, which contains defects and grain[35]. Nevertheless, their explanation contradicts the experimental observation that the amorphous oxide film

developed on Fe-Cr alloys tends to re-crystallize itself but ends up with a more protective oxide film[21,22].

The graph theory and McBee and Kruger's explanation focus on the behavior of oxide film rather directly on the root of the phenomenon – the alloy itself, leaving the passivation mystery still unsolved.

1.4.3 Percolation model

Like graph theory addressing the geometric connectiveness, Sieradzki and Newman[36–42] explain the critical composition in binary alloys with site percolation but focus on the parent alloys. In Fe-Cr alloys, the authors consider that a minimum distance exists for two neighboring Cr atoms within which the adsorbed O could bridge the two Cr atoms and forms -Cr-O-Cr- bonds, the structural unit of a passive protective film. A percolating network of Cr atoms is required across the surface in order to develop a continuous protective passive film. As shown in table 1.1, the distance of two Cr atoms in an angled -Cr-O-Cr- bond, based on the hardcore sphere model, lies in between the distance of the 2nd and 3rd nearest neighbors (NN) in Fe-Cr alloys. On the other hand, the critical threshold 13 at.% Cr for decent passivity sits in between the percolation threshold of atoms with distance up to 3rd NN (p_c {1,2,3} = 9.4%) and 2nd NN (p_c {1,2} =17.4%) of body centered cubic (BCC) lattice. Besides the explanation for the classic critical content

Table 1.6. The distances between 1st, 2nd, and 3rd nearest neighbors of BCC Fe lattice and comparison with the radius of Cr and O ions in hard core sphere model[36].

Nearest neighbors/atoms	1st nn	2nd nn	3rd nn	Cr^{3+}	O^{2-}
Distance/radius	$\frac{\sqrt{3}}{2}$a=2.49Å	a=2.87Å	$\sqrt{2}$a=4.06Å	0.69Å	1.40Å

of 13 at.% Cr, the percolation model also addresses the p_c {1,2} as the threshold where -Cr-O-Cr clusters become infinitely connected without the assistance of 3rd NN. The conjecture is supported by the obvious improvement in the structural stability of the initial passive film above 17 at.% Cr by in situ synchrotron XPS[42].

The percolation model envisions the initial stage of passivation as Fe atoms are actively dissolved while Cr atoms develop -O-Cr-O- units with adsorbed O atoms. Once Cr composition in the alloy reaches above the percolation threshold, a protective passive film develops through the network of -Cr-O-Cr-. Otherwise, the continuous dissolution of Fe atoms would destroy the passive Cr oxides film so that no passivation status could be accomplished. The selective dissolution of Fe is evidenced by the remarkable enrichment of Cr in the passive film, reported by considerable XPS investigations[43–48].

The Cr K-edge by in-situ EXAFS spectra of the passive films developed on pure Cr has shown a similar structure to $Cr(OH)_3$[34,49], which corresponds to an amorphous hydrous oxide with CrO_6 octahedra linked together by hydrogen bonds. In the percolation model, the linking process between Cr atoms by O and the formation of -Cr(OH)-O-Cr(OH)- bonds is achieved through a process like gel polymerization, yielding to an initially amorphous $Cr(OH)_3$ film[21,22]. The increasing Cr concentration in the alloys is expected to boost the disorder of passive films. As shown in figure 1.7, in situ STM shows that as Cr concentration increases, the immediately formed long-range ordered films at low Cr contents gradually disappear. Instead, originally disorder or amorphous films form, which tend to crystallize themselves over time either in the air or under

polarization. The aging-induced structural relaxation was interpreted by a dehydration process of $Cr(OH)_3$ into Cr_3O_2, the -Cr(OH)-O-Cr(OH)- link evolves to -Cr-O-Cr-.

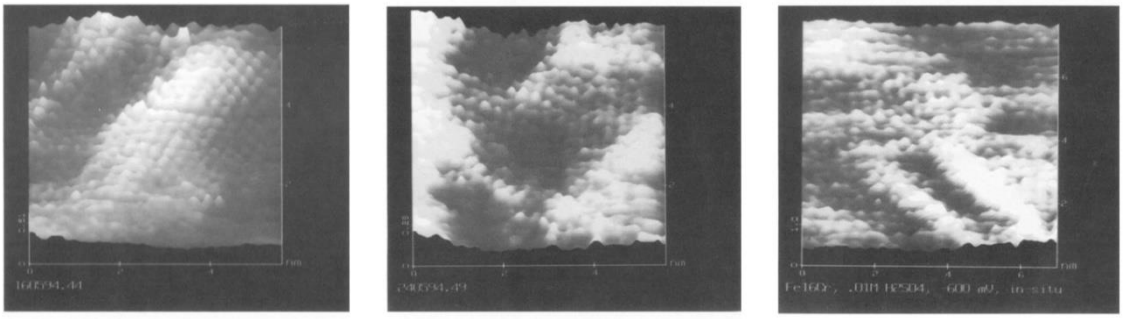

Figure 1.7. In-situ STM observation of the passive film developed on Fe-13.8 at.% Cr (left), Fe-14.7 at.% Cr (middle), Fe-16.5 at.% Cr (right) in 0.01 M H_2SO_4 at + 400 mV_{SCE} after passivation for about 1h (oblique view), a triangular lattice with a spacing of 3.1 Å is found. An increasing disorder is seen with increasing Cr concentration in the alloys[21,22].

In addition to experimental observations, Sieradzki and Newman employ computational simulations to address how the dissolution probability of the constitute elements changes the percolation criteria in the percolation model. The 2D and 3D simulations turned out to qualitatively reproduce the composition-dependent alloy passivation[39,40]. They assigned the "surface" Fe/Cr atoms in a randomly populated 2D/3D Fe-Cr alloy lattice with different dissolution probabilities, depending on the applied potential and local neighboring atoms. Cr atoms surrounded by two or more Cr atoms in 1st and 2nd NN have zero possibility of dissolution, simulating Cr oxide formation and the "surface" passivation. The other Cr and Fe atoms are assigned with specific dissolution probability, q_{diss}(Cr), and q_{diss}(Fe). The coordination chemistry effect was realized by varying q_{diss}(Fe) for Fe atoms with different atoms in NN. The impact of

applied potential is entered into the simulation via the changes of dissolution probabilities.

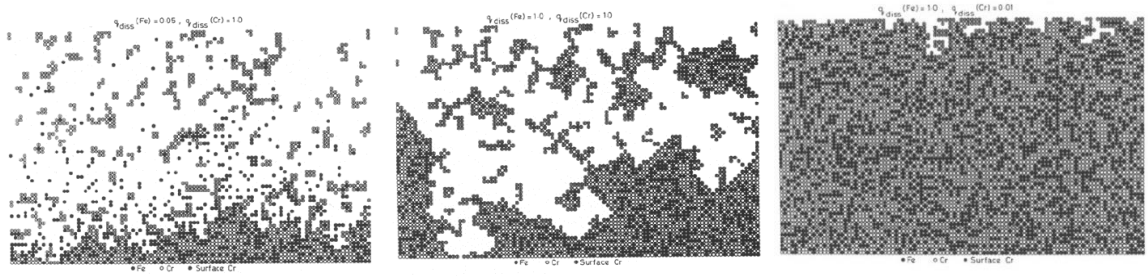

Figure 1.8. Endpoints of the simulations for random Fe-Cr alloys with Cr concentration, p, equal to 0.49 (49 at.% Cr) [39]. A active-passive transition is shown when varying the relative dissolution possibility of Fe and Cr is varied: left, $q_{diss}(Cr) = 1.0$, $q_{diss}(Fe) = 0.05$; middle, $q_{diss}(Cr) = 1.0$, $q_{diss}(Fe) = 1.0$; right, $q_{diss}(Cr) = 0.01$, $q_{diss}(Fe) = 1.0$.

The passivity of the alloy at a fixed composition turns out to depend on the ratio of $q_{diss}(Cr)$ to $q_{diss}(Fe)$, as shown in figure 1.8, which means that the passivation threshold is a function of the relative dissolution probability. The simulation results well match the experimental observation that the relative dissolution rates are determined by the applied potential and the pH of the environment. Active-passive transitions are found to occur around the site percolation threshold (~40% in 2D and ~16% in 3D for $p_c\{1,2\}$), when $q_{diss}(Cr)$ is set as 0 and $q_{diss}(Fe)$ as 1 to mimic the primary passivation, e.t., Cr is passivated and Fe is sufficiently selective.

So far, all the works they have reported are within the context of the Fe-Cr alloy system. Further development requires the successful application of the approach in broader subjects.

To sum up, passivation is a result of alloy interacting with the environment. All the models/theories only address the importance of the alloy part, with less attention paid to the environment. As the solution chemistry strongly impacts the passivation behavior

of the alloy, the changing environment should be reflected and addressed in the further development and refinement of those models.

1.5 From percolation to passivation

The composition and structure of the steady-state film that forms over extended time have been extensively investigated and characterized, while little of the initial stage of the passivation is explored and understood. This section introduces the further development of the percolation model that connects alloy passivation behavior to site percolation in a more generalized system, with addresses on the initial stage of passivation. The 2D-3D cross-over effects and the impact of randomness on the percolation threshold are introduced and applied in passivation.

1.5.1 Primary passivation

Based on the passivation behaviors of Fe- 24 at% Cr alloy in 1 M H_2SO_4, as shown in figure 1.9, Frankenthal[50–52] has divided the passivation region into two sub-regions: the primary passivation at lower potentials and the secondary passivation at higher potentials, with an interval potential termed as reactivation potential (E_a). The division of the two regions was determined by if hysteresis exists between positive and negative scanned LSV curves. As shown in figure 1.10a, Frankenthal claims that if the scanning is reversed at a potential higher than E_a, the i-V curve shows evident hysteresis. Reversibility can be achieved with hysteresis eliminated when the scanning potential does not exceed E_a. Though, specific careful pretreatments like sufficient reduction at cathodic potential, dissolving hundreds of layers at $E_{p,}$ and flushing new electrolytes to the surface are required before the reverse scanning. He suggests that the primary

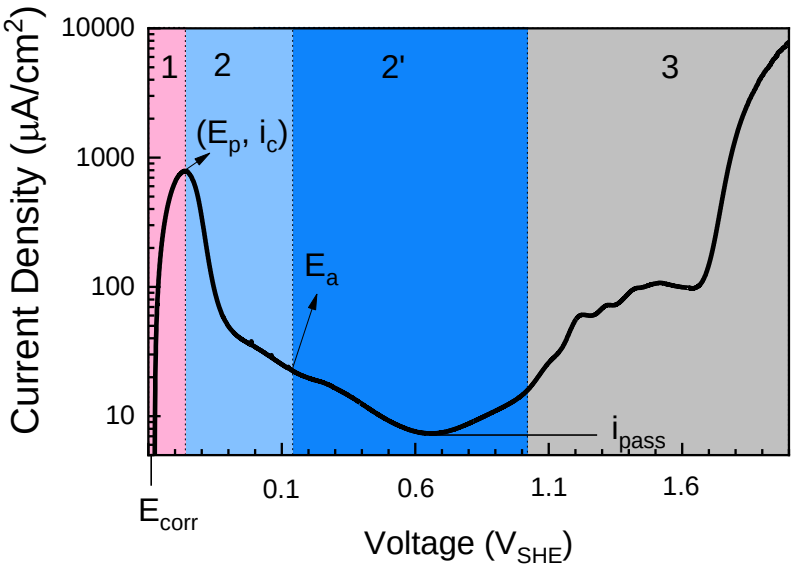

Figure 1.9. Anodic polarization curve of Fe-17.4 at.% Cr in 0.1 M H_2SO_4 with passivation region divided into two subregions: primary passivation region and secondary passivation region, the interval potential is marked as E_a.

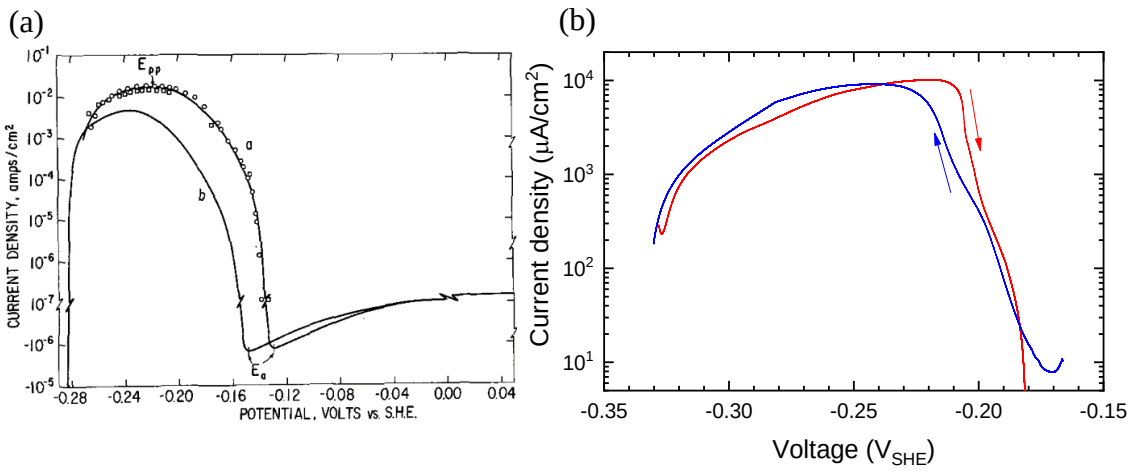

Figure 1.10. Comparison of the reversibility of polarization curves obtained by Frankenthal and us. (a) Potential current curves Frankenthal used to define E_a for Fe-24 at.% Cr in 1N H_2SO_4, curve a illustrates the reversible behavior in the potential range of primary passivating film. Squares and circles mark the points in positive and negative scans, respectively; curve b illustrates hysteresis caused by the presence of secondary film, the scanning rate is 100 mV/ hr[50]. (b) positive and negative scanning results we obtained for Fe-24.2 at.% Cr with a scanning rate of 0.03 mV/s and a rotating rate of 1000 rpm. Scanning was conducted after reduction at cathodic voltages and active dissolution at peak potential.

passivation is initiated by the coverage of oxygen ion on Cr atoms, which could be reversibly reduced when the scanning is reversed. In contrast, the passivation achieved in the secondary passivation region involves forming a mixed Fe/Cr oxide film. It was initially proposed that the reversibility and the nature of the film formed around E_a were independent of time. However, the claim was later corrected with an aging effect of the transition from primary passivation to secondary passivation.

We have tried to reproduce his results by following a similar procedure but ended up with pronounced hysteresis, as shown in figure 1.10b. In our experiments, the setup of flushing the surface with the fresh solution was replaced by a rotating electrode with a high rate (1000 rpm) to suppress the diffusion limitation impact on hysteresis. With negative scanning started at a potential 100 mV lower than the E_a reported by Frankenthal, a noticeable hysteresis was still observed (a potential shift around 100 mV). The reversibility proposed by Frankenthal may stand for pure metal. But for alloys, one would think that the reversibility only occurs if the dissolution before the passivation does not change the surface composition of the alloy, which means no selective dissolution is expected to occur. This contradicts the apparent and widely reported enrichment of Cr in the passive film[34,44,45,49,53].

The primary passivation that the percolation model refers to is not associated with the reversibility of the passivation, or the hysteresis between backward and forward LSV as Frankenthal proposed. It is defined by the relative contribution from the constituents of the alloys to the passivation, as underlined by q_{diss}(Cr) and q_{diss}(Fe) in Qian's computational simulations[39]. The percolation model attributes the critical value of alloy passivation to the threshold of passivating A atoms evolving an "infinite" cluster in

the parent binary alloy AB, with a presumption that B atoms do not participate in passivation at all, but instead, are actively dissolved into the electrolyte. The reason to address this assumption is that B atoms' contribution to passivation will lower the threshold of A atoms forming a percolated and protective network. The possibilities of both A and B atoms either to be actively dissolved or to form the passive film is thermodynamically determined by the applied potential and pH of the electrolyte. As a result, locating environmental settings (including both potential and pH) that allow B atoms to be dissolved and A atoms to be passivated is critical to examine the percolation model.

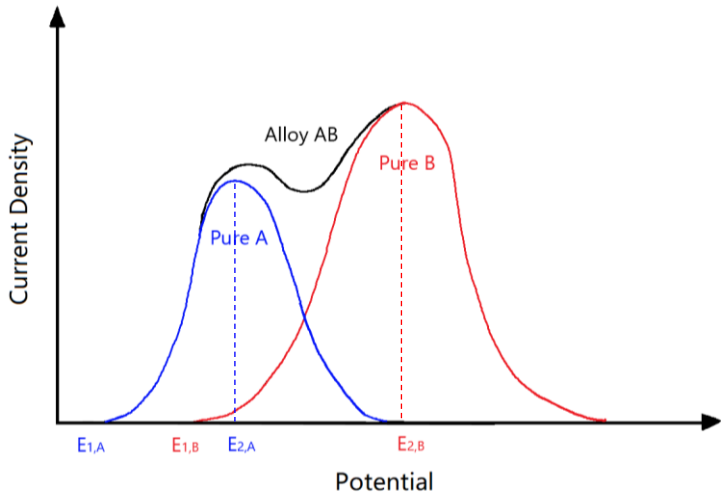

Figure 1.11 Schematic drawing of the LSV of a chuck of A(blue), a chuck of B(red), and when tieing AB(black) up without alloying. This ideally breaks down the polarization curve of binary alloy to the polarization curves of constituting elements, A and B, without considering alloying effects.

Figure 1.11 shows a schematic cartoon that decomposes the double-peaked LSV curve into two typical polarization curves of constituting elements without considering alloying effects. Here, A passivates at a lower potential than B, as A is the passivating element. An ideal potential satisfying percolation presumption lies in between $E_{2,A}$ and

$E_{2,B}$, or so-called primary passivation. However, as addressed in Uhlig's electron configuration theory, the alloying process will alter the electrochemical behavior of both A and B. For example, the passive potential of atom A surrounded by B atoms would deviate from $E_{2,A}$. This effect could be evaluated with accurate DFT calculations for the dissolution energy change of B surface doped by A and the oxidation energy shifts of A clusters surrounded by B atoms. It will be discussed in section 2.4.1 with an example of Fe-Cr alloys.

Ideally, within the so-called primary passivation region, the passive element A in a binary alloy A_pB_{1-p} is bonded with absorbed O, looking for connectivity in the film. In contrast, element B is selectively dissolved into the electrolyte, destroying the connectivity of the film. When the concentration of A, p, is below the percolation threshold, -A-O-A- bonds only form isolated A oxide clusters. The dissolution of connecting B atoms will lead to the detachment of metal particles. This phenomenon is called undercutting. Figure 1.12 circles out the undercut parts. On the other hand, once p reaches above the percolation threshold, an infinite cluster of A atoms evolves to a continuous passive film, stops the further dissolution of B atoms.

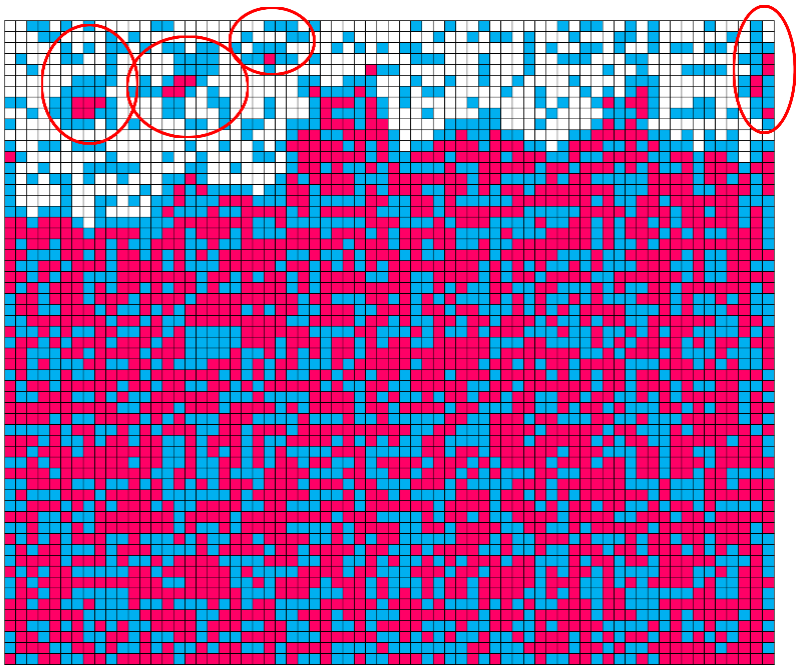

Figure 1.12. Undercutting in primary passive dissolution. Simulated 2D passivation in B(red)-A(blue) alloy with occupation probability of A atoms is 0.47. The lattice is percolated in one direction (from left to right). The circled alloy parts are undercut when surrounding B atoms are actively dissolved (become white).

In A_pB_{1-p} alloys diluted with A atoms, the distribution statistic is dominated by A monomers and dimers, which cannot serve to nucleate and will be simply dissolved, and undercutting barely occurs. As p increases, a higher density of locally percolated clusters would evolve. These isolated clusters get undercut during dissolution. Once the concentration of A reaches above the percolation threshold, a global network is developed, and the number of undercut clusters will suddenly drop. Undercutting will only exist with a small number of clusters excluded from the percolating network during the dissolution and passivation of the alloy percolated by passivation A, as shown in figure 1.12. This dramatic drop in the undercutting amount could be used to monitor the occurrence of a percolating network. The current efficiency could quantify the

undercutting phenomenon since undercut particles do not contribute to electrochemical current but are counted in other measurable parameters like mass losses.

1.5.2 Percolation

Percolation is a mathematical phenomenon dealing with the effects of composition on the richness of interconnectivity in a spatially random system. It has been applied to explain a broad range of phenomena, e.g., the electric conductivity change of metal/insulator composite over different compositions. There are two different percolation problems, bond percolation and site percolation. Site percolation problems could simply model the random binary alloys filling the lattice sites with fixed probability as atomic concentration, and is discussed here. Figure 1.13 displays a 2D site percolation process with the increasing occupancy probability, p, of black spots on square lattice sites. The black spots are scattered with little connectivity at low occupied concentration. With increasing p, some clusters of larger sizes evolve, and eventually, a network spanning the spatial directions develops – a scenario defined as percolation.

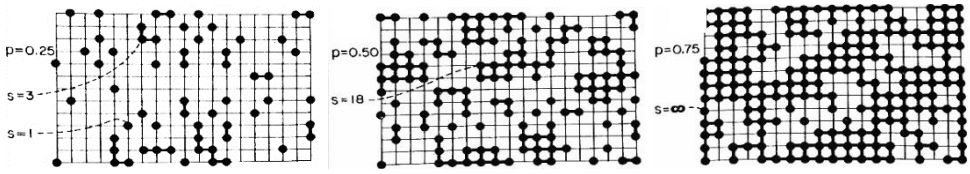

Figure 1.13. Illustration of the percolation transition in a 2D square lattice, with increasing occupancy. The distribution of atoms in random alloys is modeled by A atoms occupying the filled sites and B atoms characterized by unfilled sites B. Various-sized clusters of A atoms are identified with different values of p. From left to right, p is 0.25, 0.5 and 0.75. For p=0.75, an unbounded cluster is present.

Modeling the transition of percolation in a random A_pB_{1-p} alloy is started with randomly filling the alloy lattice and is illustrated here with the 2D square case shown in figure 1.13: choosing a site in the square lattice and occupying it by A with a probability

of p. Once a site is occupied by A, the chance of this A atom belonging to an A cluster with a size of two is 4p since there are four 1^{st} NN in a 2D square lattice. By similar arguments, the probability this occupied site belonging to a cluster with a size of 3 should be $18p^2$, and the one with a cluster size of s should be proportional to p^{s-1}. As a result, when $p << 1$, e.t. the low concentration regime, the likelihood of forming a cluster with a size of s would peak at s=1 and exponentially decay as s increases. In other words, nearly all the filled sites are monomer when p is small. One could imagine that as the occupancy, p, increases, the number of $s \geq 2$ clusters, such as dimers (s=2) trimers (s=3), will increase because the probability of an A cluster finding an adjacent site filled with A become larger so that the cluster grows in size.

However, with increasing p, it becomes more challenging to derive the distribution of cluster sizes mathematically. By contrast, computational simulations could help obtain the distribution over the full concentration range. Figure 1.14a shows how the 3D correlation length (ζ) measured in Monte Carlo simulations evolves with increasing concentration of filled sites. ζ is defined to represent the connectedness and behaves in a way as the average cluster size does. The correlation length diverges around the percolation threshold, where an “infinite” Cr cluster forms, spanning the entire sample.

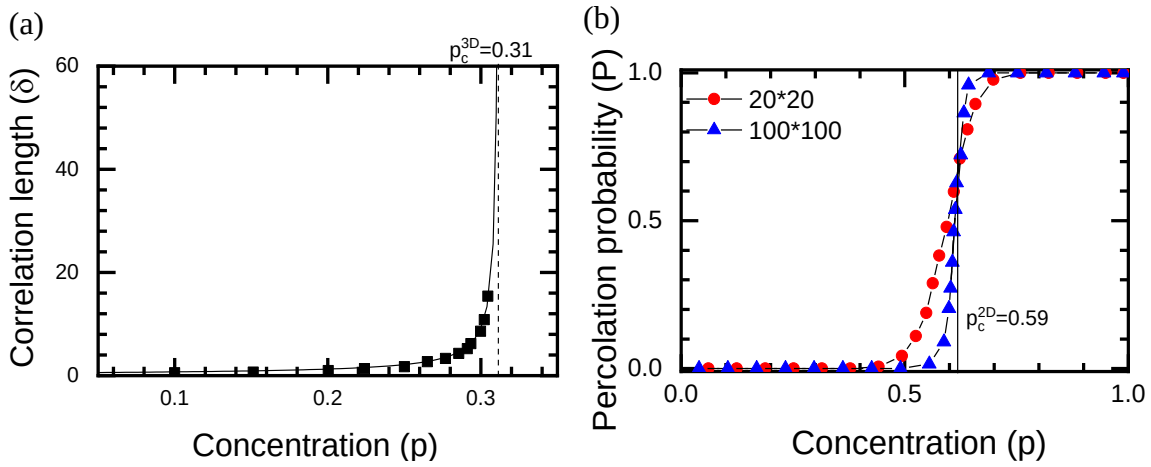

Figure 1.14. Characterization of percolation transition with computer simulations (a) The measured 3D correlation length (ζ) as a function of occupation probability, or concentration, p. The correlation length gets close to the size of the simulated lattice (1024 x 1024 x 1024) as the concentration approaches the percolation threshold[56]. (b) The percolation probability (P) versus concentration (p) curves in cases of simulations with a 20-by-20 random grid (blue) and 100-by-100 random grid (red)[54].

The way to accurately capture the percolation process with Monte Carlo simulations is introduced here. A realization is initiated with the random occupation of the lattice by A atoms with a specific probability equal to p. The lattice is examined with the percolation criteria (spanning over different directions) after the lattice is filled up. In the beginning, the cell is filled with a low fraction of A that no percolating cluster of A evolves. p is then increased until the lattice satisfies the percolation criteria. The p for percolation is recorded as the percolated concentration for this realization. With thousands of realizations, a distribution of numbers of realization over the percolated concentration could be collected and converted to a percolation probability over the concentration. Figure 1.14b shows this transition in 2D lattices with two different sized lattices[54]. A prominent trend is found that a sharper transition is obtained for the lattice of larger size. One may safely conclude that when the simulated cell size is sufficiently

large as in real alloy samples, percolation should rarely occur in the lattice with p below a threshold value p_c, and for lattice above this value, the random lattice would always get percolated.

1.5.3 2D to 3D cross-over effects

It is essential to know that the percolation thresholds, p_c^{3D} and p_c^{2D}, realized in 3D and 2D, respectively, are different from the percolation in a thin film. When applying the percolation model to alloy passivation, the 3D percolation corresponds to a passivation process that undergoes the dissolution of at least thousands of monolayers. However, it is well established that the passivation is achieved within a thin film in nanoscale. As a result, the passivating element A must span the two dimensions parallel to the passive film within the thickness of the thin film. One could imagine that percolation in a thin film requires a higher concentration of A. Thus the p_c^{3D} discussed in section 1.5.2 would only set the lower compositional limits. This section addresses the issue with the introduction of the 2D-3D cross-over effects in the percolation model.

The passivation surface is roughened with electrochemical dissolution and chemical dissolution of oxide, which could be imagined as a topological 2D surface. Figure 1.15 shows how the roughened topological surface becomes enriched in A. A "2D" percolation of A atoms evolves as the preferential dissolution of B atoms proceeds. Here, *h* is the depth of dissolution required for A to passivate the surface. If passivation is achieved within one monolayer, that is to say, a percolation network occurs on an atomically flat 2D surface, the relevant percolation threshold then increases to $p_c^{2D}\{1,2,3\}$, the percolation threshold for interactions including up to 3rd NN in 2D. The value of $p_c^{2D}\{1,2,3\}$ varies with surface orientations and crystal structures. For a BCC (100) surface, the threshold would be the same as square lattice, 29.2 at.%[55]. When *h* increases from 1 monolayer to essentially infinite, i.e., $1<h<\infty$, the threshold of

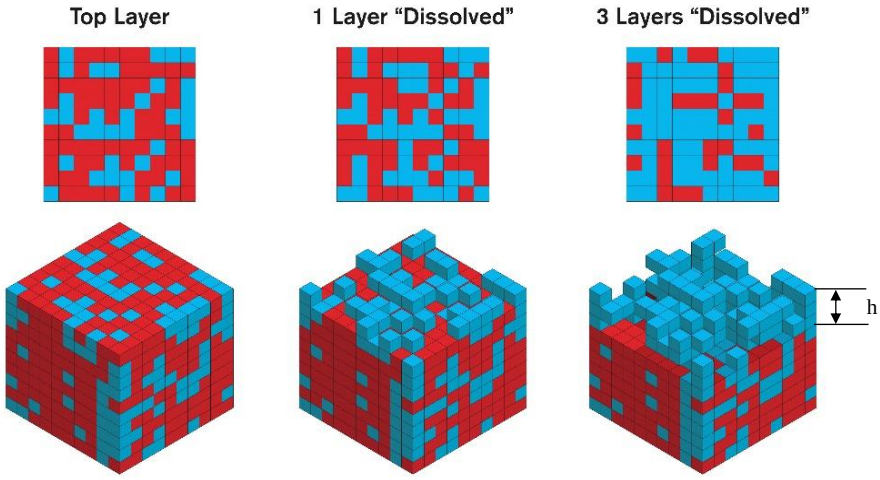

Figure 1.15. Schematic cartoon for illustration of 2D-3D percolation cross-over effects in surfaces roughed by dissolution. The top row shows the surface's plan view, and the second row gives an isometric view. The 10 x 10 x 10 lattice is occupied by A (blue) and B (red) atoms, with a concentration of A equal to 0.33. The left column shows the initial surface before the dissolution of B atoms; the middle column shows the situation after the B atoms in the first monolayer are dissolved; the right column corresponds to the scene after the dissolution of B atoms in the first 3 layers. In the case of AB alloy with 33 at.% B, a 2D percolation is realized after 3 layers are dissolved.

percolation descends from $p_c^{2D}\{1,2,3\}$ to $p_c^{3D}\{1,2,3\}$. Conversely, for A-B alloy with A concentration sitting in between $p_c^{3D}\{1,2,3\}$ and $p_c^{2D}\{1,2,3\}$, one can essentially obtain the *h* in the dissolution direction that the system needs to look for "xy-plane" connectivity.

The equation that concludes the cross over effects can be derived based on the well-known finite sample-size effects in percolation problems. The percolation correlation length, ζ , i.e., the connectivity length, depends on composition with a relation described by equation 1.2:

$$\zeta \approx \left| p_c - \mathrm{p} \right|^{-v}, \tag{1.2}$$

where v is the scaling exponent with a universal (independent of lattice type) value of ~ 0.88 for the 3D case and 4/3 for the 2D case. Since the probability to percolate a system of size h (volume h^3) is equal to the probability that a finite cluster with a radius of h appears in an infinite system, the percolation threshold for a cluster with a finite size of h should follow the equation 1.3:

$$\mathrm{h} \approx \left| p_c^{3D} - p_c(\mathrm{h}) \right|^{-v_{3D}}, \tag{1.3}$$

Through a renormalization scheme, Sotta and Long tested the capability of this equation in determining the percolation threshold for films of thickness h[56]. They started with filling up a film cell with a size of $d \times d \times h$ with occupation probability p, and then renormalized or coarse-grained the cell to a 2D lattice with a renormalized cell size of h^3. Figure 1.16a briefly displays the renormalization process of a film with a dimension of 16 x 16 x 4, every grain with a size of 4 x 4 x 4 is renormalized into one lattice. Whether the renormalized lattice is occupied or not is determined by whether the

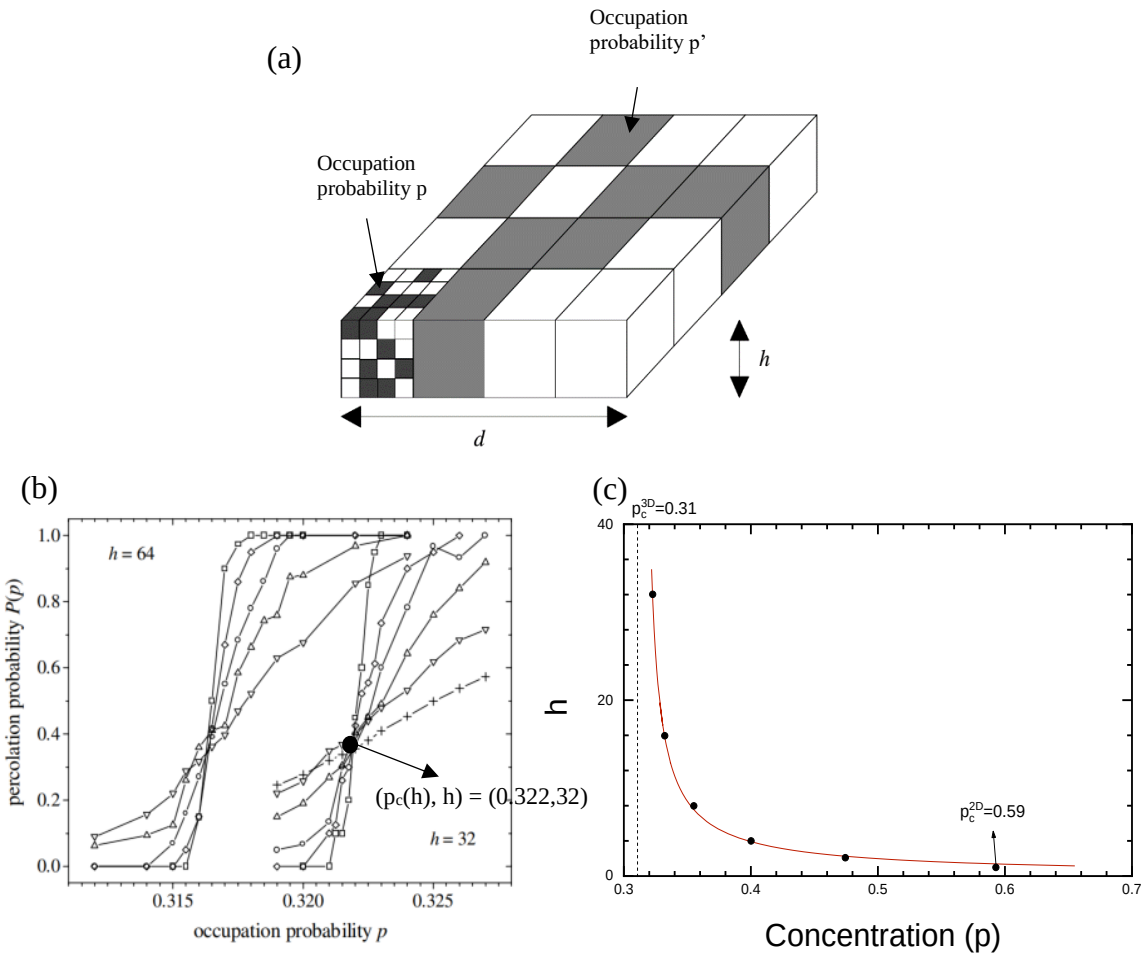

Figure 1.16. Illustrations of how Sotta and Long tested the equation, $p_c(h) \approx p_c^{3D} + \alpha\, h^{-1/\nu^{3D}}$, for 2D to 3D cross-over effects through lattice renormalization[56]. (a) Coarse-grain process of a 16 x 16 x 4 thin film into a 4 x 4 x 1 2D lattice. (b) The percolation probability curves of h = 64 and h = 32. The crossing point of curves with different d gives the percolation threshold for specific h and makes up a point in the (c) plot, which shows a decent fitting to the equation.

originally occupied lattice percolates the original grain or not. The renormalization changes the occupation probability of a cell from p to p'. And p' is a function of initial occupancy p and film thickness h, p' = f (p, h). The thin film is transformed into a 2D lattice through this process. Whether the original thin film is percolated is defined by the percolation status of the renormalized 2D lattice. For a fixed h, percolation probability

transitions over occupation probability could be collected for cells of various d through plenty of such realizations. The intersection of the curves gives to the percolation threshold for a film with a thickness of h, a $(p_c(\mathrm{h}), h)$ couple, as shown in figure 1.16b. Different (p_c(h), h) couples are obtained by change h in such numerical simulations and show an excellent fitting to the theoretically derived equation 1.4:

$$p_c(\mathrm{h}) \approx p_c^{3D} + \alpha\, \mathrm{h}^{-1/\nu^{3D}}, \tag{1.4}$$

with numerically fitted prefactor α in order of unity (figure 1.16c). The capability of this mathematical equation to describe the 2D-3D transition is verified, and thus the equation is used to predict the film thickness transition in the percolation model.

1.5.4 Atomic configuration effects on percolation and passivation

The previous section addresses how the concentration of the passivating element in a random alloy affects the percolation in the thin film and thus the passivation behaviors of the alloy. However, most solid solutions in thermal equilibrium do not exhibit perfect randomness. Instead, some degree of deviation from a random solution to ordering or clustering is usually present due to the interactions between constituent atoms. In a regular solution model, the enthalpy of mixing is calculated through equation 1.5:

$$\Delta H_{mix} = Z\Delta E X_A X_B, \tag{1.5}$$

where Z is the number of nearest neighbors; $\Delta \mathrm{E} = [\mathrm{E_{A-A}} - 1/2(\mathrm{E_{A-A}} + \mathrm{E_{B-B}})]$, defines the interaction parameter of the lattice; X's correspond to the atomic fraction of the constituent elements. The Gibbs free energy is given by,

$$\Delta G_{mix} = \Delta H_{mix} - T\Delta S_{mix}, \tag{1.6}$$

where T is the temperature, ΔS_{mix} is the mixing entropy. ΔH_{mix} defined by equation 1.5 determines the trend to clustering (A, B atoms are attracted to each other) or ordering (A, B atoms are repelling to each other), both of which are non-random configurations. The equilibrium temperature, from which the atomic configuration is frozen by quenching, on the other hand, tunes the randomness of the alloy. Schematic cartoons for the three atomic configurations are displayed in figure 1.17.

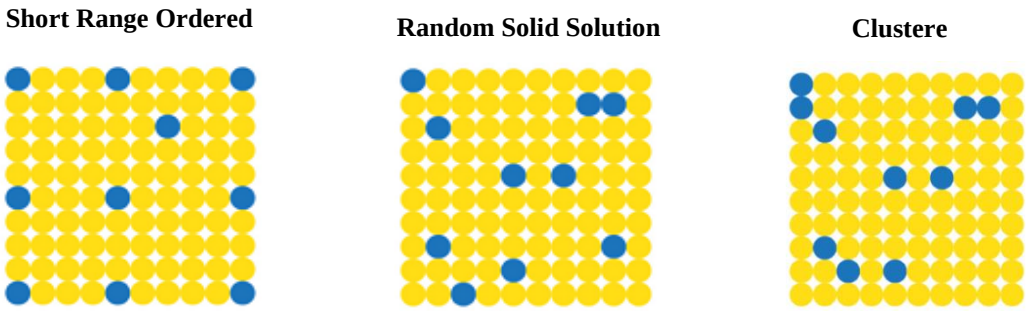

Figure 1.17. Cartoons of the surface of alloy AB with different atomic distributions: random solid solution (middle), short range ordered (left), and clustered (right). Blue and yellow circles represent A and B atoms.

When considering the kinetic impact during alloy preparation, the atomic distribution in real alloys could be far off the thermodynamic equilibrium described by the theoretical equations shown above. However, the atomic configuration could be experimentally measured by scattering techniques or extended x-ray absorption fine structure (EXAFS). On the other hand, the impact of the atomic configuration on the percolation threshold could be computationally simulated with large cell Monte Carlo renormalization group (MC-RNG) methods. These results would then allow for the determinations of p_c^{3D} of ordering/clustering alloys and thus predictions of the corresponding passivation behaviors.

CHAPTER 2

PASSIVATION OF FE-CR ALLOYS

As a fundamental subsystem of stainless steels, Fe-Cr alloys are one of the most significant alloy sets from an industry perspective and have drawn the most attention in corrosion science. Fe-Cr alloys with sufficient (above 10-13 at. %) Cr exhibit excellent corrosion resistance, even in strongly acidic electrolytes. The alloys with Cr content below the critical composition exhibit corrosion behavior similar to Fe, while alloys with higher Cr concentration passivate in the way pure Cr does. In this chapter, the passivation behavior of Fe-Cr binary alloys, as the simplified binary alloy system from stainless steel, is carefully analyzed to examine the application of the percolation model in determining the critical composition of passivating element for a protective passive film.

2.1 Background

The critical role the passive film plays in the passivation is generally acknowledged. The compositional and structural properties of the passive film developed at the Fe-Cr alloys/aqueous media interphase have been extensively investigated using electrochemical techniques, scanning probe, and surface science spectroscopy techniques in-situ and ex-situ[21,22,34,35,44–47,49,57,58]. It turns out these passive film properties vary with environmental settings, such as applied potential and pH of the electrolyte, and evolve with time. The absolute values obtained by different investigators sometimes are far from the comparison. Still, good agreement is reached on the qualitative transitions of the film features over the conditional parameters:

(1) With increasing Cr content, the crystalline passive film developed on the Fe-Cr alloy surface vanishes and transits to an initially amorphous film[22,35]. Amorphous

passive film is also observed on the outer $Cr(OH)_3$ layer formed on elemental Cr, with inner Cr_2O_3 in nanocrystalline structure[18]. By contrast, in-situ STM demonstrates a nanocrystalline nature of the passive film developed on elemental Fe[8–10]. The inner layer consists of primary Υ-Fe_2O_3 mixed with some Fe_3O_4 and is covered by a hydrated outer layer, Υ-FeOOH[8,11]. The initial amorphous film on Fe-Cr alloys developed on alloy with higher Cr concentration would self-crystallize overtime under polarization or in air[21]. Based on these observations, the percolation model envisions a scenario that a hydr(oxide) gel network develops via the connection of amorphous -Cr(OH)-O-Cr(OH)- bonds during the initial Cr oxidation. The increasing Cr concentration in the alloy increases the proportion of $Cr(OH)_3$ in the film, a more amorphous film being developed. In other words, the increasing disorder in passive film developed on alloys with higher Cr composition indicates a growing contribution from Cr. The self-crystallization with time is interpreted by a dehydration process of amorphous $Cr(OH)_3$ gel transiting to the crystalline Cr_2O_3 [42].

(2) It is observed that the remarkable enrichment of Cr in the passive film is suppressed by increasing applied potential and electrolyte pH. The pronounced Cr enrichment in the passive oxide films compared with alloy substrate is generally observed during the passivation of Fe-Cr alloys in acidic electrolytes. The Cr enrichment in passive film over parent alloy has been identified in the initial stage of passivation within several seconds. It accumulates over time, suggesting a heavier dissolution of Fe oxides than Cr oxides[59]. The percolation theory interprets the pronounced enrichment as originated from the primary passivation process, where Cr atoms remain on the surface and participate in the formation of the passive film, while most of the Fe atoms are selectively

dissolved into the electrolyte except those bridged or adjacent to the Cr oxide formation nuclei being incorporated into the film.

The degree of Cr enrichment varies with different experimental conditions, such as electrolytes and applied potentials[34,44,45,53]. With increasing applied potential or pH, the Fe/Cr ratio in the film tends to approach the bulk alloy composition, indicating a growing Fe contribution to alloy passivation. The electrochemical behavior of pure Fe and Cr can explain this decreasing Cr enrichment with the increasing applied potential and electrolyte aggressiveness. Unlike passivation achieved by Cr, the passivation of Fe in strong acid is initiated by local saturation of Fe^{2+} accumulated by high dissolution rates, followed by the precipitation of passivation precursor, i.e., an unstable porous ferrous salt film[60,61]. More anodic potential above Flade potential (0.58V at pH=0) stabilized the "passivation" with the growth of Υ-Fe_2O_3. In Fe-Cr alloys, much lower current density limited by Cr passivation kills the probability of ferrous salt precipitation. The Fe ions generated by the lower dissolution rate are highly free to diffuse towards bulk electrolyte. Fe participates in passivation only when passive Fe oxides stably develop. Before that, only Cr oxides are responsible for passivity. With increasing potential, the chance of stable Fe oxide remains in the passive film increases, decreasing the degree of Cr enrichment in the passive film. The pH-dependent Cr enrichment in passive films can be partly reasoned because the Fe oxides are more vulnerable to the aggressive electrolyte, with the observation that Fe shows a higher passive current than Cr[62,63]. The reasons behind this could be traced from the thermodynamics that Fe oxide is less stable in solutions of lower pH.

In other words, the more participation of Fe in passivation at higher pH will alleviate the requirement for Cr percolation and thus decrease passivity thresholds. That a higher pH increases the contribution from Fe to passivity is also reflected by the various critical thresholds reported in the plots of the critical current density and passivation potential transition over Cr composition under different pH. The critical composition for alloy passivation is not always reported with the same value but remains controversial — the well-accepted threshold of 13 at.% Cr in Fe-Cr alloys was supported by the transition of current density and passivation potential over Cr composition in a strong sulfuric acid (pH=0)[25]. In comparison, a sharp transition has been identified around 5 – 8 at% in the critical current density transition over Cr concentration in neutral sulfate solutions[24].

On the other hand, the critical value for alloy passivation could change with different defining criteria. Keddam measured the steady-state polarization curves and classified Fe-Cr alloys into Fe-like group, transition group, and Cr-like group based on the number of current maxima. He set the two compositional terminals dividing the three groups as the critical Cr at.% threshold. A similar change in the two terminals are noticed when he changed the pH: increasing pH lowers both Cr at.% terminals. Keddam claimed that the Cr content in the Fe matrix played a similar role as the OH^- in the solution[64].

The percolation model only considers the connectiveness of Cr atoms in the alloy and is constructed with the assumption that Fe is preferentially dissolved and minimally participates in passivation. The influence of environmental conditions on alloy passivation is addressed by the relative contribution from the constituent elements, just as Qian altered the dissolution possibility in KMC simulations[39,40]. An ideal examination of the percolation model would require accurate identification of the primary passivation

region. Firstly, the experiments are preferred to be conducted in strong acid to increase Fe dissolution and suppress Fe passivation. Additionally, online ICP-MS is employed along with LSV to monitor the Fe/Cr dissolution ratio in the electrolyte at different potentials. The primary passivation region where Fe is favorably dissolved and Cr prefers to get passivated could be identified.

On the other hand, as addressed by Uhlig, alloying with Fe will attenuate the affinity of Cr to O, thus the Gibbs energy for the formation of -Cr-O-Cr- bond. The potential to passivate Cr clusters in the Fe matrix is expected to deviate from pure Cr. The degree of the deviation should depend on the size of Cr clusters. The percolation model focuses on the geometric connectiveness in alloy with little emphasis on this electronic effect, but the questions would be cleared out with DFT calculations.

2.2 Experiments

2.2.1 Sample preparation

A series of Fe-Cr alloys with various compositions (5.3%, 7.0%, 9.4%, 11.6%, 14.7%, 16.8%, 17.4%, 20.2%, 22.2%, 24.3%) were prepared by melting corresponding pure elements (99.85% Fe, and 99.99% Cr Goodfellow) in vacuum induction furnace. For electrochemical analysis, the specimens were fabricated as cylinders of 5 mm diameter by electrical discharge machining. Energy dispersive spectroscopy (EDS) verified alloys compositions after machining. Heat treatment was conducted with specimens sealed in quartz tubes with an atmosphere of Ar+5% H_2 after abraded to 1500-grid finish. The specimens were homogenized at 1100 °C for 24 h. The following water quenched to room temperature assumedly gives alloys in the forms of a random solid solution.

Immediately before each experiment, the specimens were polished with silicon carbide paper of progressively finer grades and diamond suspension to particle size of 1μm.

The phase diagram of the Fe-Cr system is shown in figure 2.1[65]. Austenite alloy (γ phase) with FCC structure is not stable at low temperature and can quickly transform to BCC ferritic structure (α phase) without much diffusion during quenching. The conventional Fe-Cr phase diagram shows a thermodynamically favored spinodal region. For example, phase separates at 600 ℃ for Cr composition in ~ 22 – 46 at.%. This transformation is exceptionally sluggish in kinetics. It was experimentally observed that the Fe-Cr alloys deep in this region showed phase separation over the thermal aging but

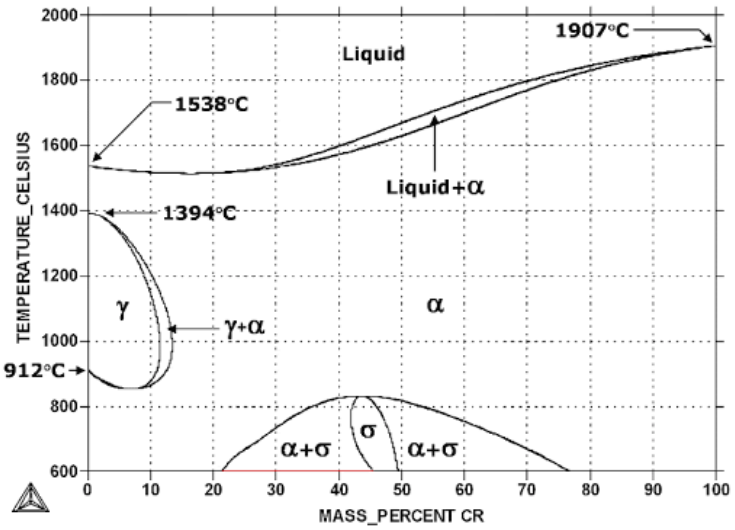

Figure 2.1. The conventional phase diagram of FeCr binary alloy[65].

with extremely slow kinetics, e.g., only 2% of the Fe-20 at.%Cr alloy transformed to two phases when annealed at 475 ℃ for 50 hr[66]. This phase separation is supposed to be suppressed by our high cooling rate of quick quench from the high homogenization temperature.

2.2.2 Electrochemical experiments

Linear sweep voltammetry (LSV) and chronoamperometry were collected with a Gamry series-G potentiostat at room temperature. All the experiments were conducted with the electrolyte of de-aerated 0.1 M H_2SO_4, if not specified. Deaeration was accomplished by bubbling with UHP N_2 just before the experiments. The specimens were mounted into the holder of a rotating disk electrode system, left with only the cross-section with a surface area of 0.2 cm^2 exposed to the electrolyte. Platinum mesh and a Mercury-mercurous sulfate electrode (MSE) were used as the counter electrode and reference electrode. All potentials are reported relative to the standard hydrogen electrode (SHE), if not specified.

The air-formed oxide was electrochemically reduced with a reduction protocol of -0.76 V for 300 s, -1.26 V for 3 s, and -0.76 V for 60 s, immediately following the immersion of the working electrode in the electrolyte. Before initiating experiments, the potential was first switched to -0.36 V for 10 s, during the time UHP N_2 was used to blow the hydrogen from the surface. All experiments proceed with N_2 flow maintained above the solution. In order to measure the charge density required for primary passivation, chronoamperometry was conducted with alloys held at particular potentials until the final current density was low enough that the integration of longer time would not have contributed more than one percent to the charge density: i.e., 100 s.

2.2.3 Computational simulations

DFT calculations were conducted with the Vienna Ab-initio Simulation Package (VASP, version 5.4.4)[67], with the exchange-correlation interactions approximated by Perdew-Burke-Ernzerhof (PBE)[68]. The electron-ion interactions of O, H, Cr, and Fe

atoms were described with the projector-augmented wave (PAW) method developed by Blöchl[69]. Spin-polarized calculations were performed to consider the magnetic properties of Fe and Cr. In the approximation of electron wave functions, the plane-wave cutoff energy is set to 450 eV. With reciprocal space sampled by 15 x 15 x 15 Monkhorst-Pack k-point grid[70], we obtained an optimized lattice parameter of 2.83 Å for BCC Fe unit cell (the experimental value is 2.87 Å) and 2.84 Å for BCC Cr (the experimental value is 2.91 Å). The calculated magnetic moment of Fe in equilibrium lattice constant is 2.195 μ_B, well matching the experimentally observed value of 2.22 μ_B[71]. For Cr bulk, an antiferromagnetic ground state was found with a magnetic moment of 1.02 μ_B per atom.

The (110) and (100) surfaces were simulated by 2 x 4 and 4 x 4 7-layer slab models separately. The surface slabs were separated by a vacuum spacing of 20.0 Å, which has been shown to be sufficient so that the image interactions from the periodic boundary conditions could be avoided. Integrations in the reciprocal space were performed with a 3 × 3 × 1 k-point grid generated by the Monkhorst-Pack method. We replaced Fe atoms in the top layer of the Fe surface with Cr atoms to simulate the surfaces of Fe-Cr alloys. The on-surface O_2/H_2O adsorption was modeled with various alloy surfaces combined with different initial (top, bridge, hollow) adsorption sites. The O_2 molecule was aligned parallel to the defined surface, while the H_2O molecule sits perpendicularly to the surface with two H atoms sticking up. The initial bond length and angle of O-O in O_2 and H-O-H in H_2O was obtained after the molecules are relaxed in a cubic vacuum superlattice with a size of 5 Å. The initial distance between the centers of O in O_2/ H_2O and the first layer of the surface was set to 2.0 Å. The structural relaxations

were performed, allowing the atomic coordinates in the different systems to relax until the residual forces are lower than 0.01 eV/Å.

2.3 Passivity of Fe-Cr alloys

In this section, the alloy passivation promoted by the gradual addition of Cr was characterized by LSV. The critical current density and passivation potential were collected as a function of Cr at.% to trace the critical Cr composition for Fe-Cr passivation. A critical value is also collected by the current transient under a located primary passivation potential. The LSV for alloys with different Cr contents was reproduced by KMC simulations that isolate geometric consideration, addressing the importance of Cr connectiveness in the parent alloys. Furthermore, the properties of the passive film developed on the alloy were studied with extended CV and reduction experiments.

2.3.1 Experimental Linear Sweep Voltammetry

The LSV behaviors of Fe-Cr alloys with different compositions we obtained in 0.1 M H_2SO_4 are shown in figure 2.2a, well matching those reported by Dobberlaar *et al.* [72], Karchheim *et al.* [73], and El-Basiouny *et al.* [74]. For alloys with a composition of 12 at.% and below, the curve is characterized by two peaks and sluggish passivation in

the "Fe-like" way. In contrast, alloys with higher Cr compositions behave more "Cr-likely" without a significantly sized second peak. A secondary passivation process is identified in the transpassive region for the alloys containing lower Cr content.

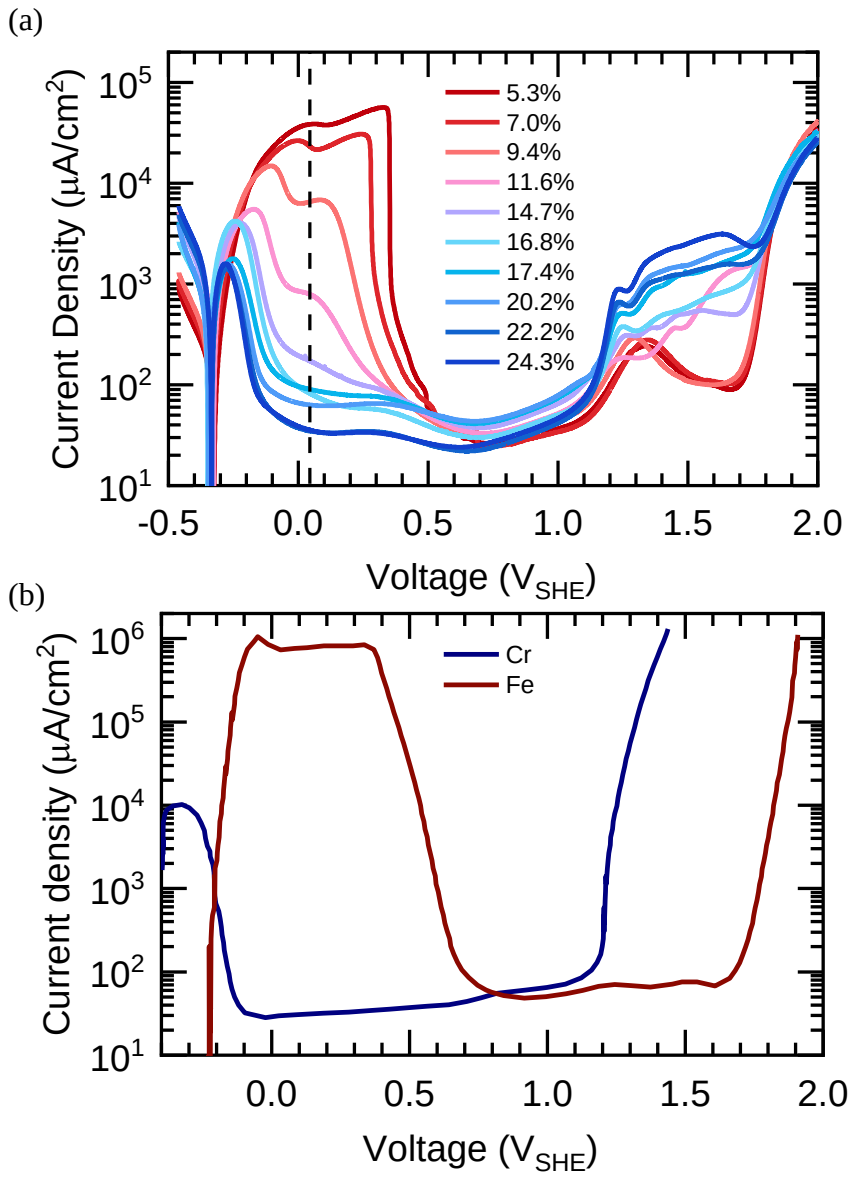

Figure 2.2. LSV curves of Fe-Cr alloys and pure metals[109]. (a) Linear sweep voltammetry results of Fe-Cr alloys with Cr concentration of 5.3%, 7.0%, 9.4%, 11.7%, 14.7%, 16.8%, 17.4%, 20.2% and 22.2% in 0.1M H_2SO_4 (the scanning rate is 5 mV/s). (b) Anodic polarization curves of pure Fe (brown) and pure Cr (blue) in 0.5M H_2SO_4. Scanning rate: 1 mV/s.

The electrochemical behaviors of Fe-Cr alloys can be better understood when compared with the LSV of pure metals. As shown in figure 2.2b, the dissolution current of pure Cr surges when the electrode is polarized above 1.1V, a potential far below the potential of O_2 evolution. Following the thermodynamic indicated in the Pourbaix diagram, the steep current increase could be associated with the reaction that Cr_2O_3 is further oxidized to soluble Cr^{6+} species[75], CrO_4^{2-}, $Cr_2O_7^{2-}$. By contrast, Fe oxides remain thermodynamically and kinetically stable until the applied potential reaches 1.7 V, where O_2 starts to evolve, and Fe_2O_3 is dissolved as FeO_4^{2-}. The current increment of Fe-Cr alloys begins around the same potential in the transpassive region as pure Cr does. As a result, this current increase of Fe-Cr alloys is more likely to be related to the transition of Cr^{3+} to Cr^{6+}.

As discussed in section 2.1, the passive film developed on Fe-Cr alloy is enriched with Cr oxides due to the selective dissolution of Fe. When entering the transpassive region, Cr_2O_3 starts to be selectively oxidized and transpassively dissolved into electrolyte while the Fe oxides maintain stable in the film. The passive film is expected to transform from originally Cr enriched passive film into a film enriched with Fe oxide. This pronounced composition change of the passive film when entering the lower transpassive region has been well recorded by different characterization techniques[45,76]. Figure 2.3 records the film properties' change of Fe-20 at.% Cr over passive-transpassive transition by monitoring a physic property, $\hbar\omega$, measured by modulation spectroscopy[77]. The $\hbar\omega$ value suddenly changes from a value close to that of pure Cr to a value near that of Fe when the potential exceeds 0.6 V, where the current

density in the corresponding LVS curve starts to rise, indicating a transition from "Cr-like" passive film to "Fe-like" one.

However, the electrochemical stability of Fe oxides is not the only requirement for the appearance of a passivation peak in the transpassive region. The geometric connectiveness of Fe oxide is also required when Cr_2O_3 is transpassively dissolved. A passivation peak can be observed in the transpassive regime when the left Fe oxides can

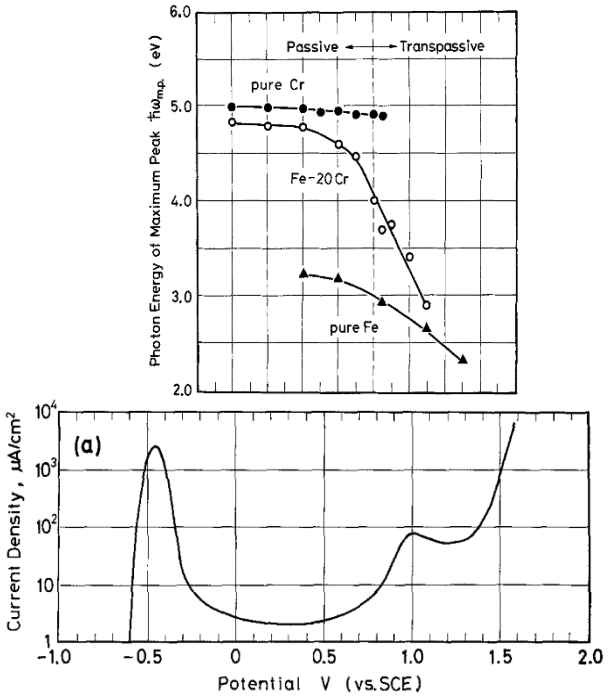

Figure 2.3. Film property changes of FeCr alloys with potential in the transpassive region, compared with pure metals[77]. The photon energies of the maximum peaks in modulation reflection spectra for the film developed on pure Fe (solid triangles), Fe-20 at.% Cr (hollow circles), pure Cr (solid circles) electrodes in 1M Na_2SO_4 (adjusted to pH 2.0 by adding sulfuric acid) change as a function of potential in passive-transpassive transition. The corresponding LSV of Fe-20 at.% Cr alloy is also attached for reference.

protect the underlying metal from further transpassive dissolution of Cr with a percolating network. This condition holds for alloys with lower Cr concentration, of which the passivation is achieved with more contribution from Fe atoms so that the

developed passive films contain a connective Fe oxide network. As Cr concentration in the alloy increases, the increasing transpassive current corresponds to an increasing Cr content in the passive film. Cr alone could achieve passivation with little Fe incorporated in the passive film in the alloys with Cr composition above the critical composition. In this case, the transpassive dissolution of Cr_2O_3 will destroy the protections of the film. As a result, no secondary passivation is observed. The connectiveness of ions in the film has already been addressed by Graph theory.

As shown in figure 2.2, the division of the examined alloys by the existence of passivation peak in the transpassive regime shares the same composition range as the division by the number of active-passive transition peaks. Based on the above discussion, one may naturally relate the two dissolution peaks in active-passive transition with the passivation of Cr atoms and Fe atoms in the alloy, separately. For alloys with Cr composition below the threshold, Cr atoms attempt to passivate the surface by forming oxides and hydroxides with absorbed H_2O and O_2 in the primary passivation region, which corresponds to the first peak. Without a protective film developed by sufficient Cr, selective dissolution of Fe atoms persists until Fe passivation eventually occurs, resulting in the second peak. While, for higher Cr-contained alloys, the primary passivation of Cr alone completes the protection for the surface so that the second peak vanishes. A negative shift of both two peaks is observed with increasing Cr concentration. We attribute this phenomenon to the electrochemical behaviors of both Cr and Fe atoms altered by alloying, which is addressed by Uhlig's electron configuration theory.

As the primary passivation by Cr is focused on, the transition of critical current density as well as passivation potential of the first peak as a function of Cr composition is studied. Figure 2.4a shows the critical current density decreases as Cr content increases. It is found that the majority of the reductions are achieved before the Cr composition reaches 10 at.%. As a result, with the solution of 0.1 M H_2SO_4, we could expect a percolation threshold around this value. The potential of the first peak, which comprehensively represents the passivation potentials of various Cr clusters in the alloys, gradually decreases to a value close to the passivation potential of pure Cr, -300 mV, as shown in figure 2.4b. This transition will be compared with the results from DFT calculations in section 2.4.1.

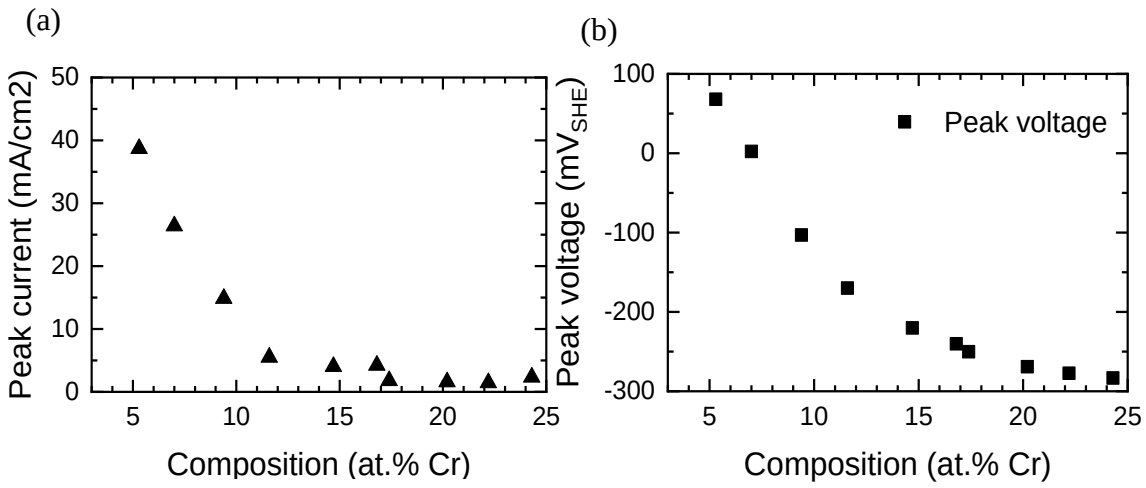

Figure 2.4. The changes of (a) critical current and (b) potential of the first peak as a function of Cr concentration are collected from the LSV curves of Fe-Cr alloys in figure 2.2a.

The effect of pH is studied with the LSV of Fe-Cr alloys in sulfuric solutions with various pH, as shown in figure 2.5. With increasing pH, both Cr dissolution and Fe dissolution are suppressed to a lower critical passivation current. A more critical role Fe playing at higher pH could be identified according to the change of the relative height of two passive peaks and the passivation in the transpassive region. The alloy with 5.3 at. % Cr even shows no transpassive dissolution of Cr oxide with no apparent current increase until the voltage reaches the O_2 evolution from H_2O in the transpassive region like pure Fe, indicating the active-passive transition is achieved with negligible contribution from Cr. On the other hand, a narrower primary passive region (the potential difference between two peaks) is observed for curves collected in higher pH, supporting our previous conjecture that stronger acid is a better environment for examining the Cr percolation in the alloy matrix.

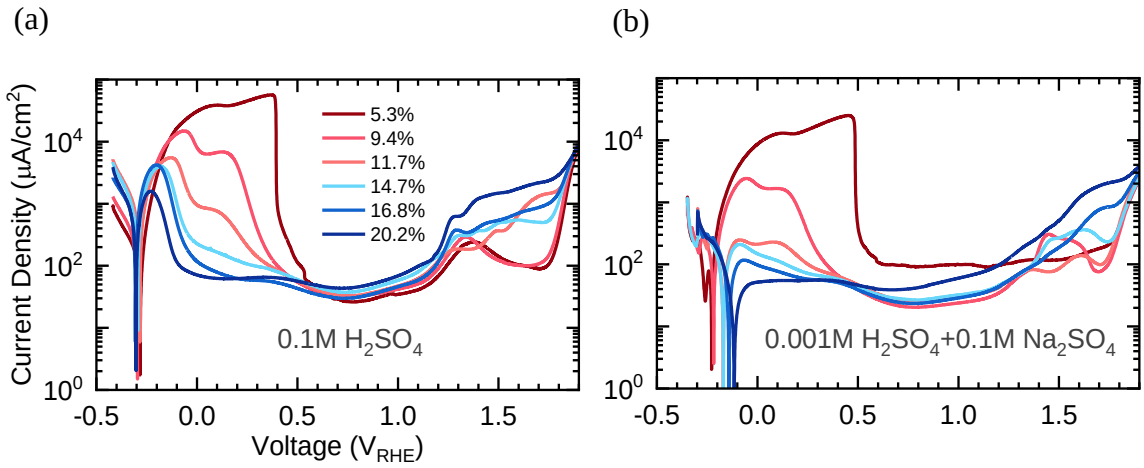

Figure 2.5. The LSV of Fe-Cr alloys in 0.1 M H_2SO_4 (a) and 0.1M Na_2SO_4 + 0.001 M H_2SO_4 (b). The figure is plotted with RHE for comparison so that the pH effects (cathodic shift of -60 mV/pH) could be simply excluded.

2.3.2 Simulated Linear Sweep Voltammetry

KMC simulations were conducted to address the impact of geometric connectivity of Cr in the parent alloys on primary passivation. No surface diffusion of either Fe or Cr is considered for the atom redistribution with the fact that the upper limit of the surface diffusivity, D_s, of either Cr and Fe at room temperature is in order of 10^{-20} cm^2/s, while the experimental dissolution rate is in order of 1 mA/cm^2, which means dissolution of 0ne monolayer takes about 0.5 s. The diffusion distance estimated by $\sqrt{D_s t}$ is less than 10^{-10} cm. The simulations model the scenario of primary passivation, where Cr atoms passivate while Fe atoms are dissolved. Blocking of dissolution, or passivation, is realized in clusters with two or more Cr atoms. To capture the incorporation of Fe in the mixed oxide film, the Fe atoms neighboring the passivating Cr atoms are also passivated. Cr atoms from Cr-O-Cr "mer" unit chain ends are subject to chemical dissolution with rates equal to 0.05 s^{-1}. The change of the electrochemical behaviors of constitute elements during alloying is ruled out in the simulations. The dissolution kinetics of isolated Cr monomers, as well as the other Fe atoms, follow equation 2.1:

$$k_{diss} = \nu_{diss} exp[-(nE_b - \phi)/k_B T], \quad (2.1)$$

where ϕ is the applied voltage; E_b is the bond energy equal to 0.075 eV; and ν_{diss} is an attempt frequency for all alloy compositions equal to 10^4 s^{-1}.

Figure 2.6 shows the LSV curves obtained by KMC simulations. With a finite thickness of the simulated cells, the lattice cell occupied with Cr concentration below 11 at.% were dissolved through before passivation. For alloy with a concentration above the value, active to passive transitions were observed. Compared with experimental results, no two-wave character was observed during the KMC simulations. The absence of the second peak in simulated LSV partly supports our assignment of the second peak to the passivation of Fe atoms since no passivation is considered for Fe atoms in KMC simulations.

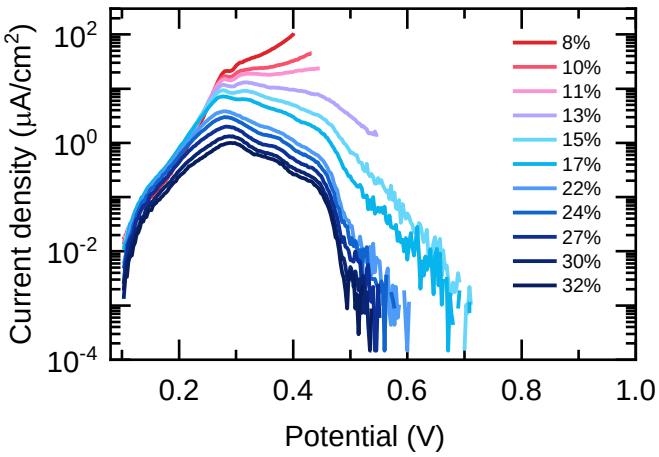

Figure 2.6. The active-passive transition behavior of Fe-Cr alloys obtained by KMC simulations with a sweep rate of 1 mV/s. The KMC simulations were conducted by Dorota M. Artymowicz.

2.3.3 Property of passive films

As discussed in the previous section, a more stable passivity evolves with extending time and increasing voltage. Extended Cyclic Voltammetry (CV), shown in figure 2.7, helps identify the different properties of passive films when developed with different anodic scanning limits. Figure 2.7a shows a surface state closer to the active surface that allows active dissolution in the reversed scan. Based on the active-passive transition peak of the second cycle, passivation can be divided into two states: the surface passivated with lower anodic limits is characterized with a CV that no dissolution in the reverse scanning is identified, but the second cycle could follow the trace of the first

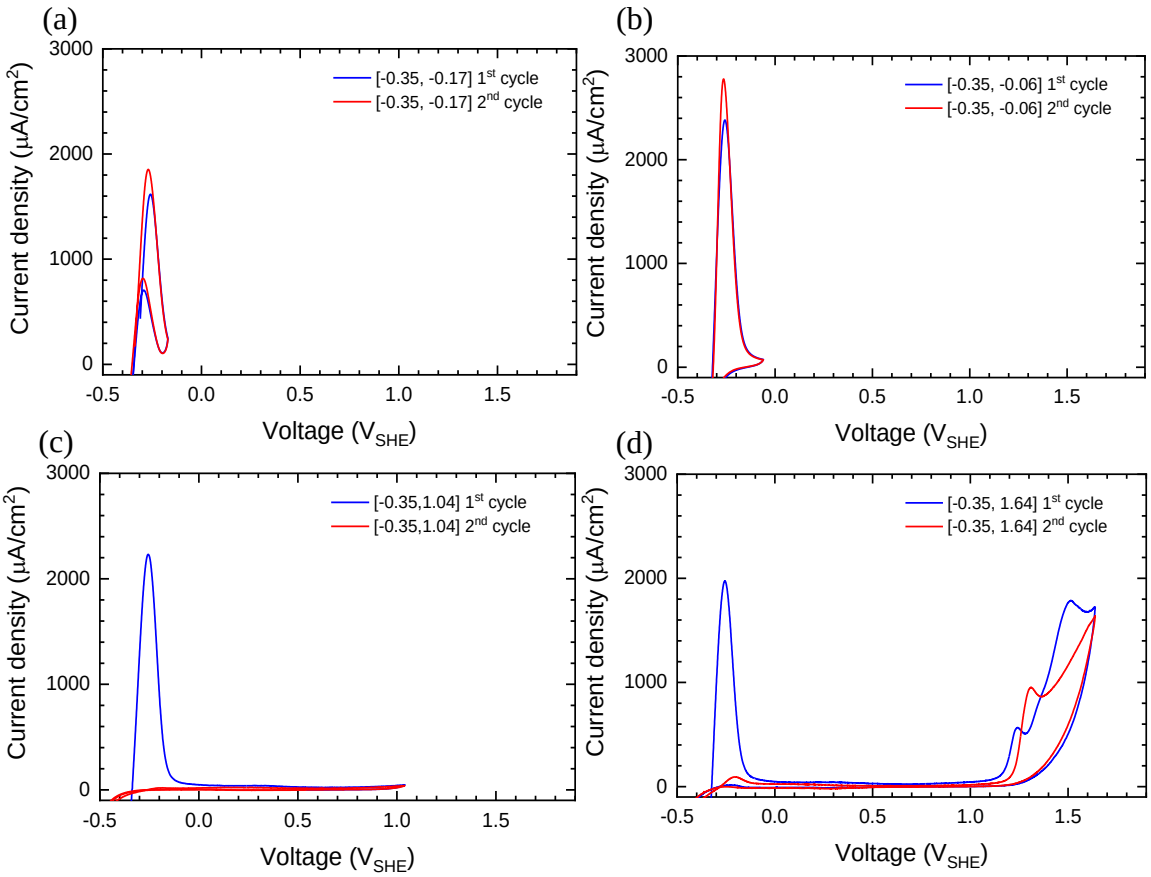

Figure 2.7. The 1st (blue) and 2nd (red) cycle of CV with different scanning ranges of Fe-20.2 at.% Cr alloy in 0.1 M H2SO4. The scanning rate is 10 mV/s.

cycle, as shown in figure 2.7b; the other passivated surface shows no reproducibility of the second cycle in CV, as in figure 2.7c; further increasing potential into transpassive regime recovers the transition peak of the second cycle a little bit, probably because the transpassive dissolution of Cr oxides destroy the original passive state and Cr enrichment, which is repaired by the transition peak in the following scanning, as shown in the figure 2.7d. The evolution of different surface states is supposed to depend on both applied potential and time, while voltammetry mixes the impact from these two.

To address the role applied potential plays in the evolution of passive film, the electrode surface is firstly anodized with a fixed time, 400 s, the passive film developed is then reduced with a fixed cathodic current density of 2.5 $\mu A/cm^2$. After the passive films are developed under various potentials or for alloys with different compositions, the stability of the films is quantitively analyzed by the potential arrests shown in the reducing chronopotentiometry.

Figure 2.8a shows a typical galvanostatic reduction curve we obtained, the decay of potential with time is an indication of the film being progressively broken down. By differentiating the potential change with time, three potential arrests are highlighted by the local minima in the decay rate (figure 2.8b). Two reduction peaks at 0.49 V and 0.14 V have been observed in the reverse CV of Fe-23 at.% Cr in 0.1 M acetate solution with pH of 4.5[34], as shown in figure 2.8c, and were corresponded with reduction of Cr^{6+} in the nearby solution to Cr^{3+} and Fe^{3+} in the oxide to more dissolvable Fe^{2+} when compared with the CV of pure metal. The first two voltage arrests we observed could align with these two reactions. The minor difference in the arrested potential could be caused by the

different pH and scanning rate we employed. As for the last potential plateau, it could correspond to the evolution of H_2.

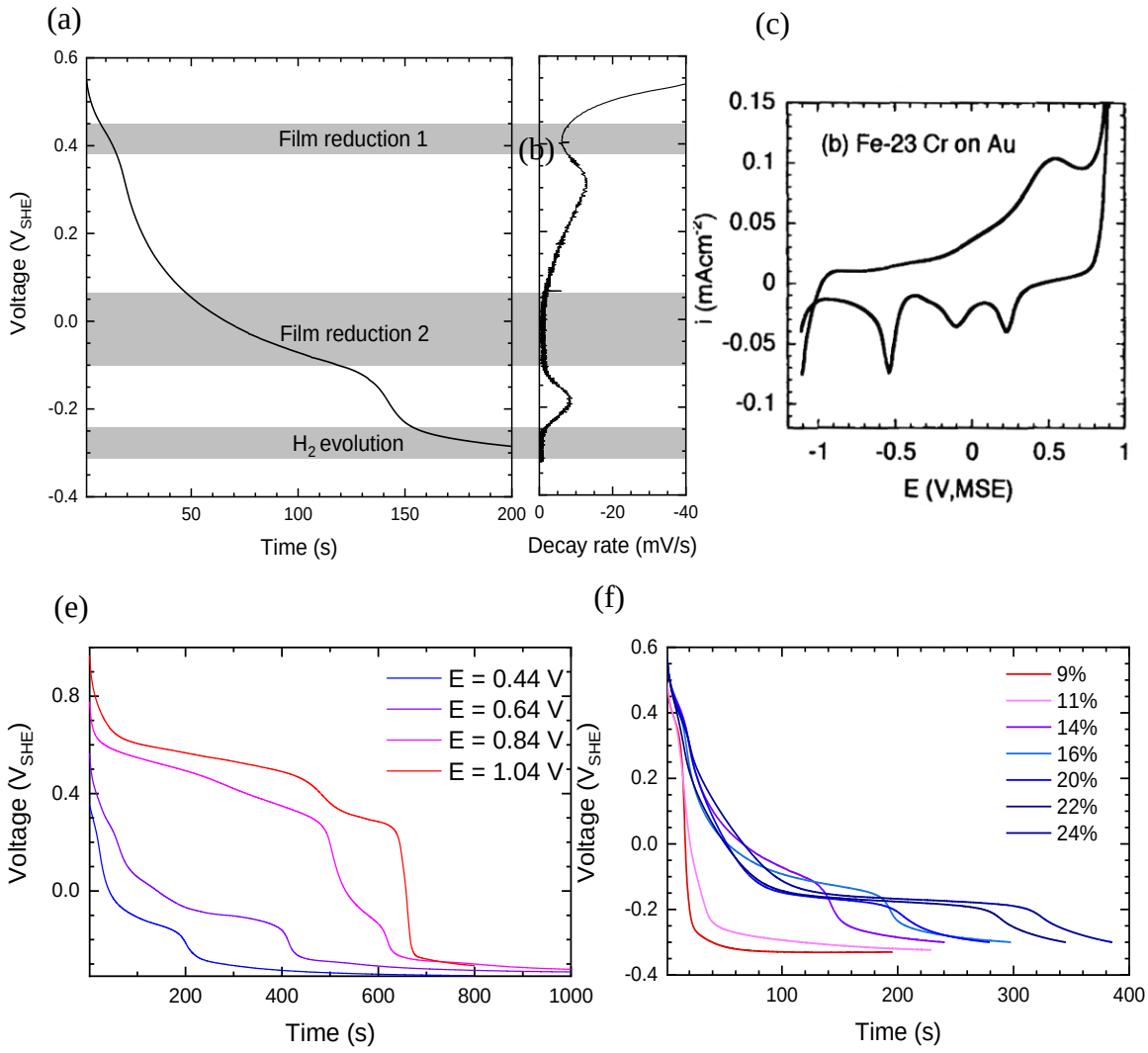

Figure 2.8. Potential profile of the cathodic reduction of passive films. (a) Potential decay of Fe-14 at.% Cr, when applied with a cathodic current of 2. 5 μA/cm^2 after passivation at 0.64 V for 400 s. (b) The polarization curve of Fe-23 at.% Cr film on Au substrate in a de-aerated solution of pH 4.5, with a scanning rate of 10 mV/s. The peak around -0.1 V_{MSE} corresponds to the reduction of Au. (e) Potential decay profiles of Fe-20 at.% Cr when applied with a cathodic current of 2. 5 μA/cm^2 after passivation at the various potential for 400 s. (f) Potential decay profiles of different alloy compositions when applied with a cathodic current of 2. 5 μA/cm^2 after passivation at 0.64 V for 400 s.

We do not observe a pronounced reduction peak in our CV, probably because the more acidic setting of ours leads to the chemical dissolution of a higher rate so that the electrochemical conversion cannot catch up. The time for the potential arrest should reflect the amount of reactant since the reduction current is fixed. Figure 2.8e demonstrates the impact of passivation potential on the composition of the passive film. Passivation at and above 0.84 V yields much more transpassive dissolution of Cr oxide to Cr^{6+} so that it could destroy the Fe oxide connectiveness (as shown in figure 2.8e, the time for the arrest of Fe^{3+} to Fe^{2+} decreases with applied potential). Figure 2.8f shows a distinct difference for alloy composition below 11 at.% and above 14 at.%.

2.4 Validation of percolation model – from 2D to 3D transition effects

In this section, the percolation model is applied in Fe-Cr binary alloys, focusing on the 2D-3D cross effects. The assumptions of the model are carefully examined by online ICP-MS and DFT calculations.

2.4.1 Assumption I – Electrochemical behavior of Cr clusters alloyed in Fe surface

The description of the chemical bond between a molecule and a surface is necessary to understand the surface reactions such as electrocatalysis and corrosion. Recently, the alloying effect on electrochemical behavior has attracted considerable attention, especially in electrocatalysis. First principle calculations, such as DFT calculations, have been proven to be a powerful tool for advancing our understanding of the fundamental physics with atomic-scale details and have been widely utilized to explore the adsorption of molecules on metal/alloy surface[78–80]. With the primary passivation as the background of examining the percolation model in passivation. The

electronic effects of alloying are discussed in terms of Fe dissolution and Cr passivation in this section.

The electronic effects of how alloying with Cr alters the dissolution potential of Fe has already been addressed by Marcus with the first principle calculation on the extraction energies of Fe/Cr from clusters of different topologies and alloy compositions[81,82]. As shown in figure 2.9, the energies difference of Fe atom extracted from the cluster embedded with single Fe (4.84 eV) and the one with 1st NN all surrounded by Fe atoms (5.14V) is even less than the in the extraction energy change from the terrace (4.9 eV) to step (4.43 eV). For alloys with Fe as the matrix, where the number of large Fe clusters prevails, the effect of alloying on dissolution energy is believed to be negligible.

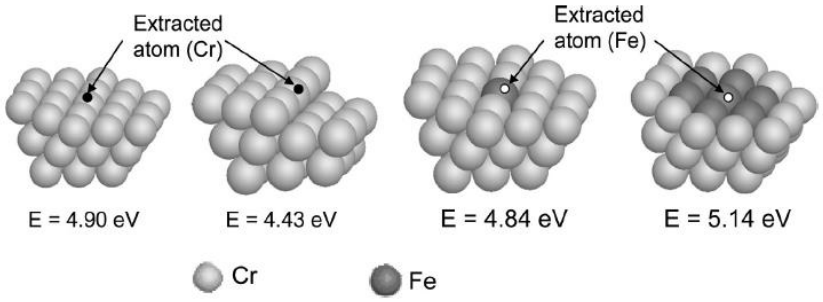

Figure 2.9. Extraction energy of Cr and Fe from clusters of various topologies and the chemical environment, using the modified embedded atom method (MEAM) potentials[81].

The d-band model developed by Nørskov associates the adsorption energies and the activation barriers with the d-band center of the transition metal, which has been widely used to predict the catalytic activity on transition metal surfaces. The higher energy relative to Fermi energy of d band states is, the stronger the bonds. They also rationalized the alloying effect with an essential trend of the alloying-induced shift in the

d-band centers of transition metals with a series of DFT calculations[78]. For example, alloying Pt with elements in the left sides of Pt in the periodic table (Fe, Co, Ni, Co, Y, Sc, etc.) shifts the d-band of Pt down and thus reduces the bonding energies of adsorbates like O_2. To our knowledge, there is no investigation directly addressing alloying effects on the adsorption/passivation of the Fe-Cr system. Simply applying this periodic table-based scheme to Fe-Cr alloys contradicts our observation that the addition of Cr increases the binding energy of the adsorbate to Fe or the Fe passivation. For a spin-polarized system like Fe-Cr, the magnetic interactions between Fe and Cr atoms could be critical, but not considered by Nørskov.

In addition to the corrosion applications of the Fe-Cr alloy system, the vital role of the alloys plays as structural parts in fusion reactors also drive a number of DFT calculations on the system, which by contrast, includes the magnetic interactions[83–85]. However, those spin-polarized calculations show that the increasing concentration of Cr, from 2 at.% to 10 at.%, lowers the d-band centers of both Cr and Fe[86], as shown in figure 2.10. Instead of entirely relying on the occupation of the d-band center, Seung-Cheol Lee emphasized a stabilization process through spin-dependent metal-adsorbate interactions for those surfaces with high spin polarization. It is found that the spin-polarized surface with a lower occupied d-band unnecessarily displays a weaker binding with the adsorbates[86]. As a result, evaluating adsorption affinity change during Fe-Cr alloying by only comparing the d-band center shift could be misleading. A direct comparison of adsorption energies is needed. Here, spin-polarized DFT calculations were

conducted to directly quantify how the adsorption energy of H_2O or O_2 on the Cr clusters surrounded by Fe atoms differentiates from elemental Cr.

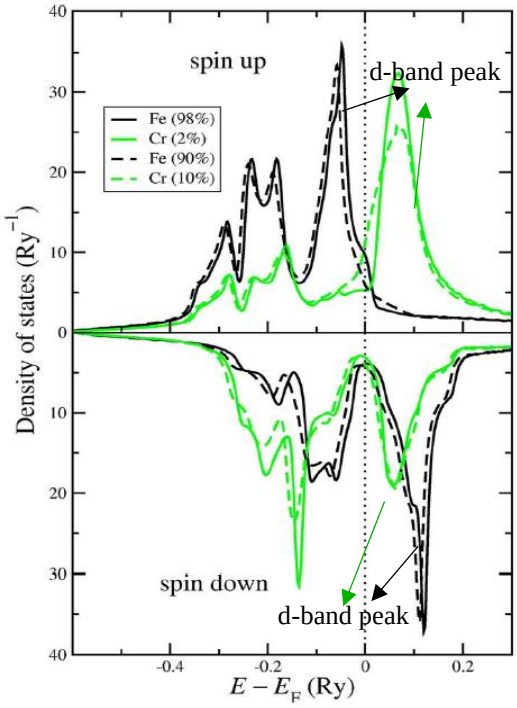

Figure 2.10. Projected density of states (p-DOS) of Cr (green) and Fe (black) in random bcc alloys Fe-2 at.% Cr (solid) and Fe-10 at.% Cr (dashed) with ferromagnetic configurations[86]. The d-band around the Fermi level is marked out.

Figure 2.11 shows the distribution of differently sized Cr clusters on (110) oriented alloys surfaces of three critical compositions given by MC simulations. The average sizes of 1.86, 2.48, 3.32 are obtained for 10 at. Cr%, 15 at. Cr% and 20 at. Cr%, separately. It is found that the surfaces with the alloy composition we investigated are dominated by small Cr clusters like monomer, dimer, and trimer, especially for the alloy with lower Cr composition. As a result, Cr clusters up to trimer could well represent the

alloys within the composition ranges we are interested in and are thus addressed in our calculations.

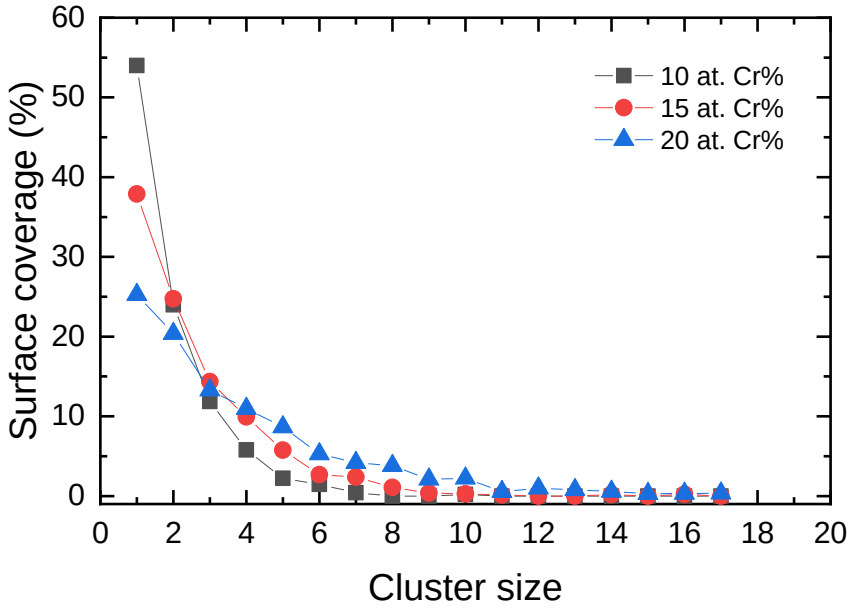

Figure 2.11. Cluster size distribution in case of random BCC Fe-Cr alloy (110) surfaces with different Cr compositions. The size of the Cr cluster is defined with neighboring Cr atoms up to 2nd NN. Results are obtained by averaging 3 realizations of filling a 128 x 128 BCC (110) surface in KMC simulations of random alloys. The simulations are conducted by Dorota M. Artymowicz.

It has been reported that the thermodynamic stability of the adsorbate-alloys system is primarily determined by the local environment contributed by the first layer of the surface with a minor contribution from the subsurface[87]. As a result, it is reasonable to simulate a Fe-Cr alloy by only doping the Cr atoms to the top layer of the Fe surface. Figure 2.12 addresses how the alloying process affects the dissociative adsorption of O_2 on Fe-Cr alloys through Fe surfaces doped with Cr clusters of various sizes and configurations, with top and bottom cartoons illustrating the initial and final configurations of the O_2 dissociation on (110) surfaces, separately. The adsorption energy E_{ad} is calculated by equation 2.2:

$$E_{ad} = \frac{1}{2}[E_{x/slab} - (E_{slab} + E_x)], \quad (2.2)$$

where $E_{x/slab}$ is the total energy of an adsorbed system; E_{slab} and E_x are the energies of the corresponding clean surface and adsorbent molecule reaching equilibrium in the vacuum.

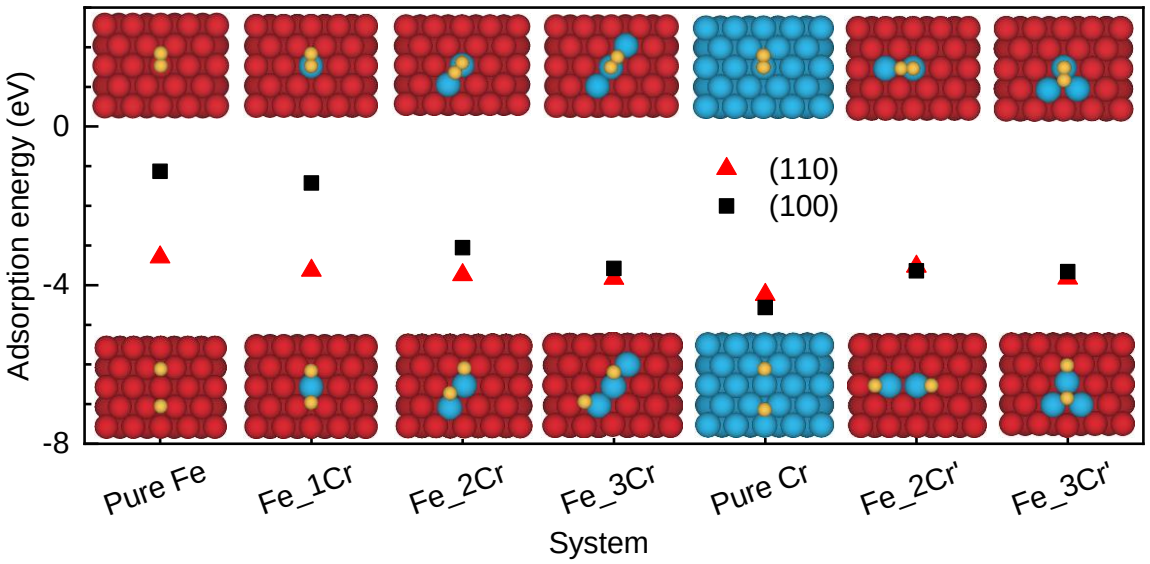

Figure 2.12. DFT calculations result of the dissociative adsorption of di-oxygen on Fe, Cr, and Cr doped Fe (100) surfaces (black square) and (110) surfaces (red triangle). The cartoons illustrate the (110) Fe surfaces doped by Cr monomer, dimer, and trimer before (top row) and after (bottom row) oxygen dissociation. The simulations were conducted by Duo Wang.

The O_2 molecule is dissociated with the O-O distance extended to more than 1.45 Å for all configurations after geometry optimizations. Pure Cr shows stronger bonding with O than elemental Fe does, especially in (100) oriented surface. A quick convergence to pure Cr with an increasing size of Cr can be recognized. Weighing the adsorption energy of Fe surface embedded with Cr trimer in between elemental Fe and Cr yields a percentage of 71% and 57%, with the absolute value reaching 91% and 78% of elemental Cr, for (110) and (100) orientation, respectively. The average adsorption energy for the

four configurations of Cr dimer and trimer is -3.49 eV/atom and -3.73 eV/atom. The difference in the energy, 0.24 eV/atom, corresponds to a difference in equilibrium potential of 240 mV, according to equation 2.3:

$$\Delta G = -nF\Delta E, \tag{2.3}$$

where n is the number of electrons transferred, and according to Uhlig's electron configuration theory, n equals 1; and F is the Faraday constant.

This difference matches nicely with the experimentally obtained -250 mV shifts of the first peak potential between 9.4 at.% alloy, of which the average cluster size is close to dimer, and 20.2 at.% alloy, of which the average cluster size is a little larger than trimer.

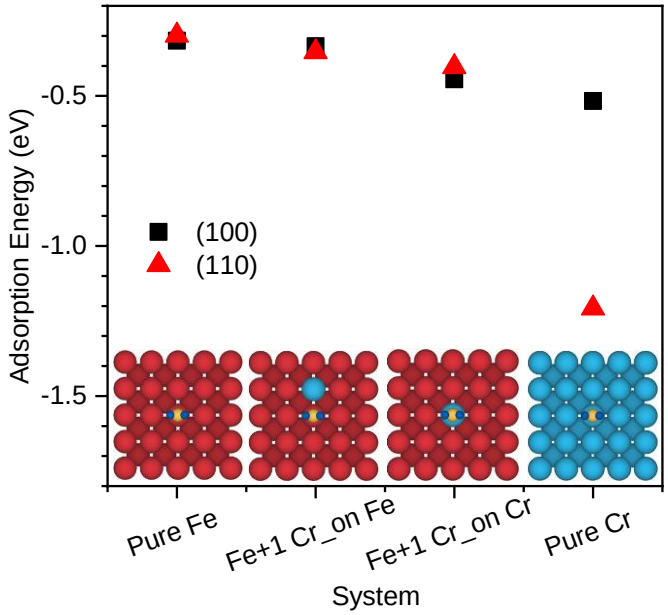

Figure 2.13. DFT calculations results of the adsorption of H_2O on Fe, Cr, and Cr monomer doped Fe (100) surfaces (black square) and (110) surfaces (red triangle). The cartoons illustrate the initial configurations in case of (100) surfaces. The simulations were conducted by Duo Wang.

By contrast, simulation with simple relaxations yields the H_2O molecule no more than slightly (less than 6% of both the bond length and the bond angle) distorted for all cases. It is reasoned the high barrier of water dissociation hinders the further reaction. The initial adsorption result is summarized in figure 2.13. Additional calculation on the bond-breaking barriers and the dissociation energies of the reaction, H_2O to H and OH, could be done with the employment of CI-NEB techniques.

To conclude, alloying with Cr will slightly shift the potential of Fe dissolution by around 100 mV. Cr clusters with small size such as trimer already display passivation behavior close to elemental Cr. As a result, it is safe to choose one potential for the alloys within the composition range interested, e.t. 9.4% - 24.3%, to display similar primary passive behavior that Fe is actively dissolved while Cr is passivated to form the film. Still, ICP-MS results are further analyzed to locate this potential for primary passivation in the following section.

2.4.2 Assumption II – Dissolution selectivity and undercutting of finite clusters

The kinetics of film growth and metal dissolution is essential for the interpretation of the passivity mechanisms. Most published kinetic studies are based on the measurement of electrochemical current, which adds up the current contributing to the development of the passive layers and the current associated with the electrochemical dissolution of metal. Take Cr for example: $n_{Cr(oxidized)} = n_{Cr^{3+}(in\ the\ film)} + n_{Cr^{3+}(in\ the\ solution)}$. Measuring Faradaic current alone does not distinguish the role of the oxidative films developed by the two constituent elements, nor does it tell us anything about selective dissolution. XPS is commonly employed to analyze the composition of the passive film and does shed some light on the dissolution selectivity when passivation

occurs. However, derivating the dissolution rate ratio of Fe/Cr from the composition of oxide film remains tenable only with the assumption that the total oxidation rate ratio is congruent with alloy composition, that is, Fe and Cr atoms being oxidized at the same rate. By contrast, online ICP-MS analyzes the electrolyte directly, revealing the fate of the ionized spices and supplementing the existing surface analysis that has been performed on passive films. Here, the ions caught from the solution are presumed to originate direct dissolution of the metal substrate without consideration of the negligible chemical dissolution that thins the film.

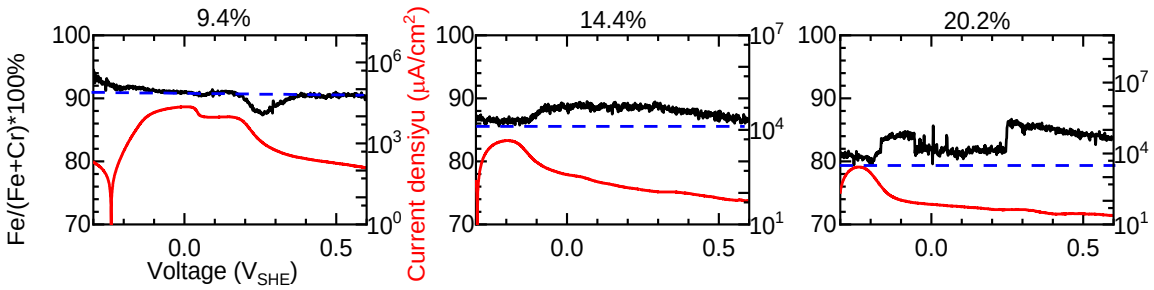

Figure 2.14. Selective dissolution of Fe (black) in Fe-Cr alloys as a function of applied potential measured by online ICP-MS and corresponding LSV (red) in 0.1M H_2SO_4. The scanning rate is 5 mV/s. The dashed blue lines mark the Fe at.% in the alloy. The epxeriments were conducted by Pietro P. Lopes.

Figure 2.14 shows the ICP-MS results during the anodic polarization for three compositions around the critical percolation thresholds of BCC lattice. For all three compositions, the selective dissolution of Fe in the active region starts from the corrosion potential and ends around the first peak. The DFT calculations in section 2.4.1 have shown that the adsorption energy of O_2 on different-sized Cr clusters in the Fe matrix: the larger size of the cluster, the closer value it has to pure Cr. The same trends should also be expected for the passivation potential of Cr cluster in the Fe matrix, which means with

increasing applied potential, the Cr clusters of larger size initiate passivation earlier than the smaller one. In the active dissolution region, those large Cr clusters participate in passive oxide formation. In contrast, the Cr clusters in a smaller size and Fe are dissolved or get undercut into the solution and detected by the quadrupole mass analyzer, yielding slightly higher Fe/Cr in the electrolyte than in the alloys. With the Cr cluster of smaller size starting to participate in passivation around peak potential, the Fe atoms that bridge these Cr clusters are trapped in the passive film. As a result, the dissolution proceeds with a ratio congruent to the alloy composition.

While the Cr atoms maintain passivation, the initiation of Fe dissolution causes the selectivity arising after the first peak, where the percolation model is interested. This increase in Fe/Cr ratio is much less evident in 9.4 at. % alloy, since no connected network of Cr is embedded in the alloy with Cr at.% below the percolation threshold, and the unconnected Cr clusters surrounding by Fe is easily undercut into the electrolyte when the bridging Fe atoms begin to be dissolved. Meanwhile, a reverse selectivity, that is, Cr shows selective dissolution, is also observed only in 9.4 at. % alloy. For alloys with low Cr composition (9.4 at. %), most parts of the surface still suffer massive dissolution with a high average current density even though Cr has already passivated, indicated by the current density of the second peak in order of 10 mA/cm^2. The initiation of Fe passivation will result in an apparent selective dissolution of Cr in a way like the initiation of Cr passivation dose in the active dissolution region: The initiation of Fe passivation only holds those larger Fe clusters on the surface. Those passivated Cr_2O_3 clusters are undercut with the dissolution of smaller Fe clusters. While in the active dissolution region, Fe atoms in the undercut particles are in a neutral state. ICP-MS will capture no

matter neutral state atoms or oxidized state ions. On the other hand, in alloys with higher Cr composition (14.4 at.% and 20.2 at.%), the passivation of Fe makes little difference since a connective network of Cr oxide has already been established.

Within the primary passivation region, oxidized Cr atoms keep looking for linkage with nearby Cr atoms by bonding with absorbed H_2O and form corresponding Cr (hydr-)oxides gel on the alloy surface. At the same time, Fe is actively dissolved, destroying the connectedness of the passive film. Protective films are developed until the percolation is accomplished after the alloy is dissolved in with a depth of h. The alloy portion enclosed by Cr oxide but out of percolated network becomes detached once Fe in between is dissolved and the Cr on the surface is passivated, which is introduced as the undercutting process in section 1.5.1. The undercut particles are not detected by the faradaic current but ionized by inductively coupled plasma and caught by spectroscopy detector, engendering a decrease of current efficiency. Figure 2.15 displays the discrepancy between electrochemical current density and the one converted from mass density dissolution. The dissolution rates(v) are converted to effective current density (i) via equation 2.4:

$$i = \left(\frac{v_{Fe/Ni}*2}{M_{Fe/Ni}} + \frac{v_{Cr}*3}{M_{Cr}}\right) * \mathrm{F}, \qquad (2.4)$$

where M's are molecule weights, F is Faradaic constant. According to the results shown in figure 2.15, with increasing Cr concentration and thus Cr connectivity, the current inefficiency caused by detachment of Cr-covered clusters decreases.

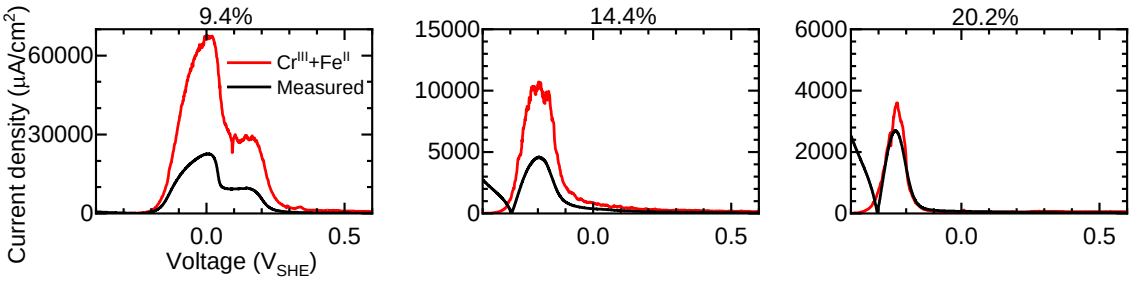

Figure 2.15. The current density for ionization and dissolution into solution during passivation of Fe-Cr alloys. Current density is converted from the mass density dissolution rate measured by online ICP-MS, Cr is assumed to be dissolved in forms of Cr^{3+} and Fe in forms of Fe^{2+} (black) and corresponding LSV (red) in 0.1M H_2SO_4. The scanning rate is 5 mV/s. The epxeriments were conducted by Pietro P. Lopes.

To conclude, the potential range for primary passivation, which is defined as Fe being actively dissolved while Cr forming a passive film, is identified to follow the first peak in LSV and ends when Fe begins to passivate at the second peak, as we predict in section 1.5.1. For alloys with LSV curves singly peaked, the start of Fe passivation is hard to locate with just LSV. When extending the slightly negative shift of the second peak in alloys with low Cr compositions into the high Cr contained alloys, locating the potential at 0 mV is safe to create primary passivation for all the alloy composition investigated. The dissolution selectivity measured by ICP-MS further confirms this. Meanwhile, the percolation model partly explains the inconsistency between mass density dissolution and electrochemical current density through the undercutting process.

2.4.3 2D to 3D transition in passivation behaviors – I. Experiments

In the Fe-Cr alloy system, the maximum possible distance for two Cr atoms forming -Cr-O-Cr- bond is about 4.03 Å, based on the hard-sphere ionic radii (radius of Cr^{3+} and O^{2-} are 0.615 Å and 1.40 Å, respectively). For BCC Fe-Cr (lattice parameter a=2.856 Å), the distance between 1st, 2nd, and 3rd nearest neighbors (NN) is $\frac{\sqrt{3}}{2}a$ (2.47 Å), a (2.86 Å), and $\sqrt{2}a$ (4.04 Å), respectively. An angled -Cr-O-Cr- bond will allow two connected Cr atoms to locate with a distance between 2nd NN to 3rd NN. The p_c in BCC lattice for interactions including up to 2nd NN (p_c {1,2}) and 3rd NN (p_c {1,2,3}), determined from the percolation model, is 17.5 % and 9.5%[88]. The Cr percolation is expected to be achieved with a Cr at.%, p_c, sitting between these two values. However, the alloys with Cr concentration of p_c will achieve passivation after thousands of monolayers are dissolved from the surface. As the Cr content in the alloys continues to increase, the number of required dissolved layer is predicted to decrease in a way as percolation does from 3D to 2D. The alloy passivation transition is less steep than simple 2D/3D percolation due to the 2D to 3D transition.

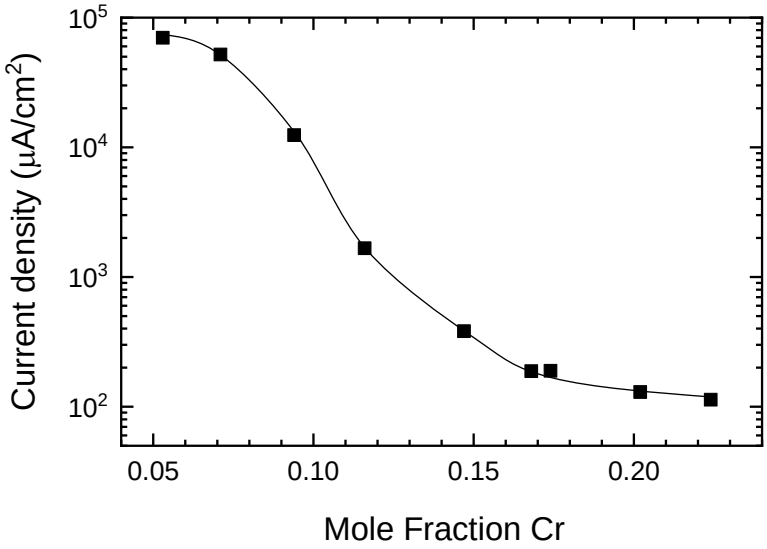

Figure 2.16. Transition behavior of current density over Cr concentration at an applied voltage of 0 V. The current density of different Fe-Cr alloys is collected from figure 2.2a.

With the assumptions confirmed in the previous two sections, the charge density and dissolves monolayer (h) for passivation of the alloys with sets of Cr compositions are determined with potential steps experiments to examine the predictions of the percolation model. The potential chosen for primary passivation sits following the first peak, e.t. 0 V. Figure 2.16 collects the transition behavior of the current density at 0 V over Cr concentration from the passivation profiles in figure 2.2a. A sharp decrease in current density locates in around 10 at.% Cr, a value agrees with the analysis by the percolation model. The current density was recorded and numerically integrated to the charge density. The number of monolayers, h, for passivation is formulated on the primary (110) BCC surface through equation 2.5 by assuming the oxidation states of the reaction products as Cr^{3+} and Fe^{2+} separately,

$$number\ of\ layers\ dissolved = \frac{\int_0^t I\,dt}{A} \Big/ \frac{2*(3*C+2*(1-C))*q}{\sqrt{2}*a_{Fe}^2}, \qquad (2.5)$$

where A is exposed surface area, *I* is the magnitude of measured current, C is the mole fraction of Cr, q is the elementary charge, and a_{Fe} is the lattice parameter of BCC Fe. The variation of lattice parameter with Cr at. % is negligible and not considered here.

For comparison, a potential above the second passivation peak of 9 at.% alloy, 0.44 V, is also studied to address the effects of the applied potential. It is believed that this potential has both Cr and Fe participate in the formation of protective oxide films. Figure 2.17 shows the two sets of integrated chronoamperometry results with numerical fits to the theoretical equation, $h = c[p_c(h) - p_c^{3D}]^{-\nu_{3D}}$. The calculated dissolved depth is in order of tens of monolayers, which corresponds to passive films of several nanometers measured by XPS analysis. The obtained values of p_c^{3D} under two potentials (0.04 V and 0.44 V) are 0.107 ± 0.0005 and 0.037 ± 0.007 respectively. The p_c^{3D} under 0

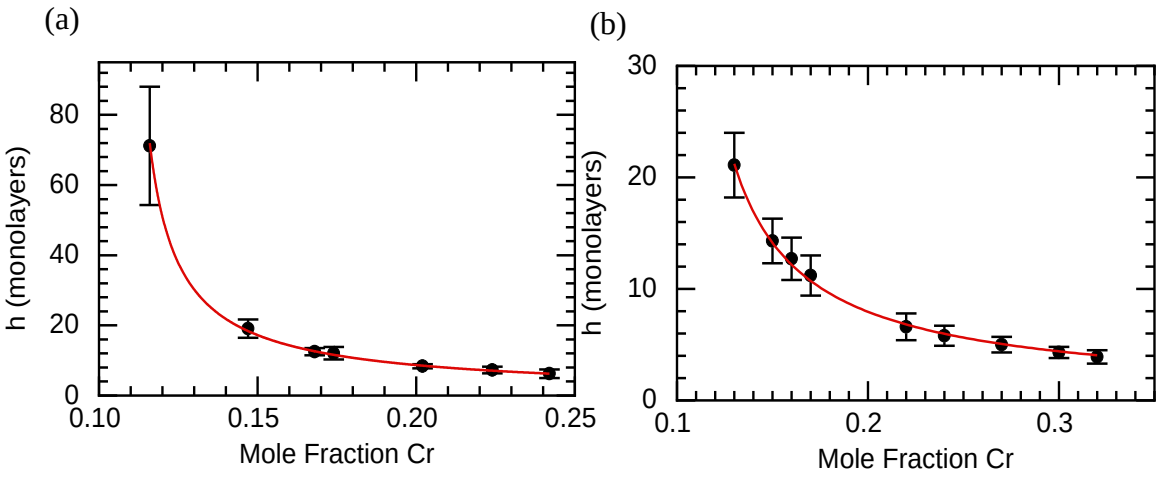

Figure 2.17. The equation for the 2D-3D cross-over effect is fitted with the passivation behavior of Fe-Cr alloys under two different passivation potentials. The number of dissolved layers is plotted with bulk Cr composition. The Fe-Cr alloys are passivated under the potential of (a) 0.04 V for 100 s and (b) 0.44 V for 400 s. The red curves correspond to the fitting results with the equation of $p_c(h) = p_c + c\,h^{-1/\nu}$ with v=0.878 used for the 3D lattice.

V, 0.107, shows excellent agreement with our prediction: between the theoretical value of $p_c^{3D}\{1,2,3\}$= 0.095 and $p_c^{3D}\{1,2\}$= 0.175 in BCC lattice and well matches the critical value at 0 V in figure 2.16. On the other hand, the smaller p_c^{3D} obtained under the higher potential, 0.44 V, supports our hypothesis of cooperative passivation joint by both Fe and Cr.

2.4.4 2D to 3D transition in passivation behaviors – II. Simulations

In the KMC simulations of Fe-Cr primary passivation behavior, the maximum penetration depth of dissolution by the potential scanning (1 mV/s from 0.1 V to 0.7 V), which is labeled as h' in order to differentiate from the h calculated from Faradic charge density, was collected over a range of compositions interested and fitted to the theoretical equation, $h = c\,[p_c(h) - p_c^{3D}]^{-\nu_{3D}}$. As shown in figure 2.18, the decent fitting of the 2D

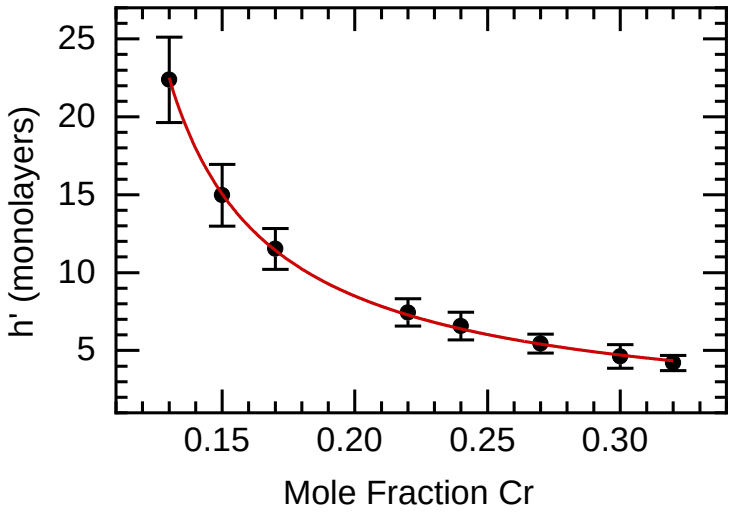

Figure 2.18. Numerical fits of the theoretical equation, $h = c\,[p_c(h) - p_c^{3D}\{1,2,3\}]^{-\nu_{3D}}$, with potential step (0.1 – 0.7 V) integrated chronoamperometry results during KMC simulations of Fe-Cr passivation behavior. The obtained $p_c^{3D}\{1,2,3\}$ equals to 0.096 ± 0.001, c is in order of unit with value of 1.17 ± 0.02. KMC simulations were conducted by Dorota M. Artymowicz.

to 3D transition with the simulation data yields a value of p_c^{3D} of 0.095 ± 0.001, a value a bit lower than the experimentally fitted one, 0.107.

With the surface roughened by dissolution, the h obtained based on the electrochemical experiments is a globally average value. In contrast, the accurately collected penetration depth in the KMC simulations, h', represents a local maximum penetration depth of dissolution. We also calculated the average dissolution depth, h, based on the charge density collected in KMC simulations in the same way we did for the experimental results. The relationship between the h and h' is shown in figure 2.19a. A linear relation over the composition examined is found. A similar linear relationship is suggested in the experiments. The (h, h') pairs slightly deviate from the linear line at the high Cr composition end, where the mole fraction of Cr approaches p_c^{2D}. The h originates from the charge density, including both the part associating with metal dissolutions and film formation. When the Cr concentration in the alloys is low, most of the charge

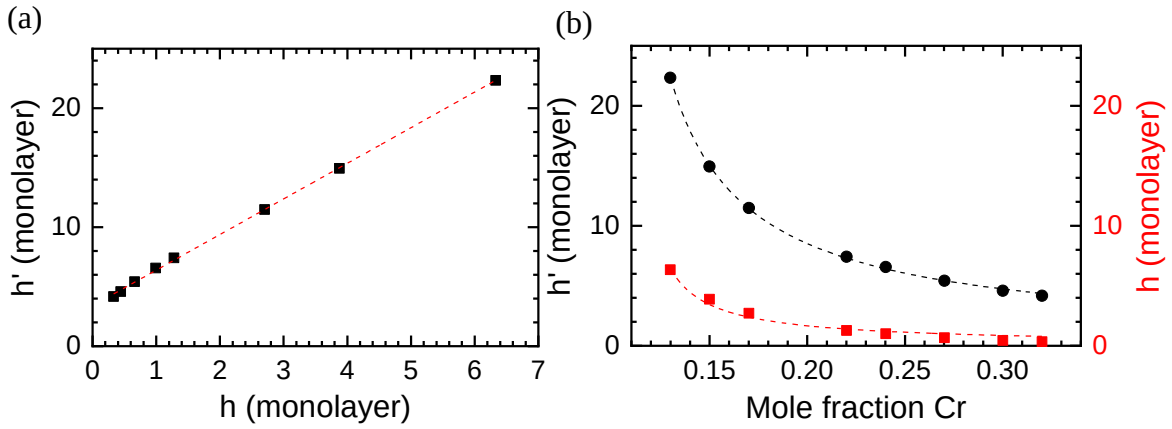

Figure 2.19. The impact of replacing the penetration depth, h', with average depth based on charge density, h, in KMC simulations. (a) A linear behavior between h' and h is shown. The linear fitting(dash) line is h=3* h'+3.4. (b) Comparison of the fits to the theoretical equation for h: $h = 0.20\ [p_c(h) - 0.110]^{-0.878}$ (red) and h': $h' = 1.10\ [p_c(h) - 0.095]^{-0.878}$ (black) . KMC simulations were conducted by Dorota M. Artymowicz.

density is consumed by dissolution, creating a locally deep penetration path. As the Cr concentration increase, the more globally flat surface narrows the difference between h and h'. Figure 2.19b summarizes the error of estimating h' with h on the 2D-3D cross effect fittings, the change of both h and h' over Cr concentration fit the theoretical equation well, with the p_c^{3D} obtained by h' a little bit lower. The minor difference in the fitted value suggests a high efficiency of the electrochemical measurement.

Marcus has also simulated the evolutions of Fe-Cr alloys surfaces during passivation as a function of Cr at.%[89]. The rules he used to define Fe and Cr dissolution probability are fixed. We can say the simulations are conducted under a "fixed" applied potential. Notably, his simulations took the surface diffusion of Fe and Cr into consideration, which is neglected by our simulations. Figure 2.20 shows the decent

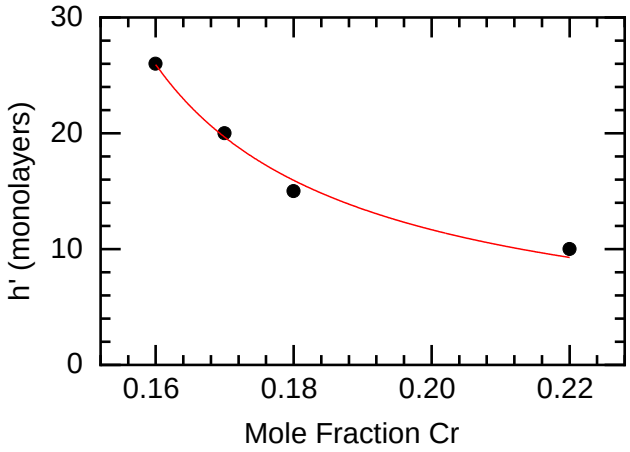

Figure 2.20. Marcus KMC results[89] with consideration of surface diffusion fitted to the theoretical equation: $h' = 1.09\ [p_c(h) - 0.13]^{-0.878}$. The simulations are conducted with cells of size 80 x 80 x 60 $Å^3$ (33600 atoms). The number of diffusion steps is set as 1, the diffusion probability of Fe and Cr set as 0.4 and 0.65. The dissolution probabilities of Fe and Cr depends on the chemical environment: with 1 Cr atom neighbor, Cr is dissolved at possibility is fixed at 0.3, while Fe has 0.9. The increasing number of Cr in the neighbor brings down the dissolution probability of both Fe and Cr.

fit of his results to our theoretical equation. Though with a higher fitted p_c^{3D}, a decent fitting is observed.

2.5 Validation of percolation model – from atomic configuration effects

In the regular solution model, the enthalpy of mixing is calculated through equation 2.6 and equation 2.7,

$$\Delta H_{mix} = Z\Delta E X_{Cr} X_{Fe}, \tag{2.6}$$

$$\Delta E = [E_{Fe-Cr} - 1/2(E_{Fe-Fe} + E_{Cr-Cr})], \tag{2.7}$$

where Z is the number of nearest neighbors; ΔE defines the interaction parameter of the lattice; *X's* correspond to the atomic fraction of the constituting elements. The difference in atomic interactions between Fe-Fe, Cr-Cr and Fe-Cr could compete with the entropy and lead to some degree of non-randomness.

Recently, some first-principles based calculations[90–96] shows that an inversion in the sign of ΔH_{mix} occurs at around 11 at.% Cr. Below this value, a single BCC phase is stable and with negative mixing enthalpy, the system tend to ordering at an intermediate temperature where entropy loses its competitiveness. By contrast, a clustering trend in alloys with higher Cr concentration separates the system into Fe rich and Cr rich, α + α' BCC phases. This inversion in ΔH_{mix} is reasoned to be originated from the magnetic frustration that Fe shows ferromagnetic (FM) property while Cr is antiferromagnetic (AFM). In Fe-Cr alloys, the magnetic moments of Cr monomers will be AFM aligned with surrounding Fe atoms; while for Cr clusters with a size of two Cr atoms (dimers) and three Cr atoms (trimers) or larger size, AFM alignment between Cr atoms will always make some Cr atoms FM with neighboring Fe atoms and thus increases the energy. The energy increased by magnetic frustration will be lowered when

the Cr atoms aggregate or cluster together. As a result, Cr atoms tend to separate with each other when Cr is dilute in the Fe matrix, while clustering is preferred at high Cr concentration.

This prediction by DFT calculations turns out to be experimentally supported by the inversion of the Warren Cowley short range order (WC SRO) parameter as a function of Cr concentration, measured by neutron scattering[97] and Mössbauer spectroscopy[98–100]. The WC SRO parameter is defined as α in equation 2.8. Since the spatial separation between Cr atoms on a surface depends on both Cr concentration and the atomic-scale ordering, in the context of the percolation model, SRO will undoubtedly alter the passivation behavior of Fe-Cr alloys. The impact of atomic-scale ordering is discussed in the following sections.

2.5.1 Disturbance of atomic distribution – I. Simulations

The percolation threshold of a clustered or ordered BCC lattice is studied by large cell Monte Carlo renormalization group method. Lattice simulating a non-random alloy is constructed by changing the probability of a Fe atom have Cr atoms as NN, p_{CrFe}, which is equal to p in a random Cr_pFe_{1-p} alloy. This deviation is described by a clustering parameter, $\alpha = 1 - (\frac{p_{CrFe}}{p})$, which is a function of the lattice interaction parameter, ΔE, according to equation 2.8:

$$\frac{(1-\alpha)^2}{(\frac{p}{1-p}+\alpha)(\frac{1-p}{p}+\alpha)} = \exp\left(-\frac{z\Delta E}{k_B T}\right), \tag{2.8}$$

where z is the coordination number of the lattice, k_B is Boltzmann's constant, and T is the absolute temperature.

The relation between α and p_{ij} is then given by equation 2.9 - 2.12 as follows:

$$p_{CrFe} = p\,(1-\alpha), \tag{2.9}$$

$$p_{FeCr} = (1-p)\,(1-\alpha), \tag{2.10}$$

$$p_{CrCr} = 1 - p_{FeCr}, \tag{2.11}$$

$$p_{FeFe} = 1 - p_{CrFe}. \tag{2.12}$$

Each lattice realization starts with filling up the sites in an empty cell with a size of $b * b * b$ with Fe or Cr atoms in a random order, based on the normalized probability that depends on the identity and number of the NN sites. The normalization principle is illustrated with three selected scenarios in the 2D lattice in figure 2.21.

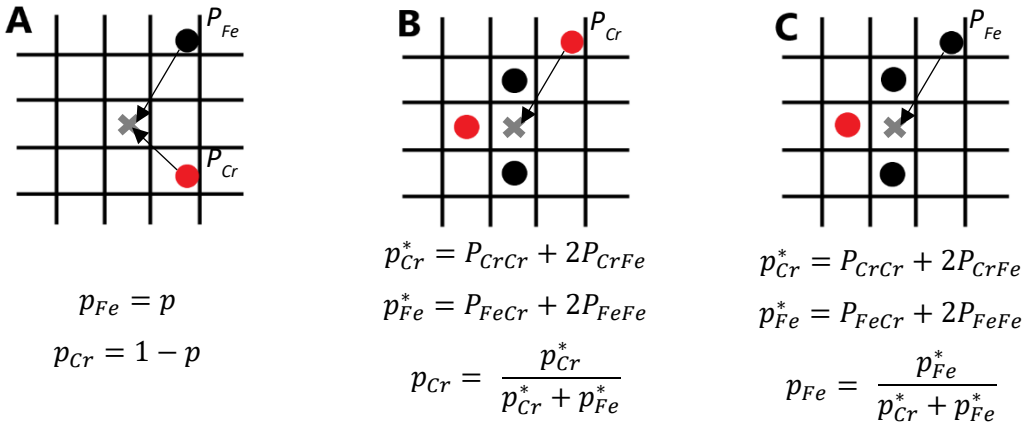

Figure 2.21. Filling a 2D lattice with non-random Fe-Cr alloys with different occupancy of neighboring lattice: (a) the filling probability remains alloy composition when there are no occupied neighbor sites. (b) and (c) show the normalized filling probability of atom Cr and Fe, respectively, when 3 occupied sites are in the neighbor. Black circles represent Fe atoms; red circles represent Cr atoms.

Large scale Monte Carlo renormalization group technique[101,102] is employed to obtain percolation thresholds for each given ΔE. The cell is gradually filled up by Fe and Cr atoms with the probability calculated with the principles shown in figure 2.21, the existence of a percolating Cr cluster is checked after each filling step; if not, the

concentration of Cr, p, is increased until Cr percolates the lattice and the corresponding concentration is then recorded as percolated concentration for this realization.

Figure 2.22 shows how the site percolation threshold is obtained for the lattice not randomly occupied, with an example of lattice clusters under ΔE = +0.015 eV and T = 300 K. After running thousands of realizations, the distribution for the numbers of realization over the percolated concentration could be collected. The histograms are shown in figure 2.22a. The distribution is fitted with Gaussian probability density function, then integrated and normalized to the corresponding cumulative density function. The corresponding function curves of different simulation cell sizes are shown in figure 2.22b and figure 2.22c, respectively. The percolation threshold of specific sized cells, $p_c(b)$, is collected as the interaction of the cumulative density function with the line $p = p'$. The scaling exponent, ν_p, is determined by equation 2.13,

$$\nu_p = \frac{lnb}{ln\lambda_p}, \tag{2.13}$$

where λ_p, is evaluated by the slope of the curve at the intersections in figure 2.22d. As shown in figure 2.22e, $p_c(b)$ is plotted as a function of b^{-1/ν_p}, the intercept of the fitted linear line with y-axis gives the $p_c(b = \infty)$.

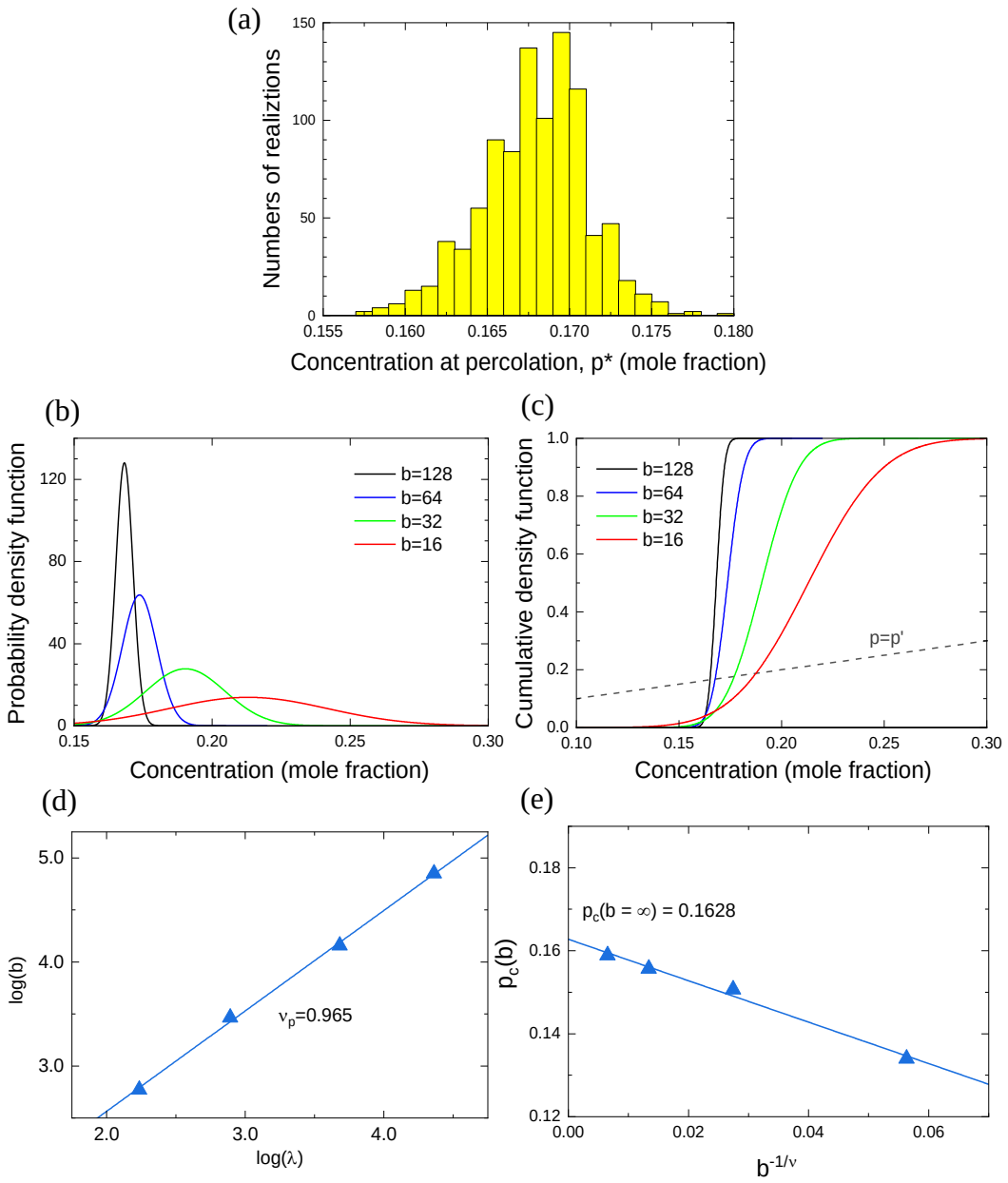

Figure 2.22. Percolation thresholds up to 1st NN, pc{1}, obtained through large cell Monte Carlo renormalization methods, with enthalpy set for alloys with clustered configuration: ΔE = +0.015 eV and T = 300 K. (a) Histograms showing the distribution of numbers of realizations ending up with different percolation thresholds, p*. 967 realizations on lattice of b = 128 are collected in total (b) Probability density functions with different simulation cell size are obtained by fitting the corresponding histograms (c) Cumulative density function of corresponding curves from (b), the intersection of these curves with the line p'=p yields the fixed-point value p*(b), the slope of the curve at the interaction is collected as λ_p. (d) the scaling exponent ν_p, is obtained, 0.965, from the slope of linear fitting with $(lnb, ln\lambda_p)$ pairs from (c). (e) pc for infinite cell, 0.1628, is obtained by extrapolating the linear fitting line of $(p_c(b), b^{-1/\nu_p})$ from (c). MC-RNG analysis were conducted by Dorota M. Artymowicz.

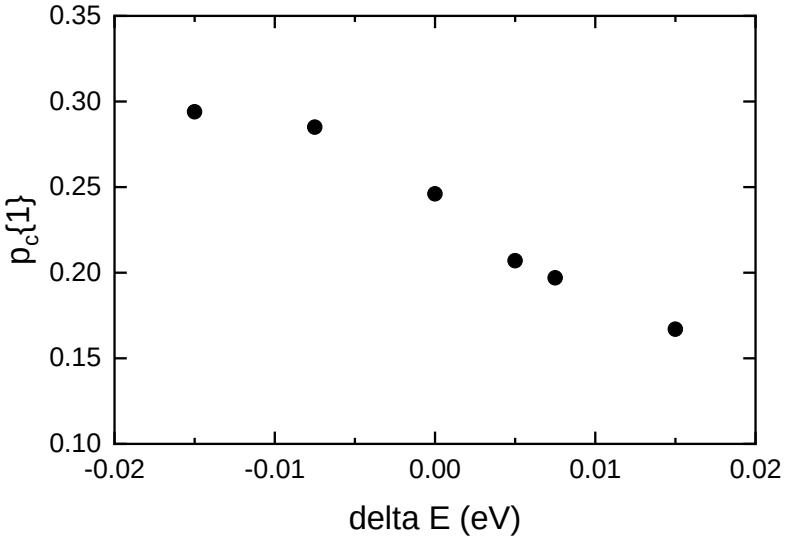

Figure 2.23. $P_c\{1\}$ as a function of ΔE is obtained by large cell MC RNG methods, ΔE ranges from -0.015 eV to +0.015 eV, T=300 K. MC-RNG analysis were conducted by Dorota M. Artymowicz.

Figure 2.23 evaluates how the 1st NN site percolation threshold, $p_c\{1\}$, changes with ΔE in range of [- 0.015 eV, 0.015 eV] at 300 K. It is found that atomic ordering dramatically changes $p_c\{1\}$, changing from 24.6% (in case of SRO with ΔE = -0.015 eV) to 17.5% (in case of clustering with ΔE = -0.015 eV). In contrast, no significant effect of SRO or clustering is found on $p_c\{1,2,3\}$: the deviation of $p_c\{1,2,3\}$ with ΔE of ± 0.015 eV from the random alloy is within ± 0.2%.

KMC simulations have also been conducted to the non-random alloys with lattice filled up via the principle talked above, ΔE = -0.016 eV is set to simulate SRO alloy; and ΔE = -0.016 eV is used for the case of clustered alloy. The obtained penetration depth, h', is plotted as a function of Cr concentration and fitted to the theoretical equation, and the results are displayed in figure 2.24a. No significant difference in fitted p_c^{3D} is found

between all the alloys tested. Clustered alloys show slightly improved passivation behavior with the critical threshold lowered by about 2 at.% Cr, while slightly delayed passivation is predicted for SRO alloy. WC SRO is used to define the chemical ordering of the alloy, as described by equation 2.8. As shown in figure 2.24b, the plotted dissolved ML required for passivation reveals the impact of atomic configuration on the passivity when the alloy is fixed with composition. At this composition, $\alpha_1 > 0.060$ is required for passivation.

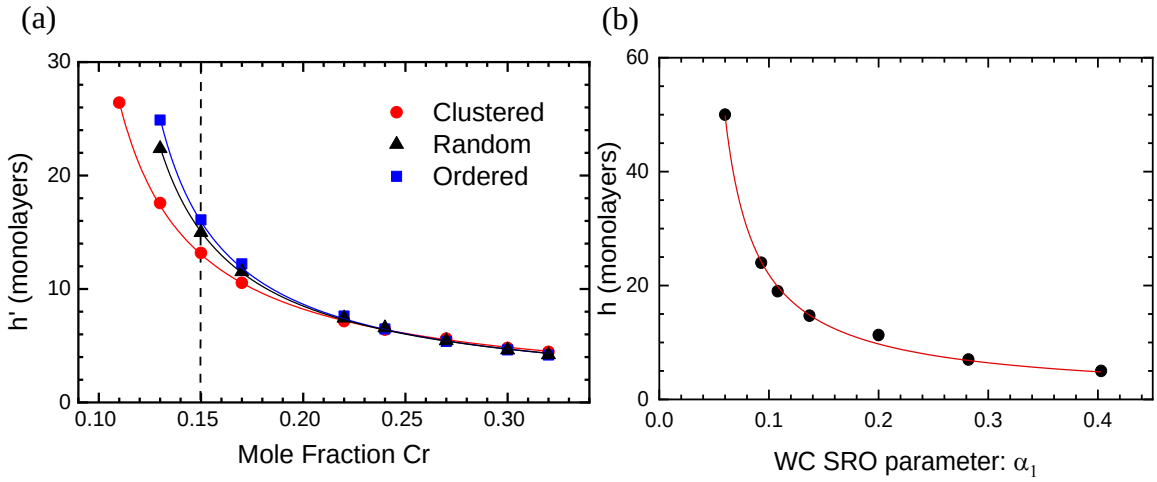

Figure 2.24. (a) The effects of atomic configurations on the 2D to 3D transition, $h' = c\,[p_c(h) - p_c^{3D}]^{-\nu_{3D}}$,with potential step (0.1 – 0.7 V) integrated results from KMC simulations. Clustered alloys (red circles): ΔE = 0.016 eV, $h' = 1.31[p_c(h) - 0.078]^{-0.878}$; random alloy (black triangles): ΔE = 0 eV, $h' = 1.10[p_c(h) - 0.095]^{-0.878}$; ordered alloy (blue squares): ΔE = - 0.016 eV, $h' = 1.17[p_c(h) - 0.099]^{-0.878}$. (b) The effect of SRO on the passivation of Fe-15 at.% Cr alloy (dashed line in (a)). The WC SRO parameter is plotted as the x-axis through its relationship with the 3D percolation threshold, $p_c^{3D}\{1\} = f(\alpha_1)$, as shown in equation 2.8, $p_c(h')$ is fixed with 0.15 (15% Cr in the alloy), h', the required dissolved monolayer for passivation, is plot in the y-axis, $h'(\alpha_1) = c\,[p_c - p_c^{3D}\{1\}(\alpha_1)]^{-\nu_{3D}}$. The dashed line is a guide to the eye. KMC simulations were conducted by Dorota M. Artymowicz.

2.5.2 Disturbance of atomic distribution – II. Experiments

The predictions by the MC renormalization and KMC simulations are compared with experimentally observed passivation behaviors of alloys in SRO and RSS. The SRO samples are obtained, following the protocols used in neutron diffraction and Mössbauer spectroscopy studies[98–100]. The heat treatment of all the samples prepared starts with homogenization at 1100 ℃ for 24 h and 800 ℃ for 24 h. Following that, a set of the samples stay at 520 ℃ for 24 h (FeCr 17.4 at.%) and 430 ℃ for 96 h (FeCr 9.1 at.%, FeCr 11.6 at.%, FeCr 14.4 at.%), reaching an equilibrium SRO state before a water quench. Annealing at intermediate temperature allows the redistribution of Cr atoms and the establishment of the SRO. The other samples are prepared to RSS counterpart by water quench followed by homogenization at 800C, where Fe and Cr atoms are randomly mixed.

Figure 2.25 shows the comparison of LSV results between the SRO and RSS alloys. The difference shows evident dependence on the alloy composition. As discussed in the previous section, the second peak corresponds to the passivation of Fe atoms, the peak height of which reflects the “protectiveness” of accomplished Cr passivation. Among the four compositions examined, the SRO Fe-11.6 at.% Cr alloy shows the most considerable difference in second passivation peak from the RSS counterpart. The passivation potential is increased by 50 mV, and the critical current is doubled. We believe a 3D percolated Cr cluster in RSS forms around this value, while SRO alloys with increased average Cr separation can hardly establish a percolated network around the same composition.

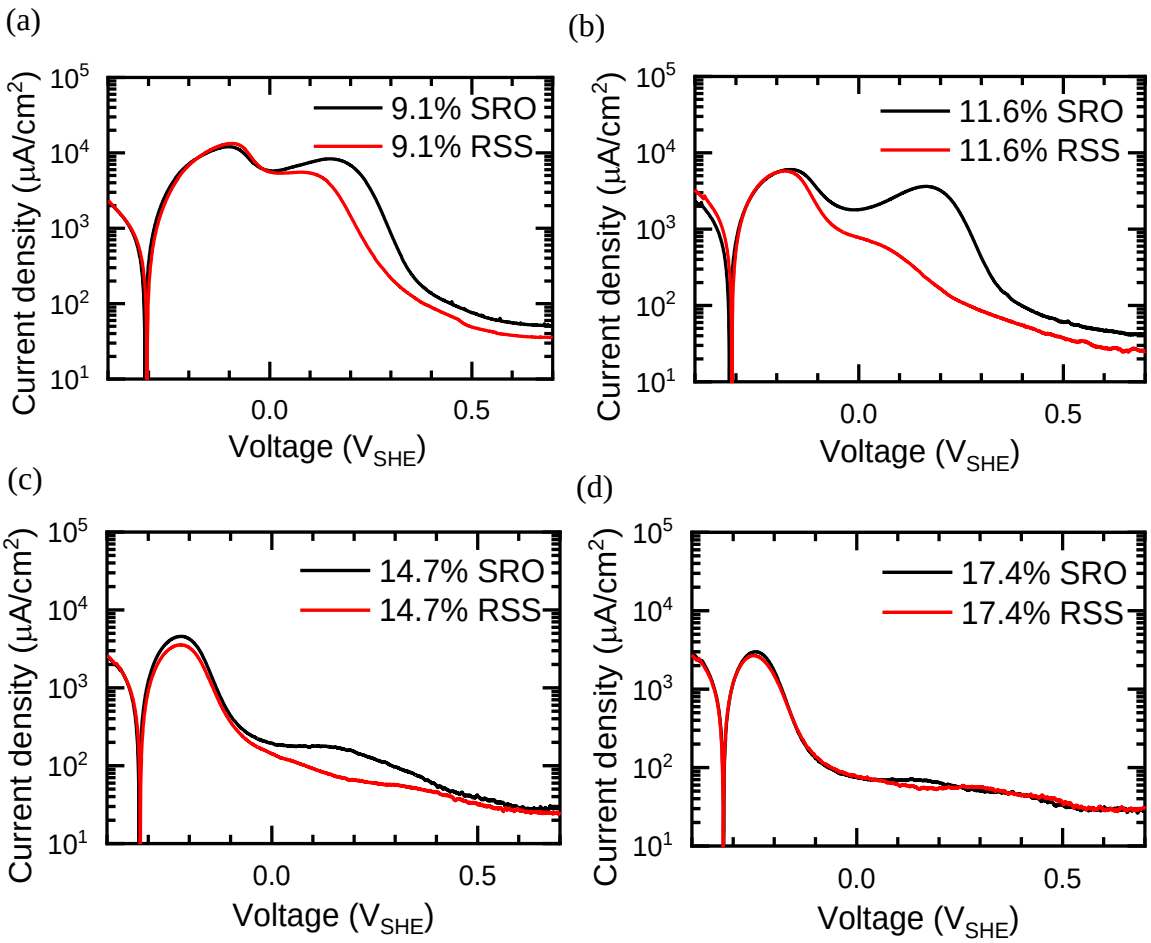

Figure 2.25. Comparison of LSV behaviors of SRO and RSS alloys with Cr compositions of (a) 9.1 at.%; (b) 11.6 at.%; (c) 14.7 at.%; (d) 17.4 at.%. The experiments are conducted in 0.1 M H_2SO_4 with a scanning rate of 5 mV/s.

SRO Fe-11.6 at.% Cr alloy also shows more "Fe-like" passivation (two large passivation peaks) even than SRO and RSS Fe-9.1 at.% Cr alloy. The occurrence of the second passivation peak has been attributed to the additional passivation from Fe, which inversely reflects the effectiveness of the Cr passivation and the percolation status. The Cr passivation of RSS Fe-11.6 at.% Cr alloy can bring the current down efficiently, leaving the second peak's critical current only a tenth of the first peak. A similar effect is seen in SRO Fe-14.4 at.% Cr alloy, implying a composition delay of around 2 at. % delay when comparing SRO alloys with RSS counterpart.

Another observation is that compared with RSS, the SRO alloys all display slightly higher passivation currents, suggesting less "protective" passive films. Without considering surface diffusion, the passive films will partly inherit the atomic distribution from the parent alloys when Fe is selectively dissolved in the primary passivation. As a result, films evolve on SRO alloys, of which the average distance between Cr NN atoms is larger than the one of RSS alloys, possess more aggregated Fe oxide clusters, and thus more vulnerable to the aggressive environment.

A delayed critical composition of the passivation of SRO alloys is further supported by comparing the numerical fits of different atomic configurations, as shown in figure 2.26. The electrodes were passivated at potential, 0.44 V, higher than the primary passivation potential so that all the alloys of interested composition could reach passivation states. With theoretically equal contributions from Fe passivation at the same passivation potential, the fitted p_c^{3D} for SRO alloys is higher than the RSS alloys, indicating a less connective Cr network of SRO alloys.

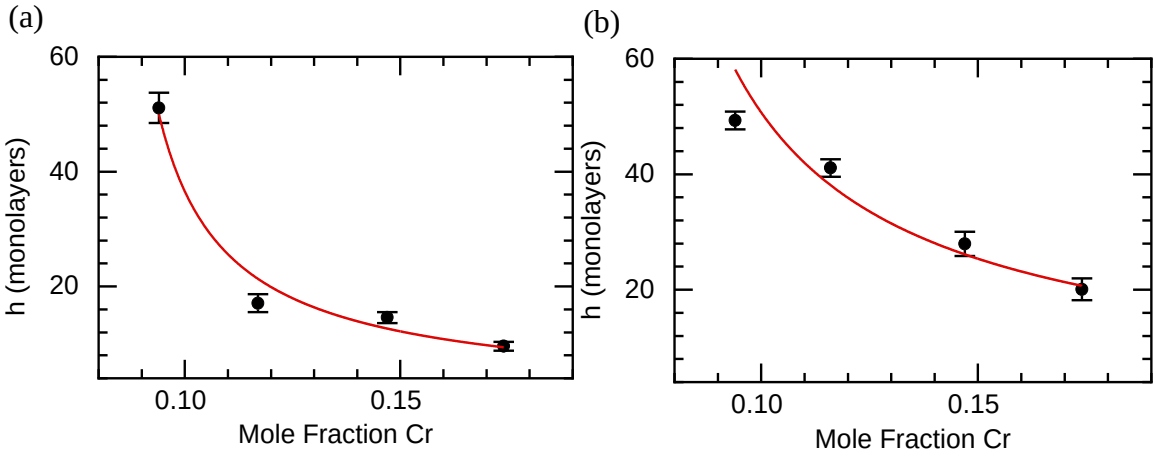

Figure 2.26. Numerical fits of the theoretical equation, $h = c\,[p_c(h) - p_c^{3D}]^{-\nu_{3D}}$ with passivation at 0.44 V for 400 s. The obtained p_c^{3D} of (a) SRO alloy equals to 0.08 ± 0.003, the one of (b) RSS is 0.058 ± 0.011.

To sum up, by disturbing the atomic configurations, the effect of atomic configuration on passivation behavior with LSV results is experimentally addressed in this section. As predicted by KMC simulations, the SRO Fe-Cr alloys show delayed passivation behaviors compared with RSS counterparts, especially at low Cr concentration. The ordering parameters of those Fe-Cr alloy we prepared may deviate from those reported in the literature. Still, these results reveal the significant impact of the NN population on the initial formation of -Cr-O-Cr- networks and thus the passivation behaviors and therefore support the percolation model. A quantitative comparison of the atomic effects between experimental results and simulation results can only be convincing when the ordering parameters are directly measured with scattering techniques or EXAFS.

2.6 Oscillations observed in Fe-Cr alloys with high Cr compositions

Oscillations under both potentiostatic and galvanostatic conditions during the electro-dissolution of metals have been known for a long time. With investigations characterizing oscillation by in-situ optical observations[103], ex-situ SEM micrographs[104], and magnified capillary current[105], the commonly accepted mechanism ascribes the occurrence of potential/current oscillations to the electrode surface swinging between active and passive states. The cycling is achieved through a feedback mechanism driven by the competition between two kinetic processes: dissolution and diffusion.

One of the earliest discovered and most widely studied oscillatory systems is the electro-dissolution of Fe in H_2SO_4. Podesta[104,106] suggested that when exposing a clean Fe surface to strong acid, oscillation cycles begin with a high-rate active dissolution

far surpassing diffusion rate limits. The accumulation of corrosion products, Fe^{2+}, drives H^+ of higher mobility away from the interface to minimize charge polarization. As a result, the local pH increases, promoting the precipitation of protective $Fe(OH)_2$ films and reversely hindering dissolution. The dispersion of Fe^{2+} in the electrolyte over time promotes the back diffusion of H^+ and, thus, dissolution of the protective film. Once the film is dissolved, the cycle repeats. For system concentrated with sulfate, porous salt films, $FeSO_4$, precipitate and passivate the surface, instead of $Fe(OH)_2$. The oscillations that have been reported are usually mono-periodic and regular, with the frequency of oscillation affected by several parameters such as electrolyte conductivity, the rotation rate of the electrode, surface area, and configuration of the cell. The typical frequency of electrochemical oscillation is in a range of 0.01-10 Hz[106].

When samples were applied with a potential in the primary passive region, we observed current oscillations with periods of around 10 ks. The oscillations were categorized with two different curve shapes and termed regular oscillations (Figure 2.27a) and chaotic oscillations (Figure 2.27b). Oscillations with a frequency of ~0.01 Hz were also observed to be embedded in the later part cycles of the long-period oscillations, resembling those well reported in the Fe $|$ H_2SO_4 system. Irreproducibility was

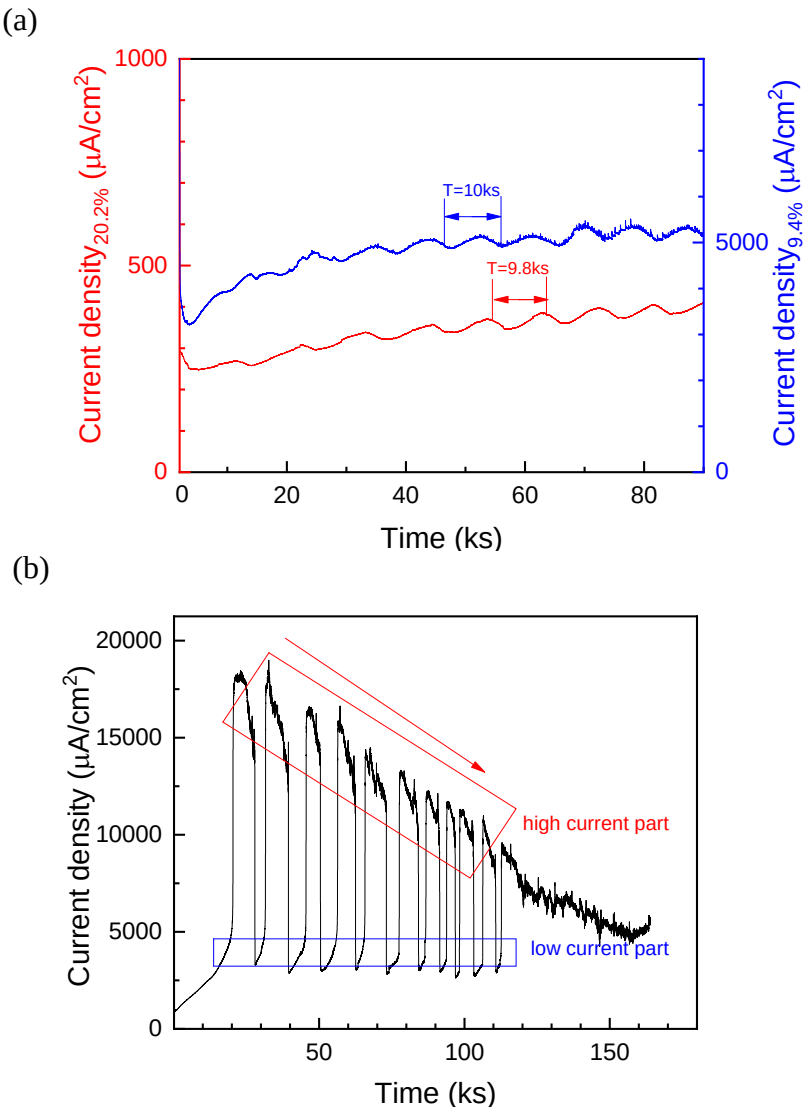

Figure 2.27. Regular oscillations with a fixed period are observed with samples of Fe-20.2 at.% Cr under a potential of -0.21V (red) and samples of Fe-9.4 at.% Cr under a potential of -0.15 V (blue); (b) Chaotic oscillations without a fixed period are observed with samples of Fe-11.6 at.%Cr under a potential of -0.09 V.

encountered with experiments set up with the same alloy composition and applied potential. Different oscillation types were sometimes identified under the same experimental setup, making it challenging to specify the exact potential regions for chaotic and regular oscillations. However, it was found that chaotic oscillations prefer

lower voltages, while regular ones tend to occur at a more positive potential. Meanwhile, a transition from regular to chaotic oscillations was sometimes observed after an extended time of dissolutions.

To the best of our knowledge, there is only one report of oscillatory behavior for Fe-Cr alloys in H_2SO_4, and this involved only alloys dilute (5 at.%) in Cr[74] with the reported oscillatory behaviors similar to those documented for pure Fe | H_2SO_4 system. Current oscillations are observed around the second passivation peak of the LSV conducted in strong sulfuric acids. However, the low-frequency oscillations we discovered show very different characteristics in aspects of oscillation frequency and amplitude.

As shown in figure 2.28, the surfaces after long time corrosion were examined by scanning electron microscopy (SEM) to track the origin of oscillations. The surface is sometimes mixed with rough parts where the grain boundary (GB) is deeply corroded in, and less rough parts where not much GB corrosion is recognized. Small particles were spotted at the bottom of the container and then collected and imaged by SEM. Based on

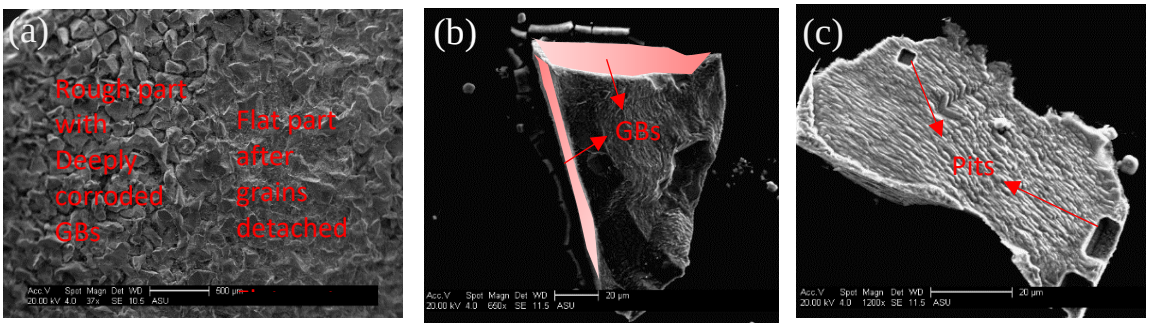

Figure 2.28. SEM images of corroded surfaces (a) and particles collected from the bottom of the container(b), (c), GBs and pits could be recognized in the images. Severe GB corrosion is observed; the particles collected in the bottom of the cell are grained dropped off when the attaching GBs are etched.

the flat surface, as highlighted by red in figure 2.28a, it is reasoned that severe intergranular corrosion leads to the detachment of whole grains. Flat parts of the surface are created when the attaching GBs surrounding the grains are “eaten” up, and the gains detach from the surface. Pits of various shapes are identified, locating at both grains bulk and GBs and telling the orientation of the grains: triangular one stands for (111) surface, and square one is for (001) surface.

The SEM results hint that those GBs corrosion and pitting may result in oscillations: GB corrosions and pits with limited dimension limit the diffusion of dissolved ion and facilitate film precipitation at relatively lower current density. They will initiate oscillations with frequency way off regular oscillation frequency resulting from very high current density. Rotating disk electrodes were employed to enhance the mass transport near-surface area other than GBs and pits for comparison. It is found that chaotic oscillations are less likely to transit back from the high current part to the lower current part (highlighted in figure 2.27), with current density maintained in high for an extended period of up to 50 ks.

One common origin for GB corrosion in steel is sensitization, which refers to the phenomenon that the precipitation of Cr carbides during heat treatment uptakes the elemental Cr along the GBs, rendering GBs to be less enriched with Cr and more vulnerable to corrosion. The temperature thermodynamically and kinetically favoring Cr carbides precipitation usually range around 500 – 700 ℃. Our high-purity samples (C concentration is about 23 ppm) and heat treatment are designed to suppress the sensitization. However, it is found that the precipitation of Cr carbides occurs much more easily in ferritic steel (BCC) than in austenitic steel (FCC). Because the carbon solubility

in ferritic steel is lower than austenitic steel and the diffusion rates of both C and Cr in the less dense BCC lattice are (two orders) higher[107]. Severe GB dissolution in acid was reported in a less pure Fe-20Cr alloy[108].

Precipitations with a size of hundreds of nanometers are identified at selected GBs. Figure 2.29 shows one of the most densely embedded GBs of a Fe-16.8 at.% Cr alloy, which has been polarized under peak potential for 500 s. Scanning transmission electron microscopy (STEM) EDS analysis recognizes that the precipitates are rich in Cr

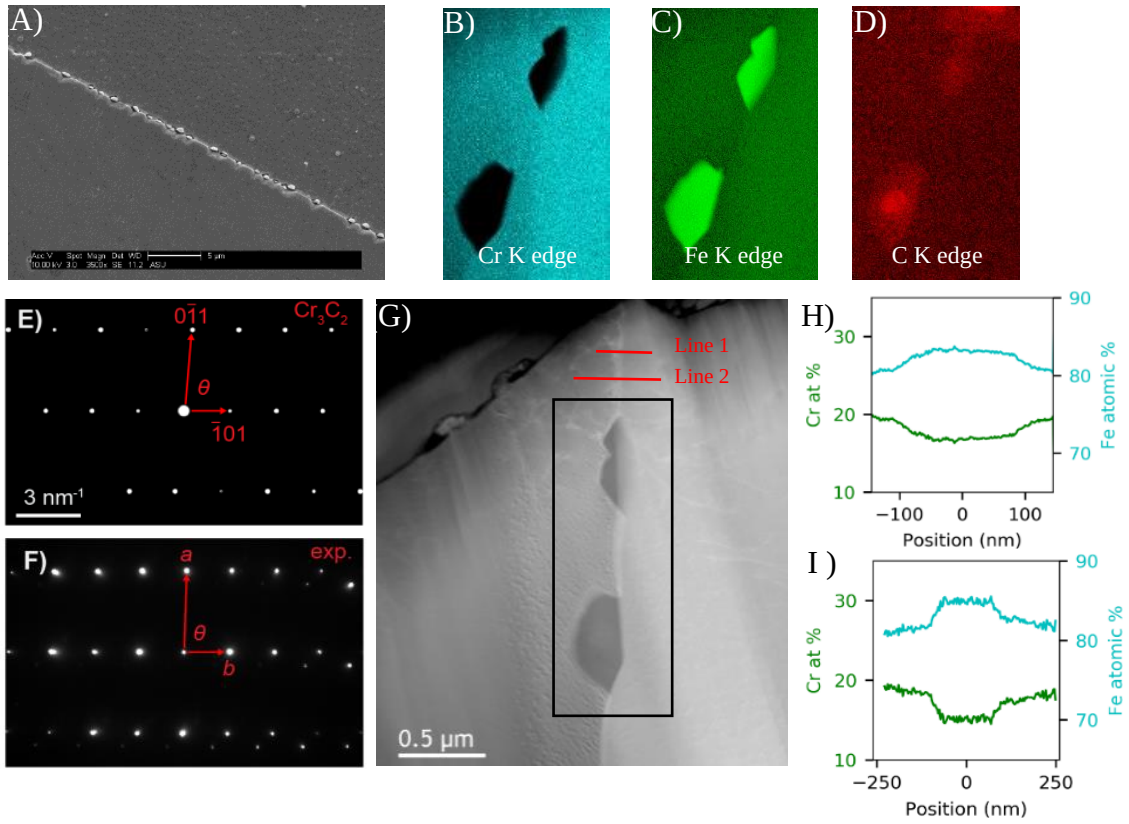

Figure 2.29. SEM and STEM analysis of the precipitation at GBs. (A) SEM image of the precipitation distribution after the surface of Fe-17 at.% Cr has been held at -0.2 V (around peak potential) for 500 s. (G) STEM- ADF image of the cross-section of a grain boundary with two precipitations. (B,C,D) The STEM EDS maps of the rectangular area in (G). (E, F) Simulated [111] SEAD of Cr_3C_2 and experimental SEAD of the top precipitation. (H, I) Concentration profiles of Fe and Cr atoms in line scanning labeled in (G), based on the EELS measurements of the Cr L-edge and Fe L-edge. STEM analysis was conducted by James L. Hart and Elaf Anber.

and C but have negligible Fe (figure 2.29b – 2.29d). Selected area electron diffraction (SAED) patterns are obtained and compared with the simulated diffraction patterns of common precipitates, $Cr_{23}C_6$, Cr_7C_3, and Cr_3C_2. It is suggested that the precipitate is likely a distorted Cr_3C_2 phase. Finally, STEM-EELS line scanning was performed in the vicinity of the GBs (line 1 and line 2 in figure 2.29g) to obtain the spatial distribution of Cr composition. It is observed Cr is depleted (15 at.% Cr) within 100 nm of the GB and the depletion quickly fades when stepping away from the vicinity of precipitates.

It is essential to clarify that the influence of the higher dissolution rate in GBs on examining our theory is insignificant. It is expected that the alloys with higher Cr content would experience more severe GB corrosion since the larger difference of elemental Cr concentration at carbides point from bulk material leads to a sharper contrast in terms of passivation. The 20 at.% Cr alloy that has been carefully examined shows the lowest Cr concentration of 15 at.% around the carbides. The depletion of Cr is only confined in the nanometer range around GB. As a result, the area-weighted average dissolved layer h for the primary passivation is supposed to be dominated by the passivation behavior of the bulk. The possible effects of GB corrosion are further excluded with the examination in Ni-Cr austenite systems, where sensitization is completely suppressed with water quenching from high homogenization temperature.

To sum up, a decreased Cr concentration is observed near the carbide precipitates in GB. This inevitable sensitization in ferritic steel is responsible for corrosion attacking around GB and accounts for the observed oscillations. However, short-time potential step experiments used for fitting the theory are supposed to suffer negligible effects from this sensitization effect.

CHAPTER 3

PASSIVATION OF NI-CR ALLOYS

3.1 Background

Ni-based alloys have been widely applied as industrial structure materials under extreme operational conditions due to their excellent mechanical as well as corrosion behavior. As another simplified binary alloy system from stainless steel, Ni-Cr alloys display a similar passivity transition as Fe-Cr alloys. Additionally, austenitic steel with FCC structure can dissolve more carbon and lower atomic mobility due to denser packed lattice. It is easier to suppress the sensitization when the Ni-Cr alloys are water quenched from the high homogenization temperature. The concern over the impact of GB corrosion encountered by Fe-Cr alloys could be quickly cleared up. However, there was notably less attention paid to the system. Among the investigation on Ni-Cr alloy passivation, most refer to high-temperature oxidation, leaving the aqueous passivation of Ni-Cr alloys incompletely characterized, let alone the composition-dependent passivity. Herein we explore the passivation behaviors of Ni-Cr alloys as a function of Cr composition and examine the capability of the percolation model in determining the critical composition of the system.

We started the study by comparing Ni-Cr alloys with the better investigated Fe-Cr alloys. The standard equilibrium potentials of these three elements to the oxidation states responsible for the protective passive films could indicate their relative passivity from the thermodynamic view[19].

$$Cr^{3+} + 3e^- \Leftrightarrow Cr(s) \qquad E= -0.74$$

$$Ni^{2+} + 2e^- \Leftrightarrow Ni(s) \qquad E= -0.25$$

$$Fe^{3+} + 3e^- \Leftrightarrow Fe(s) \qquad E= -0.04$$

The polarization curves of the pure metals in figure 3.1 compare the passivity with consideration of kinetic effects[109]. Elemental Ni can achieve passivation relatively more efficiently with a sharper active-passive transition peak and a lower critical passivation current than Fe. However, the passive films of Ni display less protectiveness with a significant amount of electrochemical dissolution observed in the passive range (~ 300 μA/cm^2), compared to the Fe in the same aggressive solution(~ 30 μA/cm^2). The increasing dissolution rate in the transpassive region is caused by the oxidation of the passive NiO film to soluble Ni^{3+}. The potential for the onset of the transpassive regime of elemental Ni and Cr is close so that in the transpassive dissolution of alloys, the corresponding passive film starts together. As a result, Ni is not protecting Cr from transpassive dissolution so that no secondary passivation is observed in the transpassive region of Ni-Cr alloys as in the Fe-Cr alloy system.

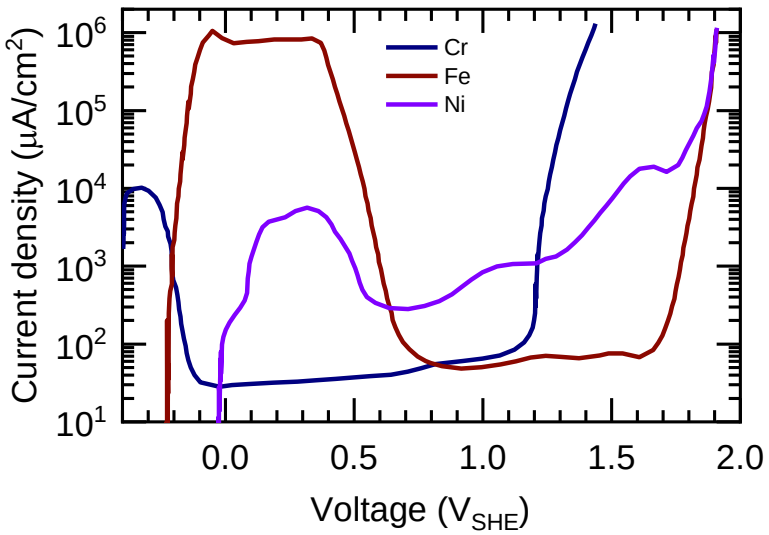

Figure 3.1. Anodic polarization curves of pure Fe (brown), Ni (purple), and pure Cr (blue) in 0.5 M H_2SO_4. Scanning rate: 1 mV/s[109].

Similar to the Fe-Cr alloying process, alloying Ni with Cr protects Ni from dissolution by negatively shifting passivation potential and decreasing the critical current and passive current. Figure 3.2 redraws the transition of the critical current density in Ni-Cr alloys over the gradual addition of Cr reported by Uhlig[110], a large drop of critical current density is found around 4 - 8 at.% Cr, even though he rationalized the electron configuration theory with 14 at.% Cr, where the decrease of the critical current stops, as the critical threshold.

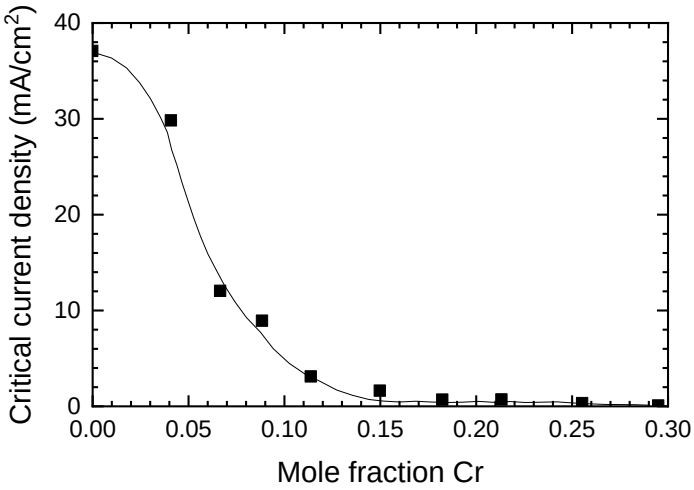

Figure 3.2. Critical current density is plotted as a function of Cr concentration for Ni-Cr alloys[110]. The LSV is measured in N_2 de-aerated 1.1N H_2SO_4.

The protectiveness of the passive film primarily depends on its structure and chemical composition. There is published literature[111–113] providing adequate spectroscopic data over the structural and compositional nature of the passive films on the Ni-Cr alloy system. Electrochemically formed passive films on pure Ni are found to be duplex-structured as Cr with the outer layer of hydrated $Ni(OH)_2$ in contact with the electrolyte and inner NiO part at the metal surface[13–16]. The passive films developed

on Ni-Cr alloys inherit the bilayer structure from constituent elements with both oxide and hydroxide layer enriched of Cr^{3+} in the acidic electrolyte.

The Cr enrichment in the films on Ni-Cr alloys is less pronounced when compared to Fe-Cr alloys because of the better passivity of Ni than Fe. The increasing pH suppresses the dissolution rate of Ni more rapidly than the one of Cr, yielding to a drop in Cr enrichment of the passive film[114]. Ni enrichment was even observed in the outer hydroxide layer when passivated in the deep passivation region and in the solution of high pH[111]. As shown in figure 3.3a, the Ni/Cr ratio reaches 15 around 0.3V, while the ratio in the parent alloy is 5. Pronounced enrichment of Cr was still reported in the acidic

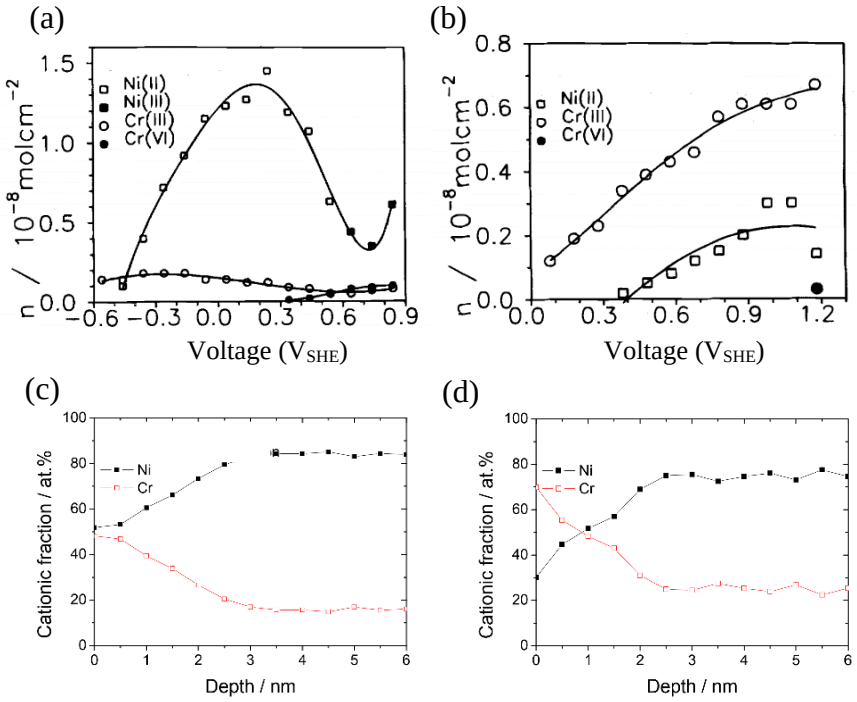

Figure 3.3. Effects of applied potential, pH of the solution, and alloy composition on the composition of passive films developed on Ni-Cr alloys. (a, b) The amount of Ni and Cr ions with the passive layer formed on Ni-20 at.% Cr when immersed in (a)1M NaOH (b) and 0.5 H_2SO_4 for 300 s, measured by X-ray photoelectron spectroscopy (XPS)[111]. (c, d) XPS depth profile for Ni and Cr for the passive film form on Ni-15 at.% Cr (c) and Ni-30 at.% Cr alloys (d) at 0.5 V_{SHE} in pH = 2.0 sulfuric acid solution for 24 h[113].

solution (figure 3.3b). Similar to Fe-Cr alloys, the Cr concentration in the film increases with the Cr content in the alloy[113]. As shown in figure 3.3c and 3.3d, the ratio of Cr/Ni is around 0.5 for the passive film on Ni-15 at.% Cr while around 1 for Ni-30 at.% Cr, when the other conditions were kept the same.

3.2 Experiments

3.2.1 Sample preparation

Ni-Cr alloys maintain in a single phase up to 45 wt.% Cr at 1200°C, well covering the range we are interested in, the phase diagram of the system is shown in figure [1]. Sets of alloys with various Cr compositions (5.0 at.%, 9.9 at.%, 11.7 at.%, 13.1 at.%, 14.9 at%, 16.7 at.%, 20.9 at.%, 23.1 at.%, and 24.1 at.%) were prepared with pure elements (99.99% Ni and 99.99% Cr, Goodfellows) by vacuum-arc-melting and machined by electrical discharging machining. Sealed in quartz with an atmosphere of Ar + 5% H_2, the samples were homogenized by solution annealing at 1100°C for 24 hours, followed by water quench to room temperature. The compositions were confirmed by EDS.

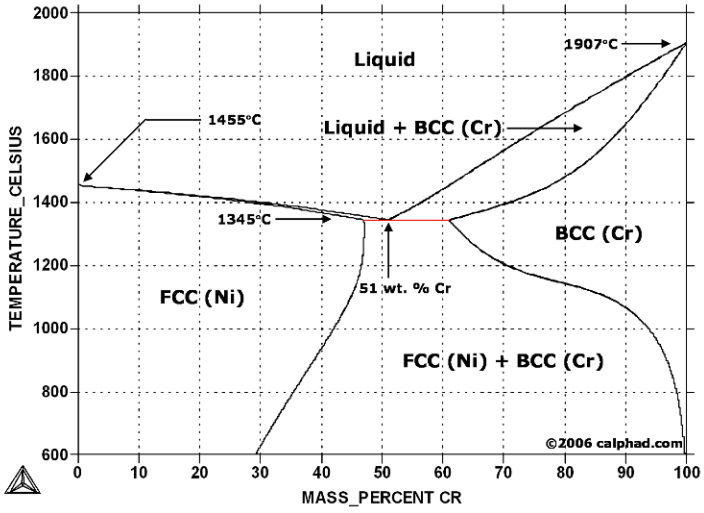

Figure 3.4. Phase diagram of Ni-Cr alloys[1].

3.2.2 Electrochemical Experiments

The same abrasion and reduction protocols for sample preparation and cell configuration of the electrochemical experiments are employed for Ni-Cr alloys as for Fe-Cr alloys. LSV was conducted with a sweeping rate of 5 mV/s. The chronoamperometry was conducted with the samples held at 0.02 V for 400 s to obtain the charge density required for primary passivation.

3.3 Validation of the percolation model – from 2D to 3D transition effects

3.3.1 Passivity of Ni-Cr alloys

Figure 3.5a and 3.5b show the polarization curves of Ni-Cr alloys with various compositions and the current-voltage behaviors of pure Cr and Ni. Assigning the transition peaks of Ni-Cr alloys to the passivation of the constituent elements is not as elucidate as for Fe-Cr alloys. The first active-passive transition peaks, located in the range of [-100 mV, -50 mV] concerning the one of pure Ni, probably result from the passivation process of Ni atoms. All the Ni-Cr alloys carry a small second active-passive transition peak resembling the one in pure Ni. As a result, it is reasonable for one to speculate that the two peaks appearing in the LSV of the alloys are both contributed from Ni passivation.

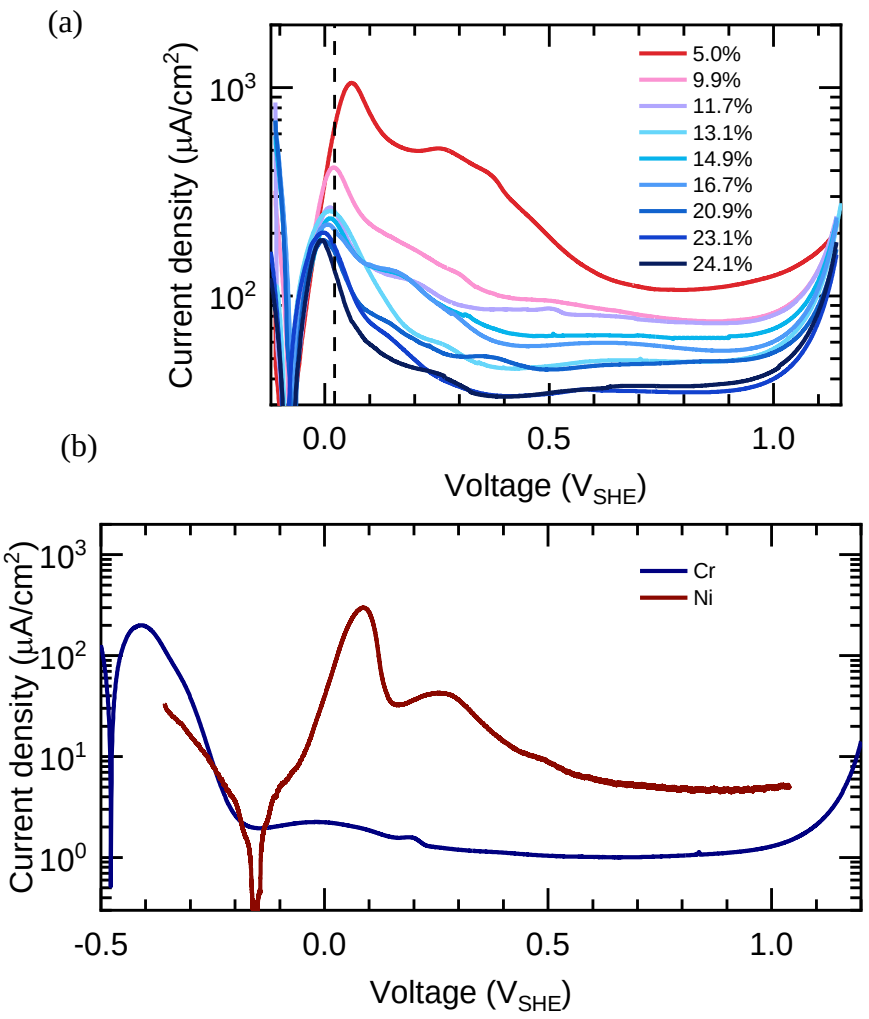

Figure 3.5. LSV of Ni-Cr alloys and pure metals (a) Linear sweep voltammetry results of Ni-Cr alloys with various Cr concentrations in 0.1M H_2SO_4 (the scanning rate is 5 mV/s). The Dash line marks the potential for chronoamperometry. (b) Anodic polarization curves of pure Ni (brown) and pure Cr (blue) in 0.1 M H_2SO_4. Scanning rate: 5mV/s. The Ni surface is electropolished in 70% concentrated H_2SO_4 at a current density of 20 mA/cm^2 for 3 min after mechanical polishing.

Ni is relatively decent catalysis for H_2 evolution reaction (HER)[115], the kinetically favored H_2 reduction arises the OCP of Ni-based alloys up to -0.1 V. The high negative current of H_2 reduction may offset and "burry" the anodic peak of Cr passivation. The transition peak for Ni passivation persists in the polarization curves of high Cr concentrated alloys above 13 Cr at.%. In contrast, Fe-Cr alloys with the same

composition passivate with only Cr passivation peak. The reason that the Ni passivation peak persists into high Cr concentration may be that the Ni dissolution is activated at a higher voltage and proceeds with a lower rate when compared to Fe, as shown in figure 3.1. The overlap of Cr passivation and Ni dissolution is less than Cr passivation and Fe dissolution. Without the help of Ni dissolving in, only Cr atoms in the outer surface are oxidized. In that case, a protective passive film will not be developed until Cr at.% reach above the 2D percolation threshold, p_c^{2D}, that is 29.5% for distance up to the 2nd NN in FCC {111}[88].

The critical current density and the peak potential were collected and plotted as a function of Cr content in figure 3.6a and 3.6b. Compared to a potential shift of -400 mV in Fe-Cr alloys within the same composition range, the peak in Ni-Cr alloys shows a relatively smoother transition with a potential difference of -70 mV. The smaller difference in the Ni-Cr system is explained by the "closer" passive properties between Ni

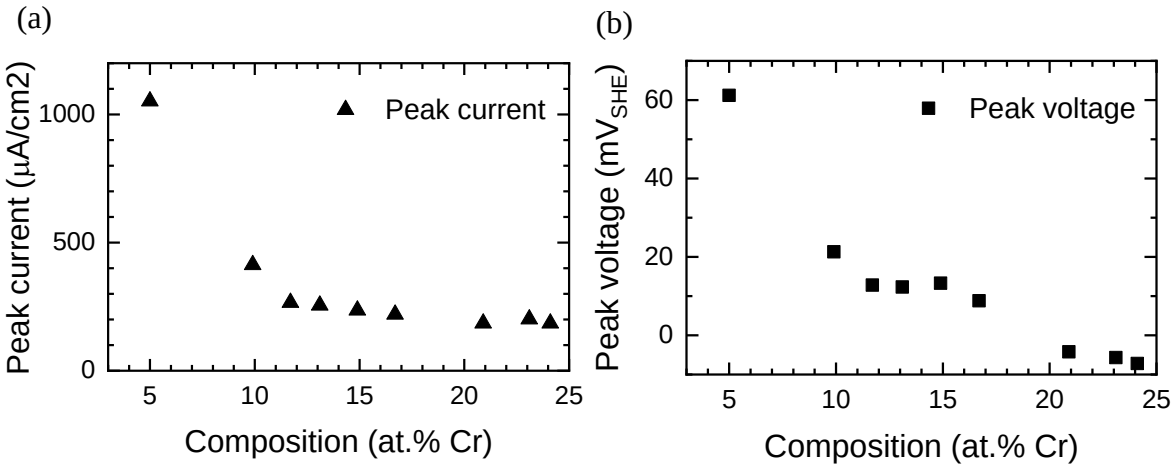

Figure 3.6. (a) The changes of critical current and (b) the potential of the first peak is plotted as a function of Cr concentration. Data points are collected from the LSV curves of Ni-Cr alloys in figure 3.5a.

and Cr, when compared with Fe and Cr couple. The significant decrease of the critical current locates in the range of 5 – 10 at.%, which shows a decent agreement with Uhlig's results[110]. This range also witnesses a considerable portion of the change in passivation potential. However, the decrease of passivation potential does not stop but persists into higher Cr concentrated alloys at a relatively slower rate.

3.3.2 Cluster size effects on electrochemical properties

Only 70 mV difference in the passivation potential is observed between 5 at.% and 24.1 at.% Ni-Cr alloys. A slighter alteration of the electrochemical properties by alloying is expected for Ni-Cr alloys, which means during the primary passivation, Ni clusters are dissolved in a way closer to elemental Ni and Cr clusters develop oxide film more like pure Cr does. Table 3.1 summarizes the adsorption energy of oxygen and water on Cr-substituted Ni surfaces as a function of the Cr cluster size[116], compared to our calculation results of pure Cr. The published paper only reported the scenarios of the surface doped with Cr monomer and dimer. Without the exactly same simulation condition, the comparison is roughly conducted as follows: The adsorption energy of oxygen and water on the monomer-doped surface has reached 62% and 41%, respectively, of the difference between the pure elements. Dimer brings up the value to 65% and 48%. The converge rates are comparable to the adsorption energy of the Fe surfaces doped with Cr dimer. It is secure to conclude that the electronic effects play a negligible role in the composition range examined.

Table 3.1. Adsorption energy(E_{ad}) of O_2 and H_2O on Cr-doped Ni(111) surfaces from[116] with $E_{ad}(O_2)$ is converted from $E_{ad}(O)$ reported from the reference added by $\frac{1}{2}$ $E_{bind}(O2)$ compared to pure Cr (110) from the present calculations with the top adsorption site.

Surface	$E_{ad}(O)$ (eV)	$E_{ad}(O_2)$ (eV)	$E_{ad}(H_2O)$ (eV)
Ni	-3.78	-0.85	-0.52
Ni-1Cr	-5.88	-2.95	-0.80
Ni-2Cr (top layer)	-5.96	-3.03	-0.85
Ni-2Cr (top and 2nd layer)	-5.99	-3.06	-0.80
Cr	-	-4.24	-1.21

3.3.3 Identification of the primary passivation region

Based on the results from simultaneous electrochemical polarization and ICP-MS analysis, Scully recently reported an early dominance of kinetically favored hydrated $Ni(OH)_2$ in passive film and ascribed this phenomenon to the strong epitaxial relationship of $Ni(OH)_2$ with FCC Ni-based alloy[117]. While after the alloys being polarized with longer times, e.t. 100 s, the higher thermodynamic stability of Cr_2O_3 and $NiCr_2O_4$ ($\Delta G_f^0(Cr_2O_3) = -1058\ kJ/mol,\ \Delta G_f^0(Ni(OH)_2) = -216\ kJ/mol, \Delta G_f^0(NiCr_2O_4) = -1257\ kJ/mol$) leads to a preferential Ni dissolution, thus the involution to Cr-rich passive films. However, the massive contribution of Ni to the initial passivation identified by Scully is under an experimental condition of much less acidic solution (pH of 5.5) and

a higher passivation potential (0.4 V) than ours. Ni hydr(oxide) formation is supposed to be more thermodynamically favored than ours, and thus a higher contribution from Ni would be expected.

With the help of online ICP-MS, the current density associated with Ni/Cr participating passive film growth or dissolution was extracted from the total current density. The pronounced dissolution selectivity of Ni helps to identify the potential range corresponding to primary passivation. Figure 3.7 shows curves for how the dissolution selectivity changes with applied potential are obtained for alloys with three critical Cr concentrations. The shape of Ni selectivity verse potential curves looks similar to the one of Fe-Cr alloys. A verse selectivity, selective dissolution of Cr, follows the Ni passivation peak of the 9 at.% alloy, of which the Cr_2O_3 developed during Cr passivation is not yet protective and continues to be undercut during Ni dissolution. When Ni passivation dominates, the undercut Cr_2O_3 clusters enrich the Cr ratio in the analyzed solution. Compared with Fe-Cr alloys, a heavier preferential dissolution of Ni is recognized in the passivation region, probably resulted from the chemical dissolution of less stable Ni (hydr)oxide.

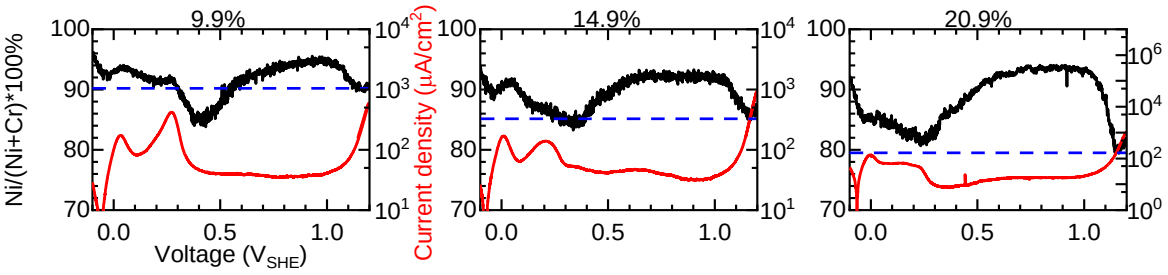

Figure 3.7. Online ICP-MS measures Ni (black) dissolution selectivity in Ni-Cr alloys as a function of the applied potential. It is plotted together with corresponding LSV (red) in 0.1 M H_2SO_4. The scanning rate is 5 mV/s. The dashed blue lines mark the Ni at.% in the alloy. ICP-MS experiments were conducted by Pietro P. Lopes.

As long as Ni dissolution starts, the lower potential is applied, the less Ni participates in passivation. However, in Ni-Cr alloys, the current contribution from high rate HER needs to be intentionally excluded by stepping the potential above 0 V. As a result, the potential region around the first peak LSV is recognized to best approach a state of primary passivation. ICP-MS results support the dissolution selectivity of Ni in this region, even though how many Ni atoms participate in the passivation remains unknown.

As shown in figure 3.8, the converted ICP-MS current density well matches the electrochemically measured one, indicating the undercutting phenomenon is much slighter in the Ni-Cr system than the Fe-Cr system. A possible explanation is that the lower dissolution rate of Ni significantly decreases the rate of destroying Cr oxide network and thus reduces the possibility of undercutting. On the other hand, the Ni electrode absorbs H_2 evolving, forms some Ni hydrides during the reduction process and serves as an H reservoir[118,119]. The H is then oxidized during anodic polarization and

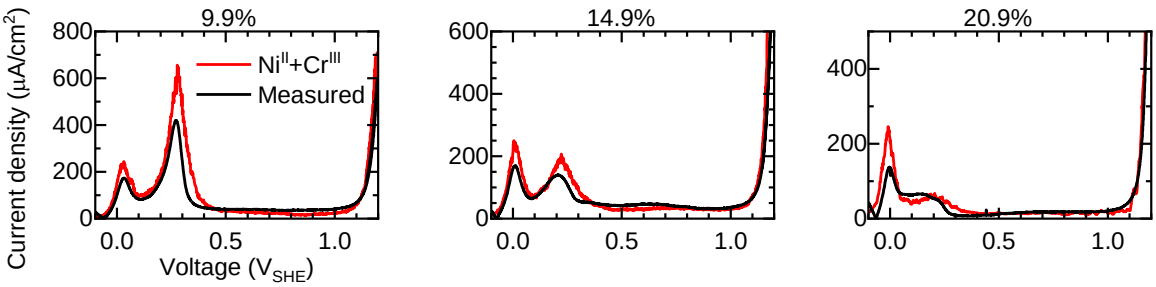

Figure 3.8. Current density for ionization and dissolution into solution during passivation of Ni-Cr alloys. Current density (black) is converted from the mass density dissolution rate measured by online ICP-MS, Cr is assumed to be dissolved in forms of Cr^{3+} and Ni in forms of Ni^{2+} and electrochemical measured LSV (red) in 0.1 M H_2SO_4. The scanning rate is 5 mV/s. ICP-MS experiments were conducted by Pietro P. Lopes.

contributes to an anodic current background in LSV but is not detected by ICP-MS converted current density, further narrowing the difference between them.

3.3.4 2D to 3D transition in passivation behaviors of Ni-Cr alloys

As shown in figure 3.9, the current density at 0.02 V is collected and plotted against Cr concentration. A significant decrease in the current density is observed around 5 at.% Rh. With the integrated current obtained under a potential of 0.02 V, the number of dissolved monolayers, h, is calculated on the primary FCC {111} surface through equation 3.1,

$$number\ of\ layers\ dissolved = \frac{\int_0^t I\,dt}{A} \Big/ \frac{4*(3*C+2*(1-C))*q}{\sqrt{3}*a_{Ni}^2}, \quad (3.1)$$

where A is exposed surface area, I is the magnitude of measured current, C is the mole fraction of Cr, q is the elementary charge, and a_{Ni} is the lattice parameter of fcc Fe. Cr

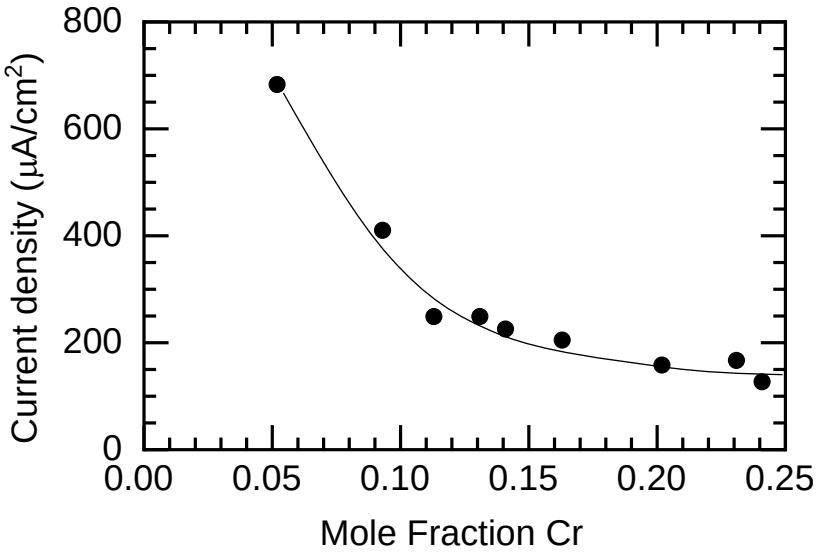

Figure 3.9. The current density transition at 0.02V over the Cr concentration, collected from the LSV in figure 3.5a.

and Ni are assumed to be oxidized to Cr^{3+} and Ni^{2+}, respectively. The lattice parameter does not vary with Cr at.%.

Figure 3.10 displays an excellent fitting of the passivation behaviors of Ni-Cr alloys to the 2D to 3D percolation transition, with fitted p_c^{3D} value of 5.2 %, a value close to the critical value presented in figure 3.2 and 3.9. For FCC Ni-Cr alloys (a_0= 3.50 Å), the 3rd NN is noticeably larger (0.25 Å) than the maximum distance, while the 2nd NN is much smaller (0.68 Å). As a result, the critical threshold for passivation is expected to lie in between corresponding interactions including up to 3rd NN (p_c {1,2,3}) and 2nd NN (p_c {1,2}), which is 6.1 % and 13.6 %, respectively[55]. However, the value we obtained is slightly below p_c^{3D}{1,2,3}. The discrepancy could be explained by the already initiated passivation of Ni under the applied potential. The participation of Ni in passivation would lower the criterion for Cr percolation. The slightly lower percolation threshold than the

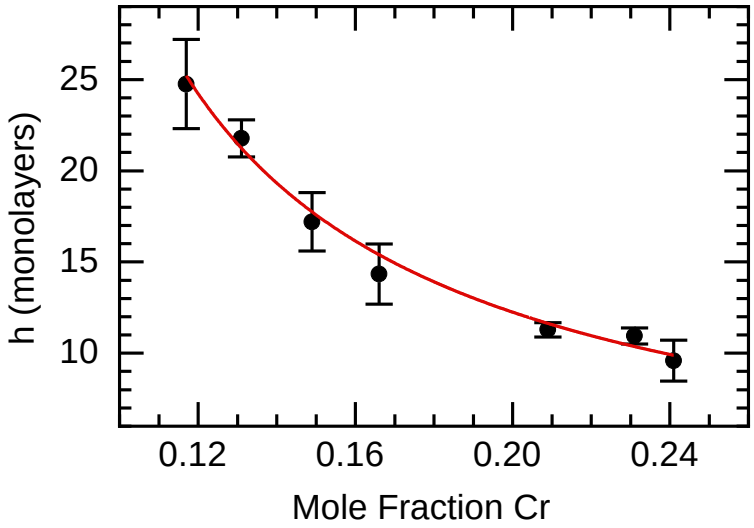

Figure 3.10. Equation for the 2D-3D cross-over effect is fitted with the passivation behavior of Ni-Cr alloys with polarization under 0.02 V for 100 s. The number of dissolved layers is plotted as a function of bulk Cr composition. The red curves correspond to the fitting results with the equation of $p_c(h) = p_c + c\,h^{-1/\nu}$ with v = 0.878 used for the 3D lattice.

prediction indicates that under the potential selected, Ni contributes to alloy passivation. The smaller overlap between the potential region for Ni dissolution and Cr passivation makes it more challenging to locate the primary passivation and exclude Ni from passivation as much as possible, let alone the contribution from the oxidation of incorporated H needs to be considered. Another possible reason for the deviation is the impact of atomic configuration, as previously discussed. The tendency of Cr atoms towards clustering will lead to the relaxation of Cr percolation, thus a lower p_c^{3D}.

3.4 Passivation and dissolution of pure Ni

3.4.1 Background

Ni is a significant element in numerous structural materials, including stainless steel. With the increasing interest of Ni-containing electrodes used in plenty of electrochemical systems such as batteries and electrocatalysis, numerous investigations have been motivated to study the aqueous dissolution and passivation mechanism of pure Ni. The chemical and structural properties of the passive film developed on Ni have been well established via electrochemical and surface analytical techniques, both in-situ and ex-situ[13,15,120–123]. A duplex-structured passive film has been reported with the inner NiO in parallel or antiparallel epitaxy with the substrate lattice, and the hydrated outer layer is in the form of α-$Ni(OH)_2$ under relatively lower potential and is stabilized to β-$Ni(OH)_2$ at more anodic voltages. The latter is harder to be reduced cathodically.

Several groups have reported In-situ electrochemical STM elucidations of the electrochemical processes occurring on the Ni single crystal surface in the atomic scale. Most of the experiments were conducted in a slightly acidic or alkaline solution so that the surface roughening by dissolution could be suppressed[12,14,16]. The air-formed

oxide on Ni is observed existing with amorphous hydrated Ni oxide islands on top of a triangular-shaped NiO thin film. Cathodic reduction under a potential just below OCP can provide a principally clean surface but with terraces roughed by dents and pits that are created due to the difference of Ni density in between NiO and metallic Ni. A stable rough surface over time suggests the low mobility of Ni atoms on the surface. The slow surface diffusion of Ni has been associated with the pinning effect by the adsorption of species like O[14], OH^- and SO_4^{2-} [124]. A pronounced non-uniformity has been reported under the dissolution potential, with the development of dents at the steps and evolutions 3D pits on the terrace. Accompanied by the dissolution process, passivation starts with small islands emerging at steps. With higher potential or extended time, the nucleation and growth of the film result in a surface entirely covered by grain-like morphology.

One puzzling feature that has been significantly less investigated is the multiplicity of current peaks related to the anodic dissolution and passivation of pure Ni in sulfuric acid, which has been occasionally observed in the polarization curve of Ni since the 1960s[125–129]. The multiple peaks can hardly be ascribed to sequential oxidation reactions since there is only one stoichiometric oxidation state of Ni in a stable passive oxide, Ni^{2+}, before it reaches the state of transpassive dissolution. Several explanations associate the additional peaks to other reactions, such as the dissolution of impurity adsorbed Ni surface[125], the oxidation of Ni hydride that is incorporated during reduction[130], the transition of NiO from the hydrated $Ni(OH)_2$ layer[126]. However, none of them is either consistent or has been fully substantiated. Nevertheless, one sure thing is that the shape of the polarization curve could change a lot by various sample preparation protocols. To advance our understanding of the passivation and

dissolution mechanism of Ni, we here focus on the investigation of the surface states related to two of the reported anodic peaks by systematically changing the perturbation conditions.

3.4.2 Results and discussion

We find an unstable additional peak of Ni when investigated the passivation and dissolution behaviors of Ni-Cr alloys, as mentioned earlier, which leads us to the study of pure Ni. A series of experiments were designed to advance the understanding of the factors dominating the peaks in the Ni polarization curve. These factors include crystallography, anions in the solution, reduction recipes, polishing protocols, scanning rates, dissolved oxygen in the solutions, and scanning rate.

Figure 3.11 shows the polarization curve of single crystals with two orientations. A characteristic two-peak nature (marked as peak I and peak II in figure 3.11) is observed during the anodic scanning in CV (a similar curve is also obtained for polycrystal but not shown in this figure). Starting from the second cycling, the peak I sees profoundly increasing intensity while peak II is significantly suppressed. After that, the curve shape in the following cycling is stabilized with high current density in peak I and a less prominent peak II. The single-peaked polarization curves obtained in similar experimental conditions from Magnussen[15] and Marcus[131] are cited for comparison.

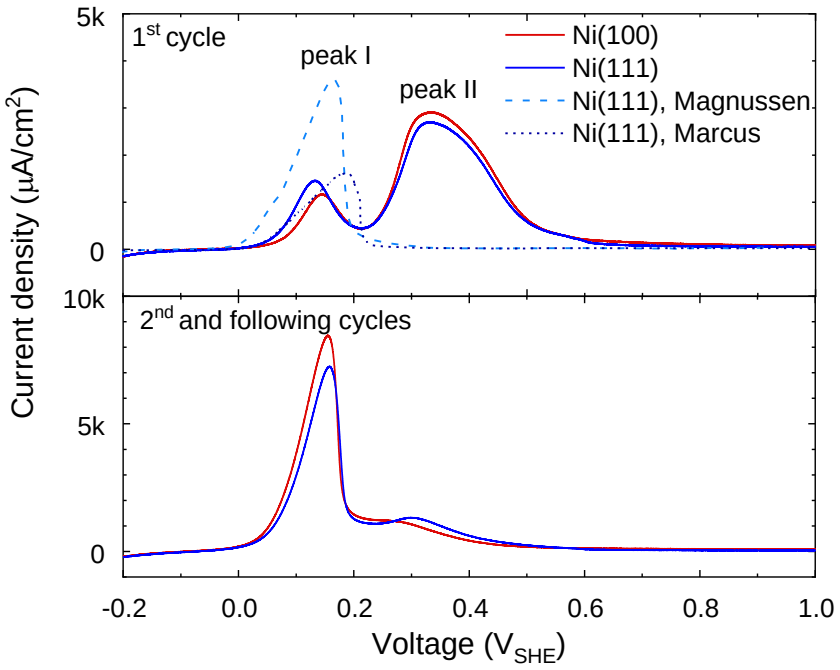

Figure 3.11. Cyclic voltammetry of single crystals with two orientations in a voltage range of [-0.4 V, 1.1 V] with a 5 mV/s scanning rate after being reduced at - 0.8 V for 300 s. Only anodic scanning is displayed for clearance. The dashed line is the curve digitalized and replotted from Magnussen's result[15], performed in 0.05 M H_2SO_4 with a scanning rate of 10 mV/s. The short dashed line is from Marcus[131], obtained in pH = 3 sulfuric acid with a scanning rate of 5 mV/s.

The recipe for the single-peaked curve was firstly reported by MacDougall[125] and later adopted by many researchers like Magnussen and Marcus. This widely acknowledged peak is found to be better aligned with the peak I from our curves. The impact of anions in the solution is studied by comparing the results in sulfuric and perchloric acids. No noticeable difference is observed with respect to the shape of the curve so that the results are not displayed here.

The relative current heights of the active-passive transition peaks could be more dependent on the topographic morphology of the electrode surface, which is easily

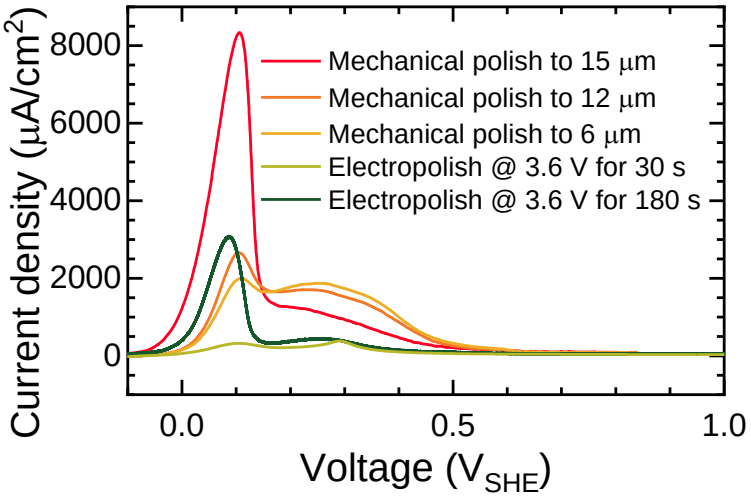

Figure 3.12. LSV of Ni polycrystal with a 5 mV/s scanning rate after being reduced at -0.8 V for 300 s. The surface is either mechanically polished or electropolished right before immersion into the electrolyte. Mechanical polish with different finishing as well as electropolish with different times is compared. Electropolish is conducted in concentrated 75% H_2SO_4 with a two-electrode configuration; Ni foil is used as the counter as well as reference electrode. Current density is calculated with the current divided by the exposed area of the sample.

perturbed by various polishing pretreatment. Figure 3.12 shows the LSV of polycrystal Ni polished by different protocols. Despite the specific area of the electrode surface changed by different roughness, the shape of the curve is dramatically altered by changed surface pretreatments.

Electrochemical reductions applied to get rid of the air-formed Ni oxide is another factor altering the shape of the obtained polarization curve. Figure 3.13 compares the LSV curves of the Ni polycrystals reduced with different potentials and time. A more cathodic potential and longer reducing time tend to positively shift the peak II positively and increase the current intensity. In a sulfuric acid with a pH of 3, Itaya[132] has reported in-situ STM observation that air-formed oxide could be actively dissolved when the potential is held at -0.26 V. Magnussen[15] also reported that a bare surface could be

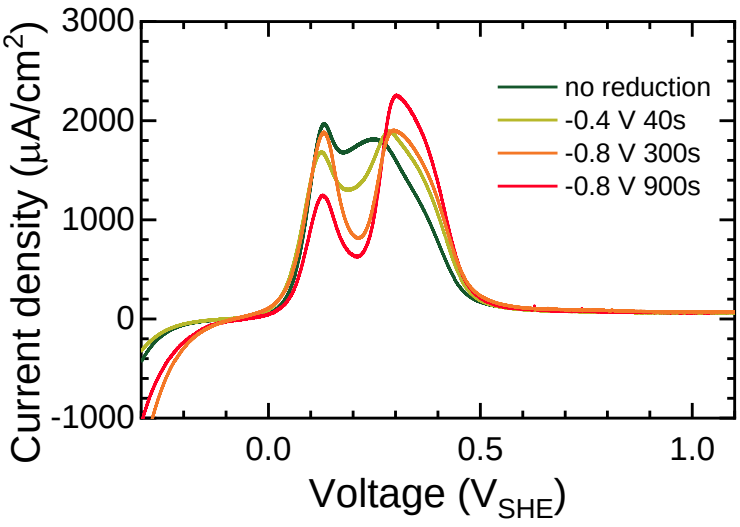

Figure 3.13. LSV of polycrystal Ni with a scanning rate of 5 mV/s. The surface is mechanically polished with a finish to 1 μm. Different reduction recipes are applied after the sample being immersed in the solution.

maintained under -0.2 – 0 V in 0.05 M H_2SO_4. Here, the reductions with lower potentials are applied in a more acidic solution, which is believed to completely remove the air-formed oxides. On the other hand, an apparent two-peak feature is observed for samples polarized following immersion into the solution without reduction, excluding the explanation that relates either peak to the oxidation of Ni hydrides[130].

While the reduction of air-formed oxide is addressed in figure 3.13, extended cyclic voltammetry is employed to address the voltages for aqueous passivation and the corresponding reduction, as displayed in figure 3.14. Cycling with increasing anodic limits firstly increasing the intensity of peak I. The orangish 2nd cycle curve in figure 3.14a shows a higher current density than the black curve of the 1st cycle. Both peaks are passivated when anodic limits surpass the root of peak II, 0.84 V. In figure 3.14a, both peaks of the greenish curves show a low current density after passivation in the 1st cycle.

Figure 3.14b, on the other hand, shows how the decreasing cathodic limit gradually recovers the two peaks after they are passivated at 1.04 V in the 1st cycle. It is found that when passivated at high potential, the first peak can be recovered with a short time (~ 40 s) reduction below -0.16 V. However, the peak II can fully restore the intensity only if a profound reduction (like 300 s at -0.8 V, the result is not shown here) is conducted before the 2nd cycle.

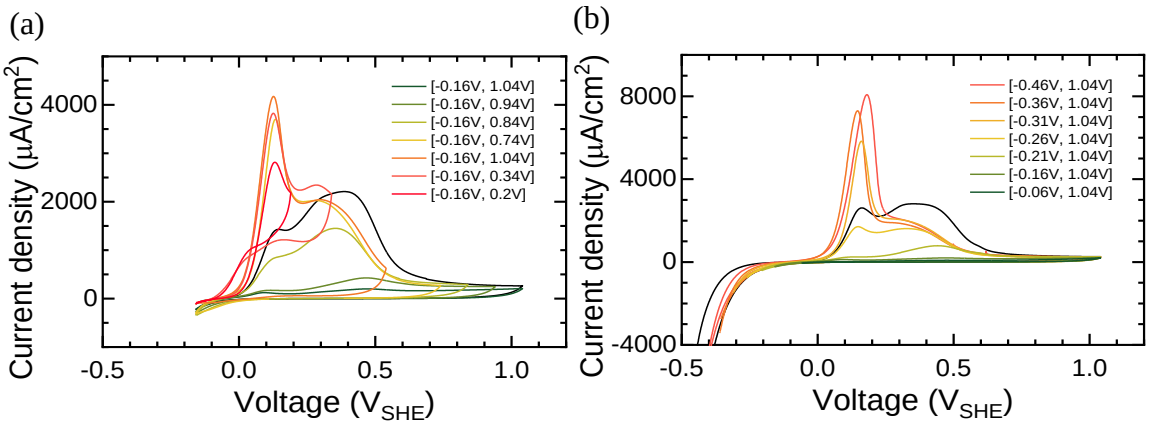

Figure 3.14. Extended CV with (a) increasing anodic limits and (b)decreasing cathodic limits. The scanning rate is 20 mV/s. The surface is polished with finish to 6 μm. Except that the black one corresponds to the 1st cycle of the CV with the widest scanning range, all the colored curves shown here are the 2nd cycle of the CV to address the change by passivation/reduction with different scanning range. The 1st cycle of different scanning ranges basically overlaps with each other. Only the one with the widest scanning range is used as a reference for locating the change of 2nd cycle.

Polarization curves obtained with different scanning rates are supposed to improve the distinction between the processes of different kinetic parameters. As shown in figure 3.15, a more prominent peak II under a higher scanning rate probably indicates it corresponds to a more kinetically favored reaction than peak I. However, at an extremely slow scanning rate of 0.1 mV/s, an additional peak (peak III) shows up with a relatively high current density, following the peak II. Moreover, the current density of peak II at 0.1 mV/s is way higher than the one at 1 mV/s, deviating from the trend of the rest curves at higher scanning rates.

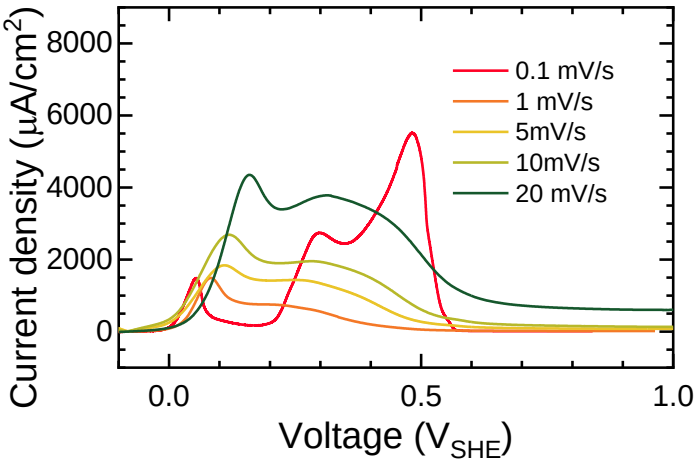

Figure 3.15. LSV of polycrystal Ni with a scanning rate of 5 mV/s. The curves are compared for solutions with or without de-aeration (UHP N_2 for 30 min).

Another interesting phenomenon is that the existence of O_2 almost doubles the intensity of peak I, but a less appreciable influence was observed on peak II, as shown in figure 3.16.

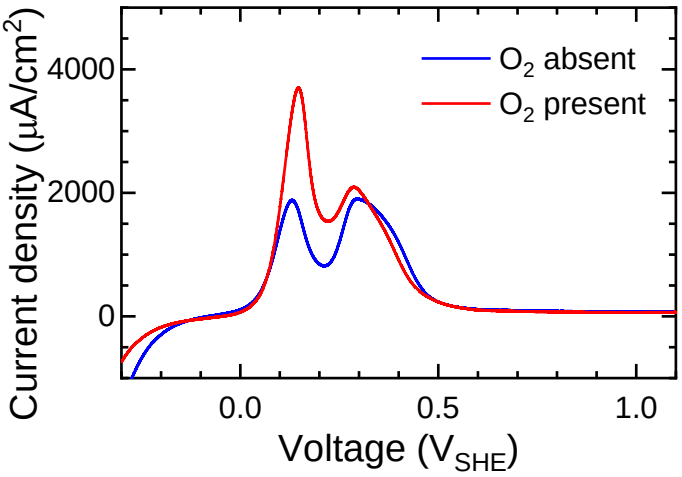

Figure 3.16. LSV of polycrystal Ni with varying scanning rates. The surface is mechanically polished with finish to 6 μm and reduced at 0.8 V for 300 s.

Even though we currently do not understand the exact mechanism dominating the multiplicity of transition peak, the results reported here strongly suggests a possible impact from the surface states of Ni. Our investigations yield a comprehensive summary of how some factors like experimental conditions and sample pretreatments factors could impact the peaks, which sets up a good start for future investigation.

CHAPTER 4

PASSIVATION OF CU-RH ALLOYS

4.1 Background

Since the application of automotive in the modern world, developing effective catalysis that could ultimately oxidize nocuous exhaust gases like nitrogen oxides, carbon monoxide, and hydrocarbons has been laid at the door of material scientists and engineers. A noble metal, like Rh, displaying high catalytic activity in nitrogen oxides conversion, is typically a crucial catalysis constituent. However, the scarceness of Rh makes it one of the most expensive metals. Replacement of Rh with the Rh-Cu alloy system is a commonly used solution to reduce the excessive use of Rh. Since the nonstoichiometric Rh oxide form on the surface is the main factor for its high catalytic activity, the alteration of Rh electronic structure during the alloying process with Cu will undoubtedly change the catalytic ability[133].

Electrochemical studies of the alloy system could help identify some common open questions in alloy passivation and catalysis, such as the clustering effect, and contribute to the catalysis community. The electrochemical behaviors of the Cu-Rh alloys reported in the literature[135] are quite interesting. The system shows passivation behaviors in a way like Fe-Cr and Ni-Cr alloys do. The formation of nanoporous Rh was reported in both active dissolution and transpassive dissolution regimes, where Cu is believed to be dissolved from the surface passivated by Rh oxide. The reactions at the interface seem to satisfy our assumption of primary passivation, where one alloy component is dissolved while the other passivates the surface.

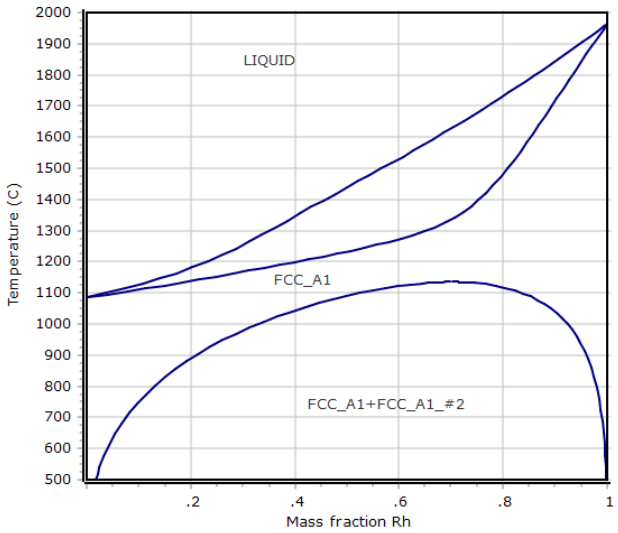

Figure 4.1. Phase diagram of Cu-Rh alloy system[133].

Cu-Rh alloy system is potentially attractive to the percolation model also because the system shows complete solubility across a broad compositions range [134], as the phase diagram in figure 4.1 shows. The possibility of the Cu-Rh system maintaining a single-phase status expands the compositional space of passivation studies. Theoretically, the sluggish phase segregation into two FCC structured alloys in the narrow spinodal region could be overcome by rapid quenching so that a single phase is obtained.

4.2 Experiments

4.2.1 Sample preparation

Cu-Rh alloys with Rh mole fraction of 7%, 10%, 13%, 16%, 18%, 20%, 22% were prepared by arc melting methods (Cu wires of 99.999%, Rh sheets of 99.95%) under argon atmosphere. EDS is utilized to examine the homogeneity of the samples. Ingot samples (with a diameter and a thickness of 5 mm) are machined with EDM after being homogenized at 1000˚C for a week and quenched in water. The sample surface is mechanically polished down to 1 μm roughness before each electrochemical experiment.

4.2.2 Electrochemical experiments

Anodic polarization and chronoamperometry experiments were performed in the cell with the same configuration used in the electrochemical experiments of Fe-Cr alloys and Ni-Cr alloys but following a reduction process of -0.2 V for 100 s. The protocol employed was proved to achieve the complete reduction by the same chronoamperometry collected after being reduced for a longer time (500 s) and lower reduction voltage (-0.5 V). A fresh solution was applied to each experiment. N_2 gas flow is used to thoroughly de-aerate the solution and is floating above the solution to maintain a low concentration of dissolved oxygen during the experiments. Polarization curves were obtained with a scanning rate of 5 mV/s. Current decay data were collected within the initial 400 s after the electrode is pulsed at the selected potential.

4.3 Validation of percolation model – from 2D to 3D transition effects

4.3.1 Passivity of Cu-Rh alloys

Figure 4.2a shows the polarization curves of Cu-Rh alloys of different compositions. Two pronounced transition peaks characterize the curves we obtained. The results are different from the single-peaked curves reported by Haijun, as shown in figure 4.2b. The discrepancy on the first peak could be explained with an incomplete reduction protocol and the experimental conditions Haijun adapted. Haijun did not de-aerate the

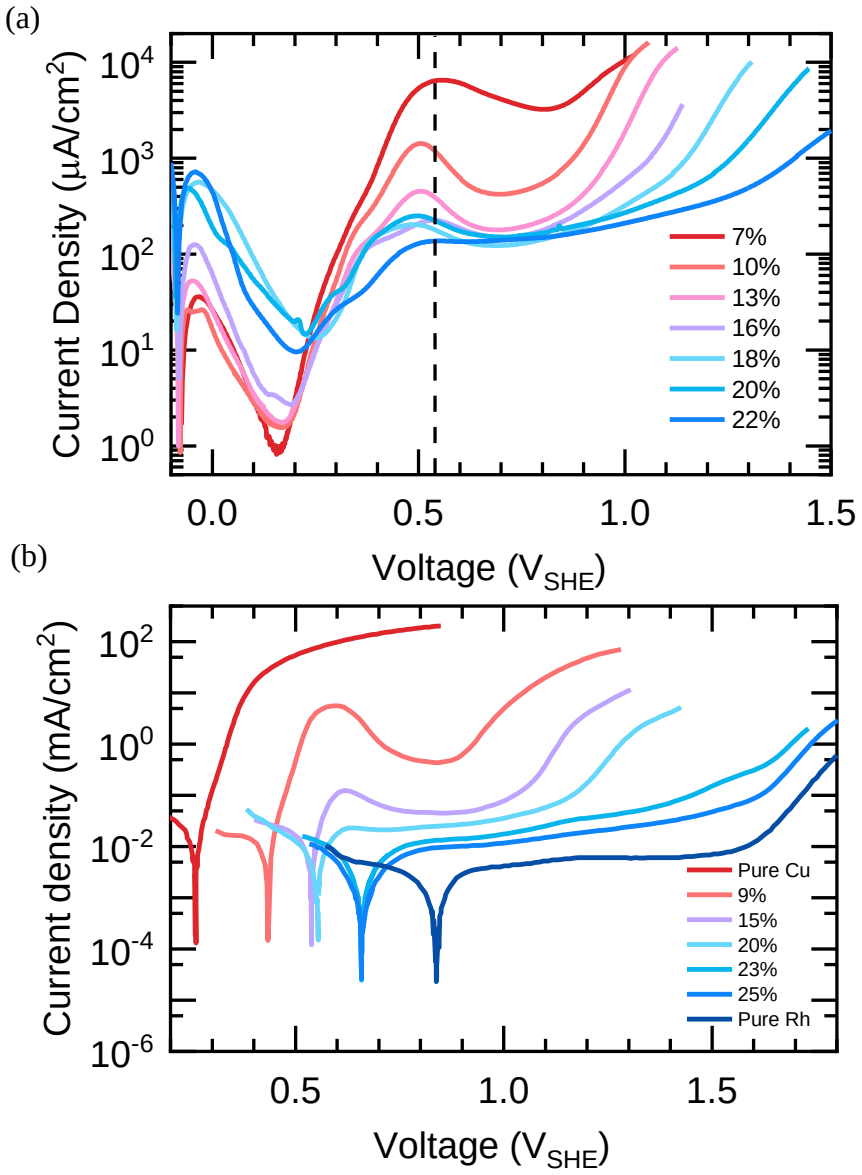

Figure 4.2. The LSV curves of Cu-Rh alloys (a) we obtained in 0.1 M H_2SO_4 with a scanning rate is 5 mV/s and (b) redrawn from Haijun's results[135] in 1 M H_2SO_4 with a sweeping rate of 1 mV/s.

solution from oxygen. And no reduction process was conducted before LSV but starting scanning form a relatively low potential, 0.14 V. The potential he chose is believed to be higher than the passivation potential of Rh, e.t. 0 V in figure 4.2a.

A reaction peak around 0 V is observed in all the alloys we tested. The peak is believed to correspond to the oxidation of Rh to Rh oxide. Rh is a unique metal, with regard to the fact that no oxidized states are soluble over the whole pH and voltage region, as shown in figure 4.3a. As a result, this peak includes basically no dissolution, which is different from a typical active-passive transition peak: current increases exponentially with increasing potential after dissolution activation. A decrease takes over the increase as the passivation dominates the surface with oxide films. Based on the polarization curve of pure Cu displayed in figure 4.2b and the thermodynamic equilibrium potential of Cu oxidation in the Pourbaix diagram in figure 4.3b, the current increase starting from 0.3 V is associated with the activation of Cu dissolution. The explanation is supported by the evolution of nanoporous Rh in the left-wing of the second peak[135]. The active current in the second peak decreases with Rh concentration, which implies that the addition of Rh enhances the corrosion resistance of the alloy. No active dissolution is observed for Cu-22 at.% Rh.

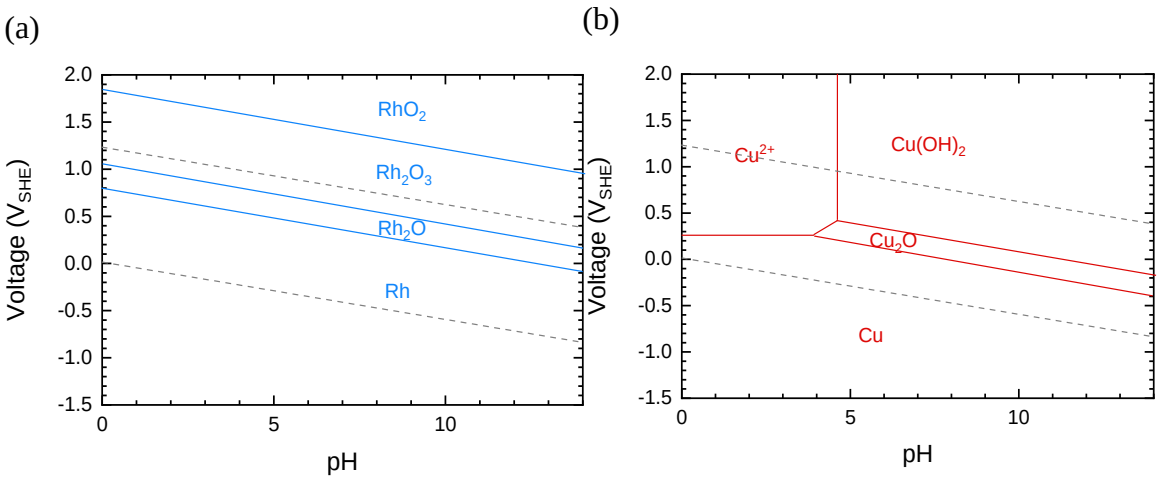

Figure 4.3. Pourbaix diagram of (a) Rh and (b) Cu in aqueous solution[19].

An apparent difference in the transpassive dissolution regime is identified between the Cu-Rh and the Fe-Cr alloy systems: the take-off voltage for the transpassive region varies with the compositions in Cu-Rh alloys; while it maintains constant for Fe-Cr alloys of various contents. The rapid current increase following passivation is usually caused by transpassive dissolution or water decomposition. But it is apparently not the case for Cu-Rh alloys. As the Pourbaix diagram shown in figure 4.3a, despite a high positive bias, Rh oxides maintain stability instead of being dissolved as soluble species in an aqueous solution, which is quite different from many metals like Cr, Fe, Ni. The "transpassive dissolution" current of pure Rh at a voltage above 1.4 V consists mostly of oxygen evolution rather than the transpassive dissolution of Rh. Even though both Cu metal and Cu^{2+} have been proved to be theoretically effective catalysts for reducing overpotentials of water oxidation[136], the current increase of Cu-9 at.% Rh around 0.8 V is unlikely to come from oxygen evolution since this potential is still below the thermodynamic value in strong acid. On the other hand, it has been reported that Cu could not form passive films in strong acid and the passivated surface developed in the right-wing of the second peak include no Cu oxide[136]. As a result, the current decrease in the second peak does not come from Cu passivation.

We currently do not understand the exact mechanism behind the shifts in the onset of "transpassive dissolution" potential by the addition of Rh as well as the current decrease in the second peak. A possible explanation is that the competition between Rh oxidation and Cu dissolution varies with the applied potential, leading to the current decrease in second passivation and the increase in "transpassivation". Compared with Rh passivating the surface with sluggish kinetics, Cu dissolves at significantly higher rates.

When the Rh passivation dominates, a passive state is achieved. The increased voltage further accelerating Cu dissolution will destroy the passivity, creating the as-seen "transpassive" dissolution. If so, the "transpassive" behavior indeed relies on the alloy composition.

4.3.2 2D to 3D transition behaviors in Cu-Rh alloys

Based on both the Pourbaix diagram and analysis on LSV, Rh is reasoned to passivate at the first peak. As potential continues to increase, sequential oxidations may follow, but the passive state maintains. As a result, the state of primary passivation that Cu is actively dissolved and Rh forms protective oxides is achieved once the increasing potential activates Cu dissolution around 0.3 V. Several voltages above 0.3 V were investigated with chronoamperometry. We found at the left shoulder of the second peak, even for alloys of high Rh content like 18 at.%, the current would slowly increase after the initial decay for tens of seconds, which is believed to result from the formation of nanoporous Rh oxide. The evolution of nanoporous Cr has never been observed in either Fe-Cr or Ni-Cr alloys.

The potentials around the peak are selected to suppress the formation of nanoporous structures. As shown in figure 4.4, the current density at 0.64 V is collected for Cu-Rh alloys with different compositions and pure Cu. A significant decrease in the current density is observed around 7 at.% Rh. Similar to the conversion for Ni-Cr alloys, the number of dissolved monolayers, h, is calculated on the primary FCC {111} surface through equation 4.1:

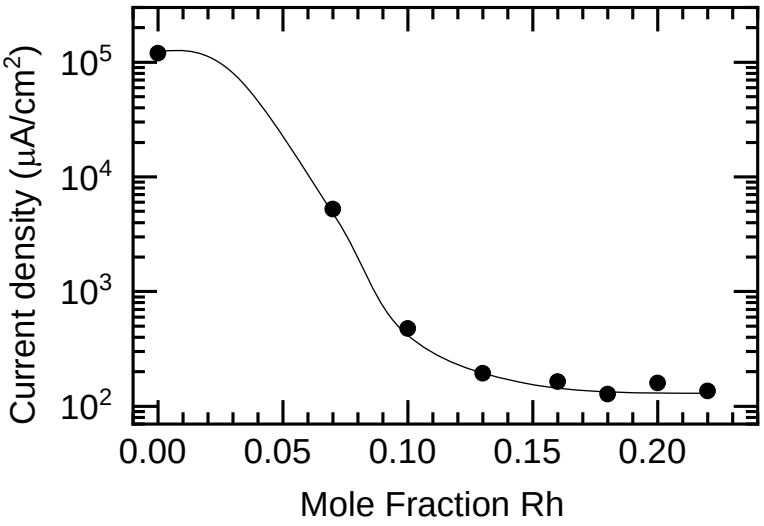

Figure 4.4. Current density transition behavior at 0.64 V over Rh concentration. Collected from the LSV curves in figure 4.2a.

$$number\ of\ layers\ dissolved = \frac{\int_0^t I\ dt}{A} \Big/ \frac{4*(3*C+2*(1-C))*q}{\sqrt{3}*a_{Cu}^2}, \qquad (4.1)$$

where A is exposed surface area, I is the magnitude of measured current, C is the mole fraction of Rh, q is the elementary charge, and a_{Cu} is the lattice parameter of FCC Cu. Rh is assumed to end with Rh_2O_3, and Cu is oxidized to Cu^{2+}. The lattice parameter is assumed to be fixed with Rh at. %.

For FCC Cu-Rh alloys (a_0= 3.60 Å), the distance between 3rd NN is noticeably larger (0.28 Å) than the length of -Rh-O-Rh-. When angling the -Rh-O-Rh- bonds and making a triangle with the 2nd NN distance as the third side, the angle between -O-Rh-O- would be too small with a value of 51º. As a result, the critical threshold for passivation is expected to lie in between corresponding interactions including up to 3rd NN (p_c {1,2,3}) and 2nd NN (p_c {1,2}), which is 6.1 % and 13.6 %, respectively[55]. Figure 4.5a shows the fitting of chronoamperometry results at 0.64 V, a 3D percolation threshold, p_c^{3D}, of

8.6 at.% was obtained, in good agreement with the critical value observed under this potential in figure 4.4. Fitting in figure 4.5b is based on the combined results from two different voltages, where current decay maintains a fixed slope, is found for each composition at a voltage lower than 0.64 V. Alloys with Rh concentration of 13 at.% and 16 at.% passivated at 0.54 V, while alloys of 18 at.%, 20 at.%, and 22 at.% passivated at 0.44 V. The fitted 3D percolation threshold ends up with 12.4 at.%, which is closed to $p_c^{3D}\{1,2,3\}$ (13.6%) of FCC lattice.

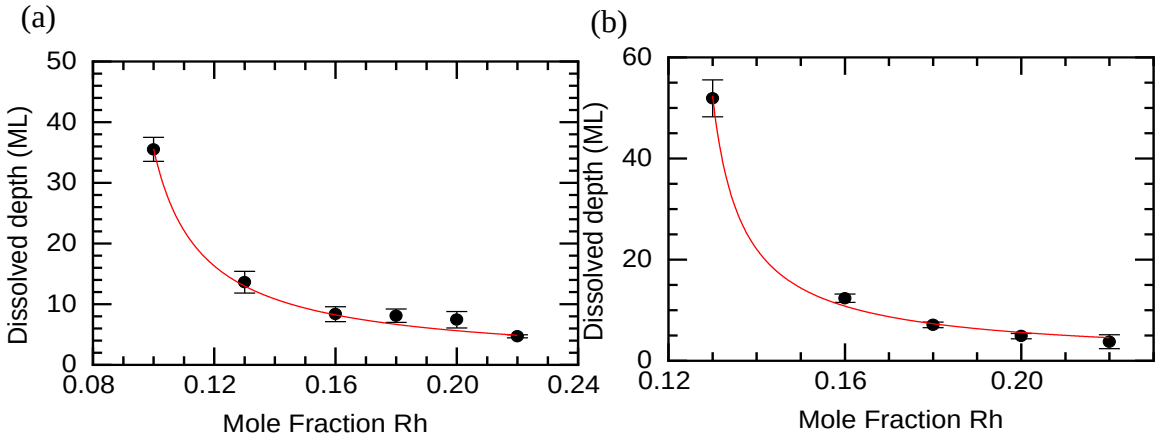

Figure 4.5. Equation for 2D-2D cross-over effect is fitted with the passivation behavior of Cu-Rh alloys with polarization under (a) 0.64 V and (b) 0.54 V and 0.44 V for 400 s. The number of dissolved layers is plotted as a function of bulk Rh composition. The red curves correspond to the fitting results with the equation of $p_c(h) = p_c + c\,h^{-1/\nu}$ with v=0.878 used for the 3D case. The fitted value of p_c^{3D} is 0.086 and 0.124, respectively.

Ideally, homogeneous alloy where atoms are randomly uniformly distributed in the matrix atoms, instead of segregation into two distinct phases. However, due to different binding energy between atoms, $E_{Cu\text{-}Cu}$, $E_{Rh\text{-}Rh}$, and $E_{Cu\text{-}Rh}$, the atomic distribution may deviate from random solutions and forms ordered or clustered configurations, which could easily lead to a discrepancy of experimental results from the theoretical predictions.

CHAPTER 5

CONCLUSIONS & FUTURE WORKS

5.1 Examination of the percolation model

The initial stage of the passivation process, the primary passivation, is investigated with experimental and simulation validation of a quantitative model, the percolation model, in several different binary alloy systems. The basic idea of the model is that the geometric connectiveness of the passivating element in the parent alloys determines the development of the protective thin film through a primary passivation process, thus the corrosion resistance of the alloy. Considering a passivating element, such as Cr, Rh studied here, the bond length of the protective oxide sets the maximum spanning length of the percolation, thus the minimum concentration value for 2D surface percolation. A corroded and roughened surface relaxes the percolation threshold to a value no less than the 3D percolation threshold. The relaxation degree is determined by the dissolved monolayers or thickness of the passive film. This theoretical film thickness transition over the percolation threshold of the film was validated in three binary alloy systems, Fe-Cr, Ni-Cr, and Cu-Rh. It turns out that the percolation model successfully predicts the composition-dependent passivation behaviors of all these alloys.

On the other hand, we found that the corrosion behaviors of the Fe-Cr alloy system changed when the atomic configuration was disturbed in a way that clustering enhances corrosion resistance while ordering delays passivation. The experimental observation agrees well with the theoretical simulations developed on the percolation model. Our results proved the atomic distribution as a promising candidate “knob” to tune the corrosion resistance at fixed composition.

Other factors that could impact the evolution of the passive films, including the pH of the electrolyte and the potential applied, were also addressed by the relative passivation contribution from constituent elements within the context of the percolation model.

5.2 Application in alloy design

There is an increasing interest in the material science community with respect to the design of multi-principal element alloys for improved properties, while design criteria for enhanced corrosion performance have not been found. Figure 5.1 is constructed to summarize how the percolation model could be applied to guide alloy engineers to design alloy compositions and atomic configurations for corrosion protection.

The mole fraction of the passivating element for passivating the alloy with fixed h is plotted against the 3D percolation threshold with spanning distance defined by comparison between -M-O-M- bond length and lattice parameters of the alloy, based on the theoretical equation, $p_c(h) = p_c + c * h^{-1/\nu}$. (c is a constant of order unity, and here is 1). The thickness of the passive film here is used to define the passivation quality of an alloy system. A fixed dissolved monolayer for passivation, h, indicates a passivity of a certain degree. The solid yellow line shows the result for h = 10 ML, other values of h will shift the line up or down. The dashed black line holds the bottom of passivation, below which passivation can never be achieved, while a lower h needs higher [M] and yields more excellent passive behavior.

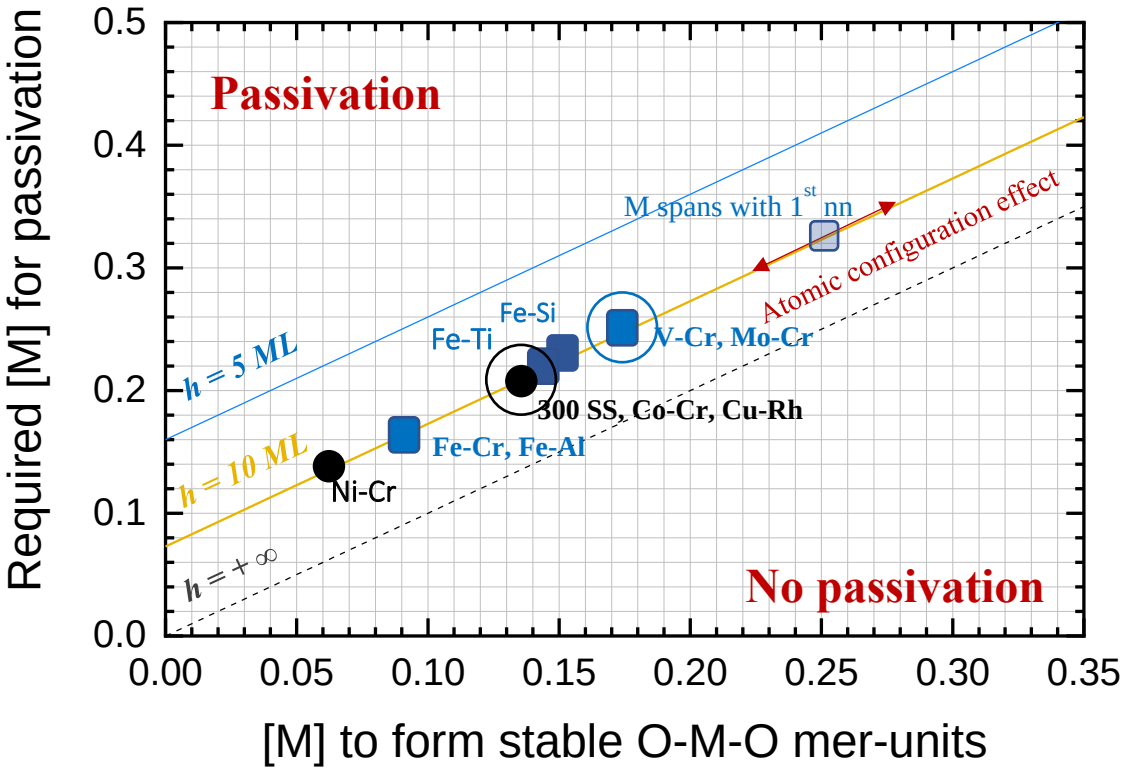

Figure 5.1. Summarized figures for the percolation model applied in alloy design. The x-axis describes the alloy system with the 3D percolation threshold for the passivating element form stable O-M-O unit of passive oxide, which is determined by comparing O-M bond length and the 1st, 2nd, 3rd nn distance of the matrix lattice. Y-axis defines the [M] required to achieve passivation with certain dissolved ML of supporting elements. Some typical FCC(BCC) alloys are populated with black (blue) points. The impact of ordering is addressed with an example of an alloy system, in which O-M-O bond spans with the distance of 1st nn in BCC lattice.

Our experimental results of Fe-Cr, Ni-Cr, and Cu-Rh together with the results of Cr-Mo, Cr-V, Co-Cr, Fe-Ti, Fe-Si, Fe-Al, and 300 series stainless steels derived from literature are populated on the figure by the comparison between passivating oxide bond length and alloy lattice parameter. Most solid solutions on thermal equilibrium do not exhibit perfect randomness. Instead, the interactions between the component atoms of an alloy system always result in some degree of clustering or ordering. The effect of atomic

configuration on passivation is addressed in the figure with red arrows changing passivation requirements. Ordering or clustering could be used to tune the corrosion resistance of alloys, providing a design strategy for an alloy system with specific compositions.

5.3 Future work

For future work, a broader application of the percolation model to other binary alloy systems is aimed. We here identified percolation thresholds of ordered alloy by MC-RNG methods, and compared it with experimental results obtained for Fe-Cr alloys, of which the ordering parameters have been predicted computationally and reported experimentally. When examining the percolation model in other systems, the comparison could also be viable when the ordering parameters are directly measured using scattering techniques or EXAFS.

REFERENCES

1. Monnartz, P. http://www.calphad.com/nickel-chromium.html.

2. Schmuki, P. From Bacon to barriers: a review on the passivity of metals and alloys. *Journal of Solid State Electrochemistry* 2002, *6*, 145–164.

3. Frankenthal, R.P.; Pickering, H.W. On the mechanism of localized corrosion of iron and stainless steel - II. morphological studies. *J. Electrochem. Soc.* 1972, *119*, 1304–1310.

4. Marcus, P.; Olefjord, I. Characterization of the passive films on FeCr and FeCrMo alloys. *Surface and interface analysis* 1988, *11*, 569–576.

5. Olefjord, I.; Clayton, C.R. Surface composition of stainless steel during active dissolution and passivation. *ISIJ International* 1991, *31*, 134–141.

6. Marcus, P.; Grimal, J.M. The anodic dissolution and passivation of NiCrFe alloys studied by ESCA. *Corrosion Science* 1992, *33*, 805–814.

7. Foley, C.L.; Kruger, J.; Bechtoldt, C.J. Electron diffraction studies of active, passive, and transpassive oxide films formed on iron. *J. Electrochem. Soc.* 1967, *114*, 994.

8. Oblonsky, L.J.; Davenport, A.J.; Ryan, M.P.; Isaacs, H.S.; Newman, R.C. In situ X-ray Absorption Near Edge Structure study of the potential dependence of the formation of the passive film on iron in borate buffer. *J. Electrochem. Soc.* 1997, *144*, 2398–2404.

9. Ryan, M.P. An STM study of the passive film formed on iron in borate buffer solution. *J. Electrochem. Soc.* 1995, *142*, L177.

10. Kong, D.-S.; Chen, S.-H.; Wan, L.-J.; Han, M.-J. The preparation and in situ Scanning Tunneling Microscopy study of Fe(110) surface. *Langmuir* 2003, *19*, 1954–1957.

11. Davenport, A.J.; Oblonsky, L.J.; Ryan, M.P.; Toney, M.F. The structure of the passive film that forms on iron in aqueous environments. *J. Electrochem. Soc.* 2000, *147*, 2162.

13. Maurice, V.; Talah, H.; Marcus, P. A scanning tunneling microscopy study of the structure of thin oxide films grown on Ni(111) single crystal surfaces by anodic polarization in acid electrolyte. *Surface Science* 1994, *304*, 98–108.

14. Suzuki, T.; Yamada, T.; Itaya, K. In situ electrochemical Scanning Tunneling Microscopy of Ni(111), Ni(100), and sulfur-modified Ni(100) in acidic solution. *The Journal of Physical Chemistry* 1996, *100*, 8954–8961.

15. Magnussen, O.M.; Scherer, J.; Ocko, B.M.; Behm, R.J. In situ X-ray scattering study of the passive film on Ni(111) in sulfuric acid solution. *The Journal of Physical Chemistry B* 2000, *104*, 1222–1226.

16. Zuili, D.; Maurice, V.; Marcus, P. Surface structure of nickel in acid solution studied by in situ Scanning Tunneling Microscopy. *Journal of The Electrochemical Society* 2000, *147*, 1393.

17. Macdougall, B.; Mitchell, D.F.; Graham, M.J. The use of electrochemical and surface-analytical techniques to characterize passive oxide films on nickel. *CORROSION* 1982, *38*, 85–91.

18. Maurice, V. XPS and STM investigation of the passive film formed on Cr(110) single-crystal surfaces. *Journal of The Electrochemical Society* 1994, *141*, 3016.

19. POURBAIX, M. Atlas of Electrochemical Equilibria in Aqueous Solution. *NACE* 1974, *307*.

20. Huang, L.-F.; Rondinelli, J.M. Reliable electrochemical phase diagrams of magnetic transition metals and related compounds from high-throughput ab initio calculations. *npj Materials Degradation* 2019, *3*.

21. Ryan, M.P.; Newman, R.C.; Thompson, G.E. A Scanning Tunneling Microscopy study of structure and structural relaxation in passive oxide films on Fe-Cr alloys. *Philosophical Magazine B* 1994, *70*, 241–251.

22. Ryan, M.P. Atomically resolved STM of oxide film structures on Fe-Cr alloys during passivation in sulfuric acid solution. *Journal of The Electrochemical Society* 1994, *141*, L164.

23. Keddam, M.; Mattos, O.R.; Takenouti, H. Mechanism of anodic dissolution of iron-chromium alloys investigated by electrode impedances—I. Experimental results and reaction model. *Electrochimica Acta* 1986, *31*, 1147–1158.

24. Uhlig, H.H.; Woodside, G.E. Anodic polarization of passive and non-passive FeCr Alloys. *The Journal of Physical Chemistry* 1953, *57*, 280–283.

25. King, P.F.; Uhlig, H.H. Passivity in the FeCr binary alloys. *The Journal of Physical Chemistry* 1959, *63*, 2026–2032.

26. Asami, K.; Hashimoto, K.; Shimodaira, S. Cr enrichment of the passive film on the surface of FeCr shows remarkable increases around 13 at.%. *Corrosion Science 18*, 151.

27. Uhlig, H.H.; Lord, S.S. Amount of oxygen on the surface of passive stainless steel. *Journal of The Electrochemical Society* 1953, *100*, 216.

28. Uhlig, H.H. The adsorption theory of passivity and the Flade potential. *Berichte der Bunsengesellschaft für physikalische Chemie* 1958, *62*, 626–632.

29. Bond, A.P.; Uhlig, H.H. Corrosion behavior and passivity of Nickel-Chromium and Cobalt-Chromium alloys. *Journal of The Electrochemical Society* 1960, *107*, 488.

30. Mansfeld, F.; Uhlig, H.H. Effect of electron donor and acceptor elements on passivity of Copper-Nickel alloys. *J. Electrochem. Soc.* 1970, *117*, 427.

31. Uhlig, H.H. Electron configuration in alloys and passivity. 1958, 8.

32. McCafferty, E. Graph theory and the passivity of Iron-Chromium binary alloys. *Electrochem. Solid-State Lett.* 1999, *3*, 28.

33. McCafferty, E. Oxide networks, graph theory, and the passivity of binary alloys. *Corrosion Science* 2002, *44*, 1393–1409.

34. Oblonsky, L.J.; Ryan, M.P.; Isaacs, H.S. In situ determination of the composition of surface films formed on Fe-Cr alloys. *J. Electrochem. Soc.* 1998, *145*.

35. McBee, C.L.; Kruger, J. Nature of passive films on Iron-Chromium alloys. *Electrochimica Acta* 1972, *17*, 1337–1341.

36. Sieradzki, K. A percolation model for passivation in stainless steels. *J. Electrochem. Soc.* 1986, *133*, 1979.

37. Newman, R.C.; Foong Tuck Meng; Sieradzki, K. Validation of a percolation model for passivation of Fe-Cr alloys: current efficiency in the incompletely passivated state. *Corrosion Science* 1988, *28*, 523–527.

38. Fujimoto, S.; Newman, R.C.; Smith, G.S.; Kaye, S.P.; Kheyrandish, H.; Colligon, J.S. Passivation thresholds in iron-chromium alloys prepared by ion-beam sputtering. *Corrosion Science* 1993, *35*, 51–55.

39. Qian, S. Validation of a percolation model for passivation of Fe-Cr Alloys: two-dimensional computer simulations. *J. Electrochem. Soc.* 1990, *137*, 435.

40. Qian, S.; Newman, R.C.; Cottis, R.A.; Sieradzki, K. Computer simulation of alloy passivation and activation. *Corrosion Science* 1990, *31*, 621–626.

41. Ryan, M.P.; Newman, R.C.; Thompson, G.E. A scanning tunneling microscopy study of structure and structural relaxation in passive oxide films on Fe-Cr alloys. *Philosophical Magazine B* 1994, *70*, 241–251.

42. Davenport, A.J.; Ryan, M.P.; Simmonds, M.C.; Ernst, P.; Newman, R.C.; Sutton, S.R.; Colligon, J.S. In situ synchrotron X-ray microprobe studies of passivation thresholds in Fe-Cr alloys. *Journal of The Electrochemical Society* 2001, *148*, B217.

43. Holliday, J.E.; Frankenthal, R.P. Characterization of Passivating Films on Fe - Cr Alloys by Soft X-Ray Spectroscopy. *J. Electrochem. Soc.* 1972, *119*, 1190–1192, doi:10.1149/1.2404440.

44. Leygraf, C.; Hultqvist, G.; Olefjord, I.; Knyazheva, V.M.; Plaskeyev, A.V.; Kolotyrkin, Y.M. Selective dissolution and surface enrichment of alloy components of passivated Fe18Cr and Fe18Cr3Mo single crystals. 34.

45. Keller, P.; Strehblow, H.-H. XPS investigations of electrochemically formed passive layers on Fe/Cr-alloys in 0.5 M H2SO4. *Corrosion Science* 2004, *46*, 1939–1952.

46. Haupt, S.; Strehblow, H.-H. A combined surface analytical and electrochemical study of the formation of passive layers on FeCr alloys in 0.5 M H2SO4. *Corrosion Science* 1995, *37*, 43–54.

47. Asami, K.; Hashimoto, K.; Shimodaira, S. An XPS study of the passivity of a series of iron-chromium alloys in sulphuric acid. *Corrosion Science* 1978, *18*, 151–160.

48. Castle, J.E.; Qiu, J.H. A co-ordinated study of the passivation of alloy steels by plasma source mass spectrometry and x-ray photoelectron spectroscopy—1. characterization of the passive film. *Corrosion Science* 1989, *29*, 591–603, doi:10.1016/0010-938X(89)90010-3.

49. Kerkar, M.; Robinson, J.; Forty, A.J. In situ structural studies of the passive film on iron and iron/chromium alloys using X-ray absorption spectroscopy. *Faraday Discussions of the Chemical Society* 1990, *89*, 31.

50. Frankenthal, R.P. On the Passivity of Iron-Chromium Alloys: I . Reversible Primary Passivation and Secondary Film Formation. *J. Electrochem. Soc.* 1967, *114*, 542, doi:10.1149/1.2426646.

51. Frankenthal, R.P. On the Passivity of Iron-Chromium Alloys: II . The Activation Potential. *J. Electrochem. Soc.* 1969, *116*, 580, doi:10.1149/1.2411968.

52. Frankenthal, R.P. On the Passivity of Iron-Chromium Alloys: III . Effect of Potential. *J. Electrochem. Soc.* 1969, *116*, 1646, doi:10.1149/1.2411650.

53. Asami, K. An XPS study of the passivity of a series of Iron-Chromium alloys in sufuric acids. 10.

54. Programming Assignment 1: Percolation Available online: https://coursera.cs.princeton.edu/algs4/assignments/percolation/specification.php (accessed on Sep 17, 2020).

55. Shante, V.K.S.; Kirkpatrick, S. An introduction to percolation theory. *Advances in Physics* 1971, *20*, 325–357, doi:10.1080/00018737100101261.

56. Sotta, P.; Long, D. The crossover from 2D to 3D percolation: Theory and numerical simulations. *The European Physical Journal E* 2003, *11*, 375–388.

57. Mitrovic-Scepanovic, V.; MacDougall, B.; Graham, M.J. Nature of passive films on Fe26Cr alloy. *Corrosion Science* 1984, *24*, 479–490.

58. Danoix, F.; Auger, P. Atom Probe Studies of the Fe–Cr System and Stainless Steels Aged at Intermediate Temperature: A Review. *Materials Characterization* 2000, *44*, 177–201.

59. Heine, B.; B. Heine Untersuchungen an Eisen und Chrom sowie deren Legierungen zur Bildung und Zusammensetzung der Passivschichten auf diesen Werkstoffen. 2015, doi:10.13140/2.1.3792.9764.

60. Kaesche, H. Die Spannungsrißkorrosion. In *Die Korrosion der Metalle: Physikalisch-chemische Prinzipien und aktuelle Probleme*; Kaesche, H., Ed.; Springer: Berlin, Heidelberg, 1979; pp. 300–363 ISBN 978-3-662-11502-2.

61. Beck, T.R. Formation of salt films during passivation of iron. *J. Electrochem. Soc.* 1982, *129*, 2412.

62. Schmuki, P. Passivity of iron in alkaline solutions studied by in situ XANES and a laser reflection technique. *J. Electrochem. Soc.* 1999, *146*, 2097.

63. Schmuki, P. In situ X-ray Absorption Near-Edge Spectroscopic study of the cathodic reduction of artificial iron oxide passive films. *J. Electrochem. Soc.* 1996, *143*, 574.

64. Epelboin, I.; Keddam, M.; Mattos, O.R.; Takenouti, H. The dissolution and passivation of Fe and FeCr alloys in acidified sulphate medium: Influences of pH and Cr content. *Corrosion Science* 1979, *19*, 1105–1112.

65. Iron-Chromium (Fe-Cr) Phase Diagram Available online: http://www.calphad.com/iron-chromium.html (accessed on Sep 17, 2020).

66. Novy, S.; Pareige, P.; Pareige, C. Atomic scale analysis and phase separation understanding in a thermally aged Fe–20at.%Cr alloy. *Journal of Nuclear Materials* 2009, *384*, 96–102.

67. Kresse, G.; Furthmüller, J. Efficient iterative schemes for *ab initio* total-energy calculations using a plane-wave basis set. *Physical Review B* 1996, *54*, 11169–11186.

68. Perdew, J.P.; Burke, K.; Ernzerhof, M. Generalized Gradient Approximation Made Simple. *Physical Review Letters* 1996, *77*, 3865–3868.

69. Blöchl, P.E. Projector augmented-wave method. *Physical Review B* 1994, *50*, 17953–17979.

70. Monkhorst, H.J.; Pack, J.D. Special points for Brillouin-zone integrations. *Physical Review B* 1976, *13*, 5188–5192.

71. Kittel, C. *Introduction to solid state physics*; 7th ed.; Wiley: New York, 1996;

72. Dobbelaar, J.A.L.; Herman, E.C.M.; de Wit, J.H.W. The corrosion behaviour of iron-chromium alloys in 0.5 M sulphuric acid. *Corrosion Science* 1992, *33*, 765–778.

73. Heine, B.; B. Heine Untersuchungen an Eisen und Chrom sowie deren Legierungen zur Bildung und Zusammensetzung der Passivschichten auf diesen Werkstoffen. *Universität Stuttgart* 1988.

74. El-Basiouny, M.S.; Haruyama, S. The polarization behaviour of FeCr alloys in acidic sulphate solutions in the active region. *Corrosion Science* 1976, *16*, 529–540.

75. Schmuki, P. Transpassive dissolution of Cr and sputter-deposited Cr oxides studied by in situ X-ray Near-Edge Spectroscopy. *J. Electrochem. Soc.* 1996, *143*, 3997.

76. Hamm, D.; Ogle, K.; Olsson, C.O.A.; Weber, S.; Landolt, D. Passivation of Fe–Cr alloys studied with ICP-AES and EQCM. *Corrosion Science* 2002, *44*, 1443–1456.

77. Hara, N. The study of the passivation films on Fe-Cr alloys by modulation spectroscopy. *J. Electrochem. Soc.* 1979, *126*, 1328.

78. Bligaard, T.; Nørskov, J.K. Ligand effects in heterogeneous catalysis and electrochemistry. *Electrochimica Acta* 2007, *52*, 5512–5516.

79. Ma, Y.; Balbuena, P.B. Surface properties and dissolution trends of Pt_3M alloys in the presence of adsorbates. *The Journal of Physical Chemistry C* 2008, *112*, 14520–14528.

80. Fu, C.; Liu, C.; Li, T.; Zhang, X.; Wang, F.; Yang, J.; Jiang, Y.; Cui, P.; Li, H. DFT calculations: A powerful tool for better understanding of electrocatalytic oxygen reduction reactions on Pt-based metallic catalysts. *Computational Materials Science* 2019, *170*, 109202.

81. Diawara, B.; Legrand, M.; Legendre, J.-J.; Marcus, P. Use of quantum chemistry results in 3D modeling of corrosion of Iron-Chromium alloys. *Journal of The Electrochemical Society* 2004, *151*, B172.

82. Diawara, B.; Beh, Y.-A.; Marcus, P. Nucleation and growth of oxide layers on stainless steels (FeCr) Using a virtual oxide layer model. *The Journal of Physical Chemistry C* 2010, *114*, 19299–19307.

83. Samin, A.J.; Andersson, D.A.; Holby, E.F.; Uberuaga, B.P. First-principles localized cluster expansion study of the kinetics of hydrogen diffusion in homogeneous and heterogeneous Fe-Cr alloys. *Phys. Rev. B* 2019, *99*, 014110.

84. Bruzzoni, P.; Pasianot, R.C. A DFT study of H solubility and diffusion in the Fe-Cr system. *Computational Materials Science* 2018, *154*, 243–250.

85. Bonny, G.; Terentyev, D.; Malerba, L. New Contribution to the Thermodynamics of Fe-Cr Alloys as Base for Ferritic Steels. *J. Phase Equilib. Diffus.* 2010, *31*, 439–444.

86. Bhattacharjee, S.; Waghmare, U.V.; Lee, S.-C. An improved d-band model of the catalytic activity of magnetic transition metal surfaces. *Scientific Reports* 2016, *6*.

87. Samin, A.J.; Taylor, C.D. First-principles investigation of surface properties and adsorption of oxygen on Ni-22Cr and the role of molybdenum. *Corrosion Science* 2018, *134*, 103–111.

88. Shante, V.K.S.; Kirkpatrick, S. An introduction to percolation theory. *Advances in Physics* 1971, *20*, 325–357.

89. Legrand, M.; Diawara, B.; Legendre, J.-J.; Marcus, P. Three-dimensional modelling of selective dissolution and passivation of iron–chromium alloys. *Corrosion Science* 2002, *44*, 773–790.

90. Olsson, P.; Abrikosov, I.A.; Wallenius, J. Electronic origin of the anomalous stability of Fe-rich BCC Fe-Cr alloys. *Physical Review B* 2006, *73*.

91. Korzhavyi, P.A.; Ruban, A.V.; Odqvist, J.; Nilsson, J.-O.; Johansson, B. Electronic structure and effective chemical and magnetic exchange interactions in bcc Fe-Cr alloys. *Physical Review B* 2009, *79*.

92. Klaver, T.P.C.; Drautz, R.; Finnis, M.W. Magnetism and thermodynamics of defect-free Fe-Cr alloys. *Physical Review B* 2006, *74*.

93. Froideval, A.; Iglesias, R.; Samaras, M.; Schuppler, S.; Nagel, P.; Grolimund, D.; Victoria, M.; Hoffelner, W. Magnetic and Structural Properties of FeCr Alloys. *Physical Review Letters* 2007, *99*.

94. Bonny, G.; Terentyev, D.; Malerba, L. On the α–α′ miscibility gap of FeCr alloys. *Scripta Materialia* 2008, *59*, 1193–1196.

95. Rahaman, M.; Johansson, B.; Ruban, A.V. First-principles study of atomic ordering in FCC Ni-Cr alloys. *Physical Review B* 2014, *89*.

96. Levesque, M.; Martínez, E.; Fu, C.-C.; Nastar, M.; Soisson, F. Simple concentration-dependent pair interaction model for large-scale simulations of Fe-Cr alloys. *Physical Review B* 2011, *84*.

97. Mirebeau, I.; Parette, G. Neutron study of the short range order inversion in FeCr alloys. *Phys. Rev. B* 2010, *82*, 104203.

98. Dubiel, S.M.; Cieslak, J. Short-range order in iron-rich FeCr alloys as revealed by Mössbauer spectroscopy. *Physical Review B* 2011, *83*.

99. Dubiel, S.M.; Cieślak, J. Effect of thermal treatment on the short-range order in FeCr alloys. *Materials Letters* 2013, *107*, 86–89.

100. Dubiel, S.M.; Cieślak, J.; Żukrowski, J. Distribution of Cr atoms in the surface zone of Fe-rich FeCr alloys quenched into various media: Mössbauer spectroscopic study. *Applied Surface Science* 2015, *359*, 526–532.

101. Reynolds, P.J.; Stanley, H.E.; Klein, W. Large-cell Monte Carlo renormalization group for percolation. *Phys. Rev. B* 1980, *21*, 1223–1245.

102. Artymowicz, D.M.; Erlebacher, J.; Newman, R.C. Relationship between the parting limit for de-alloying and a particular geometric high-density site percolation threshold. *Philosophical Magazine* 2009, *89*, 1663–1693.

103. Bartlett, J.H.; Stephenson, L. Anodic Behavior of Iron in H2SO4. *J. Electrochem. Soc.* 1952, *99*, 9.

104. Podestá, J.J.; Piatti, R.C.V.; Arvia, A.J. Comparative Electron Microscopy (SEM) examination of Fe, Au, and Zn electrode surfaces polarized in different regions of potentiostatic E/I behavior. *CORROSION* 1982, *38*, 599–603.

105. Teschke, O.; Soares, D.M.; Galembeck, F.; Tenan, M.A. Capillary and electrochemical oscillations in a corroding electrode system. *Langmuir* 1985, *1*, 713–718.

106. Podestá, J.J. The potentiostatic current oscillations at iron/sulfuric acid solution interfaces. *Journal of The Electrochemical Society* 1979, *126*, 1363.

107. Bond, A.P.; Lizlovs, E.A. Intergranular corrosion of ferritic stainless steels. *Journal of The Electrochemical Society* 1969, *116*, 1305.

108. Frankenthal, R.P.; Pickering, H.W. Intergranular corrosion of a ferritic stainless steel. *Journal of The Electrochemical Society* 1973, *120*, 23.

109. Beauchamp, R.L. Polarization Characteristics of High-Purity Iron-Rich Iron - Chromium - Nickel Alloys in Sulfuric Acid Solutions. Ph.D.Degree, The Ohio State University, 1967.

110. Bond, A.P.; Uhlig, H.H. Corrosion Behavior and Passivity of Nickel-Chromium and Cobalt-Chromium Alloys. *J. Electrochem. Soc.* 1960, *107*, 488, doi:10.1149/1.2427729.

111. Oblonsky, L.J.; Ryan, M.P. In situ X-ray Absorption Near-Edge Structure study of the active and transpassive dissolution of passive films on Ni and Ni-Cr alloys in 0.1 M H2SO4. *Journal of The Electrochemical Society* 2001, *148*, B405.

112. Luo, L.; Zou, L.; Schreiber, D.K.; Baer, D.R.; Bruemmer, S.M.; Zhou, G.; Wang, C.-M. In-situ transmission electron microscopy study of surface oxidation for Ni–10Cr and Ni–20Cr alloys. *Scripta Materialia* 2016, *114*, 129–132.

113. Jabs, T.; Borthen, P.; Strehblow, H.-H. X-ray Photoelectron Spectroscopic examinations of electrochemically formed passive layers on Ni-Cr alloys. *J. Electrochem. Soc.* 1997, *144*, 1231.

114. Jang, H.; Kwon, H. Effects of Cr on the structure of the passive films on Ni-(15, 30)Cr alloys. *ECS Transactions* 2019, *3*, 1–11.

115. Hall, D.S.; Bock, C.; MacDougall, B.R. The electrochemistry of metallic nickel: oxides, hydroxides, hydrides and alkaline hydrogen evolution. *Journal of The Electrochemical Society* 2013, *160*, F235–F243.

116. Das, N.K.; Shoji, T. A density functional study of atomic oxygen and water molecule adsorption on Ni(111) and chromium-substituted Ni(111) surfaces. *Applied Surface Science* 2011, *258*, 442–447.

117. Lutton, K.; Gusieva, K.; Ott, N.; Birbilis, N.; Scully, J.R. Understanding multi-element alloy passivation in acidic solutions using operando methods. *Electrochemistry Communications* 2017, *80*, 44–47.

118. Bernardini, M.; Comisso, N.; Davolio, G.; Mengoli, G. Formation of nickel hydrides by hydrogen evolution in alkaline media. *Journal of Electroanalytical Chemistry* 1998, *442*, 125–135.

119. Hall, D.S.; Bock, C.; MacDougall, B.R. The electrochemistry of metallic nickel: oxides, hydroxides, hydrides and alkaline hydrogen evolution. *Journal of The Electrochemical Society* 2013, *160*, F235–F243.

120. D'Alkaine, C.V.; Santanna, M.A. The passivating films on nickel in alkaline solutions I. General aspects of the Ni (II) region. *Journal of Electroanalytical Chemistry* 1998, *457*, 5–12.

121. Hall, D.S.; Lockwood, D.J.; Poirier, S.; Bock, C.; MacDougall, B.R. Applications of in situ Raman Spectroscopy for identifying nickel hydroxide materials and surface layers during chemical aging. *ACS Applied Materials & Interfaces* 2014, *6*, 3141–3149.

122. The passivation of nickel in aqueous solutions—II. An in situ investigation of the passivation of nickel using optical and electrochemical techniques - ScienceDirect.

123. Hoppe, H.-W.; Strehblow, H.-H. XPS and UPS examinations of the formation of passive layers on Ni in 1 M sodium hydroxide and 0.5 M sulphuric acid. *Surface and Interface Analysis* 1989, *14*, 121–131.

124. Nakamura, M.; Ikemiya, N.; Iwasaki, A.; Suzuki, Y.; Ito, M. Surface structures at the initial stages in passive film formation on Ni(111) electrodes in acidic electrolytes. *Journal of Electroanalytical Chemistry* 2004, *566*, 385–391.

125. MacDougall, B. The effect of cathodic treatment on nickel dissolution. *Journal of The Electrochemical Society* 1975, *122*, 383.

126. Barbosa, M.R. Comparative potentiodynamic study of nickel in still and stirred sulfuric acid-potassium sulfate solutions in the 0.4–5.7 pH range. *Journal of The Electrochemical Society* 1988, *135*, 1077.

127. Tokuda, T.; Ives, M.B. Pitting corrosion of Ni. *Corrosion Science* 1971, *11*, 297–306.

128. Vilche, J.R.; Arvía, A.J. Kinetics and mechanism of the nickel electrode—II. Acid solutions containing a high concentration of sulphate and nickel ions. *Corrosion Science* 1978, *18*, 441–463.

129. Real, S.G.; Vilche, J.R.; Arvia, A.J. The characteristics of the potentiodynamic potential/current profiles obtained with the Ni/0.5N H2SO4 interface. A contribution to the mechanism of the electrode process. *Corrosion Science* 1980, *20*, 563–586, doi:10.1016/0010-938X(80)90072-4.

130. Bernardini, M.; Comisso, N.; Davolio, G.; Mengoli, G. Formation of nickel hydrides by hydrogen evolution in alkaline media. *Journal of Electroanalytical Chemistry* 1998, *442*, 125–135.

131. Seyeux, A.; Maurice, V.; Klein, L.H.; Marcus, P. In situ scanning tunnelling microscopic study of the initial stages of growth and of the structure of the passive film on Ni(111) in 1 mM NaOH(aq). *J Solid State Electrochem* 2005, *9*, 337–346.

132. Suzuki, T.; Yamada, T.; Itaya, K. In Situ Electrochemical Scanning Tunneling Microscopy of Ni(111), Ni(100), and Sulfur-Modified Ni(100) in Acidic Solution. *The Journal of Physical Chemistry* 1996, *100*, 8954–8961.

133. Palina, N.; Sakata, O.; Kumara, L.S.R.; Song, C.; Sato, K.; Nagaoka, K.; Komatsu, T.; Kobayashi, H.; Kusada, K.; Kitagawa, H. Electronic Structure Evolution with Composition Alteration of RhxCuy Alloy Nanoparticles. *Scientific Reports* 2017, *7*.

134. Cu-Rh - Phase Diagram Available online: https://sites.google.com/site/catcalcphase/metal/cu/cu-rh?overridemobile=true.

135. Liu, F.; Jin, H.-J. Extrinsic Parting Limit for Dealloying of Cu-Rh. *J. Electrochem. Soc.* 2018, *165*, C999–C1006.

136. Du, J.; Chen, Z.; Ye, S.; Wiley, B.J.; Meyer, T.J. Copper as a Robust and Transparent Electrocatalyst for Water Oxidation. *Angew. Chem. Int. Ed.* 2015, *54*, 2073–2078.

137. McCafferty, E. Introduction to Corrosion Science, Springer, (2010), ISBN 978-1441904546.

138. Kirchheim, R., et al. The Passivity of Iron-Chromium Alloys, Corros. Sci. 29, 899–917 (1989).

139. Williams, D.E., Newman, R.C., Song, Q. & Kelly, R.G. Passivity breakdown and pitting corrosion of binary alloys, Nature, 350, 216-219 (1991).

140. Odette, R. & Zinkle, S. Structural Alloys for Nuclear Energy Applications, Elsevier, (2019). ISBN 978-0123970466.

141. Niinomi, M., Nakai, M. & Hieda, J. Development of new metallic alloys for biomedical applications, Acta Biomater, 11, 3888-3903 (2012).

142. Miracle, D.B. & Senkov, O.N. A critical review of high entropy alloys and related concepts, Acta Mater., 122, 448-511 (2017).

143. George, E.P., Raabe, D. & Ritchie, R.O. High-entropy alloys, Nat. Rev. Mater., 4, 515-534 (2019).

144. Troparevsky, M.C., Morris, J.R., Kent, P.R.C., Lupini, A.R. & Stocks, G.M. Criteria for predicting the formation of single-phase high entropy alloys, Phys. Rev. X, 011041 (2015).

145. Huang, L-F., Scully, J.R. & Rondenelli, J.M. Modeling corrosion with first principles electrochemical phase diagrams, Annu. Rev. Mater. Res., 49, 53-77 (2019).

146. Huang, L_F. & Rondenelli, J.M. Electrochemical phase diagrams of Ni from ab initio simulations: role of exchange interactions on accuracy. J. Phys. Condens. Mat., 29, 475501 (2017).

147. X. Yu et al. Nonequilibrium solute capture in passivating oxide films, Phys. Rev. Lett, 121, 145701 (2018).

148. Sherman, Q., Voorhees, P.W. & Marks, L.D. Thermodynamics of solute capture during the oxidation of multicomponent metals, Acta Mater, 181, 584-594 (2019).

149. Bastek, P.D., Newman, R.C. & Kelly, R.G. Measurement of passive film effects on scratched electrode behavior, J. Electrochem. Soc. 140, 1884–1889 (1993).

150. Shannon, R.D. Revised Effective Ionic Radii and Systematic Studies of Interatomic Distances in Halides and Chalcogenides, Acta Cryst., A 32, 751- 767 (1976).

151. Liu, M., Aiello, A., Xie, Y. & Sieradzki, K. The Effect of Short Range Order on the Passivation of Fe-Cr alloys, J. Electrochem. Soc., 165, C830 – C834 (2018).

152. Sykes, M.F. & Glen, M. Percolation processes in two dimensions: I Low-density series expansions, J. Phys. A-Math. Gen., 9, 87-95 (1976).

153. Sykes, M.F. & Glen, M. Percolation processes in three dimensions, J. Phys. A-Math Gen., 9, 1705-1712 (1976).

154. Stauffer, D. & Aharony, A. Introduction to Percolation Theory, 2nd Edition, Taylor & Francis, (1992), ISBN 0 7484 0027 3.

155. Clerc, J. P., Giraud, G., Alexander, S. & Guyon, E. Conductivity of a mixture of conducting and insulating grains: Dimensionality effects, Phys. Rev. B, 22, 2489-2494 (1980).

156. Lopes, P.P. et al. Relationships between Atomic Level Surface Structure and Stability, ACS Catal., 6, 2536–2544 (2016).

157. Liu, Y. et al. Stability Limits and Defect Dynamics in Ag Nanoparticles Probed by Bragg Coherent Diffractive Imaging, Nano Lett., 17, 1595-1601 (2017).

158. Gaskell, G. R., Introduction to the Thermodynamics of Materials, 4th Edition, Taylor & Francis, (2003), ISBN 1-56032-992-0.

APPENDIX A

HIGH LEVEL ALLOY DESIGN FOR CORROSION PROTECTION

With the advent of data mining, artificial intelligence and increased computing power for DFT based calculations, new families of alloys are being discovered at an increasing rate[142-144]. Currently, there are no criteria for determining alloy compositions that would be expected to display good passive behavior. Potential-pH diagrams, which are now constructed using DFT assume thermodynamic equilibrium, but often passive film growth is kinetically controlled; passive films can be far from equilibrium both in terms of crystal structure and composition[145-148]. In this study, we focus our attention on percolation processes that occur during the initial stage of passivation, termed primary passivation[50], which is a surface process occurring over time scales of 10 milliseconds or less[149].

Site percolation has previously been connected to the passivation behavior of Fe-Cr, Ni-Cr and stainless-steel alloys[36]. Based on the ionic radii of Cr^{3+}, O^{2-} and the BCC Fe-Cr crystal structure, it was conjectured that connected surface -Cr-O-Cr- linkages or "mer"-units could evolve for Cr atoms separated by as much as the 3rd NN distance in the Fe-Cr lattice[36,150]. Similar arguments for FCC Ni-Cr alloys indicate that Cr atoms can also be as far apart as the 3rd NN distance which is just slightly larger (0.016 nm) than the Cr atom separation in a mer-unit. The key motivation for connecting percolation phenomena to passivity has to do with the formation of spatially isolated -Cr-O-Cr-mer units. As a result of the selective dissolution of Fe or Ni that occurs during primary passivation, it was reasoned that such unconnected locally passive regions could be dissolved out and that the only way of preventing this was if these incipient oxide nuclei were continuous or percolating across the alloy surface[36,151]. The percolation thresholds for BCC and FCC random solid solutions including up to 3rd NN, here termed,

$p_c^{3D}\{1,2,3\}$, are 0.095 and 0.061 respectively[88]. Importantly, these thresholds only set lower compositional bounds for the mole fraction of Cr required for passivation. As demonstrated below, at these thresholds, in order for primary passivation to occur, Fe or Ni would have to be selectively dissolved over depths corresponding to thousands of monolayers.

It is essential to recognize that the primary passivation process occurs on a topological or roughened surface that has evolved by electrochemical metal and chemical metal-oxide dissolution. Figure 1.15 is a cartoon showing the evolution of such an alloy surface and how the initial alloy composition dictates the depth of dissolution, h, required for the formation of the primary passive film. Figure A.1 shows analogous results from KMC simulations of the passive surface that developed for a BCC Fe-17 at.% Cr alloy. As Fe is selectively dissolved, Cr enriches on the roughened surface. Metallic surface Cr atom clusters of sufficient size serve as sites for the nucleation of Cr-O-Cr-mer units and

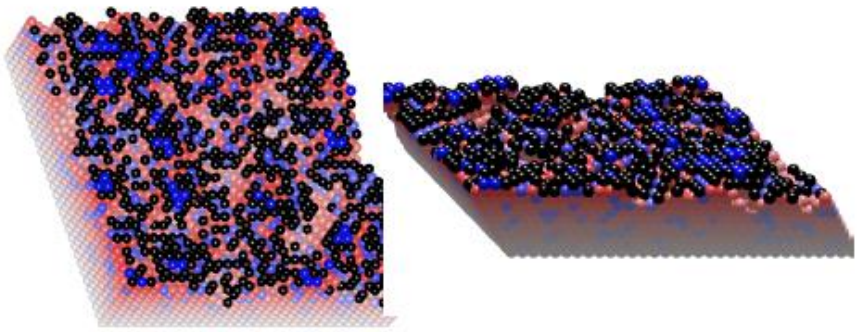

Figure A.1. Results of KMC simulations of passivation in a 17% Cr, Fe-Cr alloy in which primary passivation occurred following the dissolution of 5.4 atomic layers. This image has been topographically colored. Except for the Fe incorporated into the primary passive film (shown as black atoms), richer shades correspond to atoms in top-most layers. Violet atoms correspond to Cr and un-oxidized red atoms, not part of the primary passive film, correspond to Fe.

Fe atoms bridged or immediately adjacent to these mer-units form an incipient mixed oxide nucleus. Since the Fe atom neighborhood that surrounds small Cr clusters will attenuate the Gibbs free energy for mer-unit formation, the electrochemical potential to passivate a particularly sized Cr cluster will depend on its size. In principle this scenario is amenable to first principles-based quantum calculations, but owing to the huge number of possible cluster configurations[152,153], a complete enumeration of such alloying cluster size effects is beyond today's computing power. Nevertheless, as shown below, clear trends emerge as a function of the number of Cr atoms in very small surface clusters.

Primary passivation evolves as the system "looks" for mer-unit connectivity on the topological surface in the thickness direction by selectively dissolving Fe or Ni. As shown in Fig. A.1, this results in a reduction of the percolation threshold on the topological surface. This argument can be elucidated within the context of percolation theory. The interlayer neighbor connectivity of Cr atoms in the thickness direction is described by the percolation correlation length, ζ, which depends on the Cr atom fraction, p[56]. The correlation length diverges as we approach the threshold according to $\zeta \approx (p - p_c^{3D}\{1,2,3\})^{-\nu_{3D}}$, where ν_{3D} is a scaling exponent which has a universal value of 0.878 in 3D[56]. This correlation length defines the depth over which Cr percolates which by ansatz we take equal to h and set $p = p_c(h)$ to obtain the result, $h = [p_c(h) - p_c^{3D}\{1,2,3\}]^{-\nu_{3D}}$, where c is a constant of order unity[154]. $p_c(h)$ represents a series of percolation thresholds determined by the alloy composition on the 2D topological surface[154]. Similar 2D-3D crossover effects have been used to explain the surface electrical conductivity of metal/insulator composites[155].

Experiments, KMC simulations, DFT calculations and large cell MC-RNG methods are used to examine the predictions and assumptions of the theory. The KMC simulations treat Cr atoms that are in clusters of sufficient extent to form -Cr-O-Cr mer-units as elemental Cr in regard to their propensity for oxidation. Since the theory only involves percolation, these simulations exclude the electronic effects related to how Fe might attenuate the Cr electronic structure and so the oxidation of variously-sized Cr atom clusters.

Figure 2.6 shows LSV results of KMC simulations modeling the primary passivation process in Fe-Cr alloys. Owing to the finite thickness of the cell size in the simulations, we found that the 11 at.% Cr alloy dissolved completely prior to passivation. Figure 2.2(a) and 3.5(a) show experimental LSV of Fe-Cr and Ni-Cr alloys in 0.1M H_2SO_4. The behavior of the Fe-Cr alloys containing up to 11.6 at.% Cr shows two waves and as the Cr concentration in this alloy increases the waves shift down in potential. Since our KMC results do not display this behavior, we suggest that it is connected to the electronic Cr-cluster size effects described above. In order to determine the charge density and h during primary passivation as a function of Cr concentration, potential step experiments were performed. A single potential for these experiments was chosen that included the peak in the passivation wave for each of the Fe-Cr and Ni-Cr compositions examined. In the case of the KMC simulations a potential step was performed from 0.1 - 0.7 V to determine the charge density and h associated with the primary passivation process. Figure 2.18, 2.17(a), 3.5 show the results. This analysis reveals the excellent fit to the theory, in that the values obtained are within 0.01 of the theoretical values of for BCC and FCC lattices[88].

Online ICP-MS was used to examine two assumptions of the model: undercutting of -Cr-O-Cr- mer-units, and selective dissolution[156,157]. Figure 2.14 and 3.7 show the ICP-MS results for key compositions of the Fe-Cr and Ni-Cr alloys. For the Fe-9.4 at.% Cr alloy there is a hint of selective dissolution in the active region, but otherwise the dissolution is virtually congruent to the alloy composition. For this alloy composition, the passivation process is similar to that of elemental iron and a good self-healing passive film is not formed. Both the Fe-14.4 at.% Cr and Fe-20.1 at.% Cr alloys exhibit selective Fe dissolution in the active region and just past the peak in the potential wave, we observe significant increases in the selective dissolution of Fe.

For the Ni-Cr alloys selective Ni dissolution initiates at potentials below the corrosion potential and continues throughout the LSV. Figure 2.15 and 3.8 show results for the mass density dissolution rates converted to current densities. For all the Fe-Cr and Ni-Cr alloys the ICP-MS evaluated current densities are larger than that observed in the corresponding LSV. This is despite the fact that the ICP-MS data do not include the oxidative process associated with the formation of the stable, non-dissolved, -Cr-O-Cr- mer-units and the oxidized iron or nickel incorporated in the primary passive film. We attribute these discrepancies between the electrochemical current densities and the ICP-MS data to undercutting of isolated mer-units.

We now address the cluster size effects previously described. As the Cr composition in the alloy increases from 5 to 20 at.%, the average surface Cr cluster size changes from isolated monomers to trimers (figure 2.11). DFT calculations were used to examine how the dissociative heat of adsorption of dioxygen varies with the size of surface Cr atom clusters. Figure 2.12 shows results for Fe, Cr and Fe-doped Cr (110) and

(100) surfaces. The adsorption energy for Cr(110) is -4.25 eV and that for Fe(110) is about 76% this value. There is almost a linear decrease in the adsorption heat as the Fe(110) surface is doped with a monomer Cr atom to a trimer Cr cluster. For Fe(110) doped with a trimer surface cluster, the adsorption energy is already about 91% that of pure Cr. The situation for the (100) surface is similar except that the adsorption energy on Fe is only about 25% that of Cr. For the Fe(100) surface doped with a Cr trimer cluster the adsorption energy is 78% that of Cr(100). We conclude that there is rapid convergence of the adsorption energies to that of pure Cr with increasing Cr cluster size.

Our results for Fe-Cr and Ni-Cr alloys assume that the alloys are ideal solid solutions. Importantly, almost all real alloys show some degree of non-ideality often described in terms the statistics of regular solutions and their tendency to short-range order or cluster[158]. In order to address how this would impact our theory, we performed large cell MC-RNG calculations[101] to determine the effect of short-range order and clustering on percolation thresholds in BCC Fe-Cr alloys. In this model, the tendency toward ordering or clustering is determined by the interaction parameter, $\Delta E = [E_{Fe-Cr} - 1/2(E_{Fe-Fe} + E_{Cr-Cr})]$, where the E's are pairwise bond energies. Over the composition range of interest, we examine ΔE values between -0.015 to +0.015 eV. Figure 2.23 summarizes our MC-RNG results that show that small tendencies toward ordering and clustering can have large effects on the 1st NN percolation threshold, $p_c^{3D}\{1\}$. For ΔE = +0.015 eV, $p_c^{3D}\{1\}$ changes from the random value of 0.246 to 0.162 and in the case of short-range order, for ΔE = -0.015, $p_c^{3D}\{1\}$ = 0.296. These results show that for passivation processes that depend on 1st NN connectivity, ordering and clustering can significantly affect the corrosion behavior of alloys. Figure 2.24 shows

KMC results for fits to our theory for Fe-Cr alloys in the case of short-range ordered and clustered alloys. We note that the differences are small because in the case of Fe-Cr alloys, passivation depends on which is barely affected by the small deviations from randomness considered above. However, for alloy systems showing stronger ordering or clustering, our results indicate that that these phenomena can be used as a “knob” to tune alloy passivation behavior.

As shown in figure 5.1, our theory provides a quantitative path forward for designing corrosion resistant alloys that minimizes the requisite metal dissolution for passive film formation in aqueous electrolytes. Within a range of composition, for simple binary alloys like Fe-Cr and Ni-Cr, the nearest neighbor spacing is inexorably tied to the composition. However, modern alloys, currently being developed for a variety of potential applications, such as those containing multi-principal elements are different, in that the NN spacing can be separately tuned by varying the composition and number of components that do not directly contribute to passivation behavior[142-144]. Additionally, in alloy systems for which passivation can be tuned to first nearest neighbors, ordering and clustering are predicted to have significant effects on composition requirements for corrosion protection.